The role of calcium on deposit chemistry and corrosion in fluidized bed combustion of biomass

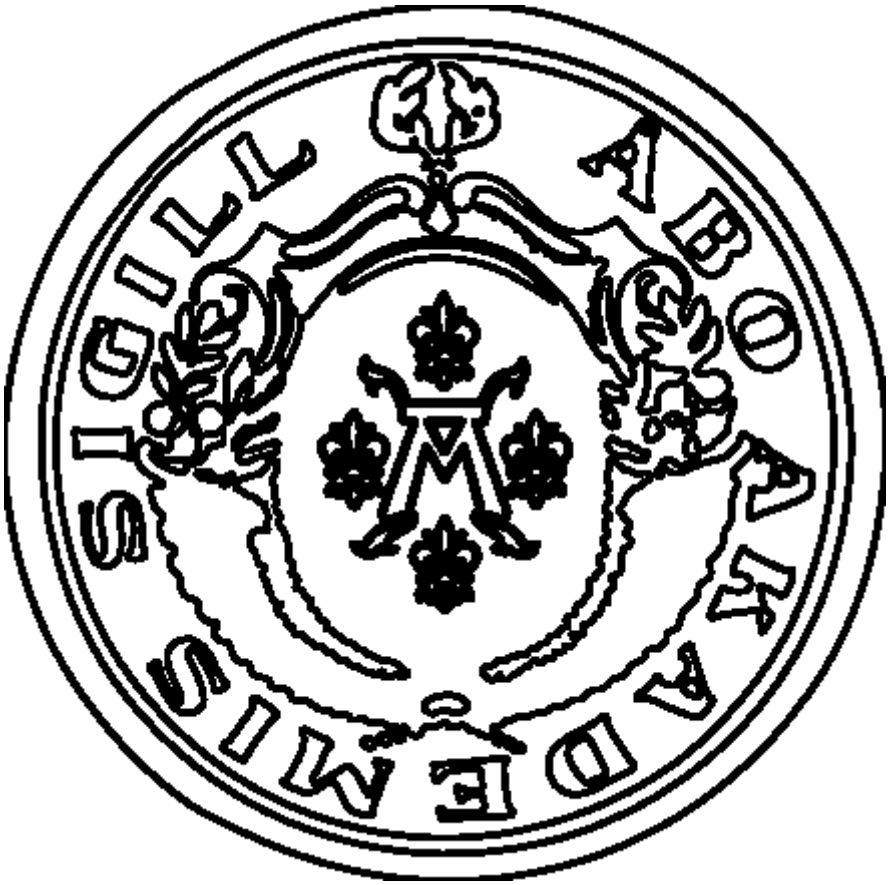

Jon Forstén, 37890
Laboratory of Molecular Science and Engineering
Supervisors: Emil Vainio D.Sc, and docent Patrik Yrjas
Faculty of Natural Science and Technology
Åbo Akademi University
2019

Abstract

Forstén Jon: The role of calcium on deposit chemistry and corrosion in fluidized bed combustion of biomass, Master's Thesis in Chemical Engineering, Faculty of Science and Engineering at Åbo Akademi University, Turku 2019

Increased interest in combustion of fuel mixtures containing calcium-rich sludges has created a need for a more detailed understanding of calcium behavior in fluidized bed boilers, as calcium may have an impact, both on high-temperature corrosion in the superheater region, and on low-temperature corrosion in the cold-end of the boiler. A higher calcium content in the fly ash may lead to a decreased sulfation of alkali chlorides and thus increase their accumulation in superheater deposits. In the colder end, the formation of hygroscopic calcium chloride has been shown to cause corrosion by forming wet deposits.

The objective of the research was to clarify the role of calcium on deposit chemistry and corrosion, from the superheater region to the cold-end in fluidized bed boilers. In order to achieve the objective, short-term deposit probe measurements were carried out in a full-scale BFB boiler, firing a calcium-rich fuel mixture, to study the behavior of calcium at various temperatures. Measurements were conducted before the secondary superheater, at the primary superheater, and the air preheater. The analysis methods SEM/EDX, TGA, and XRD, were utilized when analyzing the deposit samples obtained during the measurement campaign. The rate of deposit build-up and a corrosion rate index was also determined for the probe rings exposed in the superheater region. The data received from these methods were analyzed separately for all measurement locations.

The deposit collected in the superheater region can be described as somewhat aggressive, as a relatively high share of chlorine was detected, in comparison to the chlorine content in the fuel mixture. Visual signs of corrosion were observed on the X10CrMoVNb9-1 material at material temperatures between 525-550 °C at the measurement point just below the secondary superheater and 450 °C at the measurement point by the primary superheater. Iron chlorides were also detected in all of the samples collected in the superheater region. Based on spot analyses conducted on flakes detached from the ring surfaces, and XRD-analyses, the corrosion was alkali induced.

The significant amounts of alkali chlorides present in the deposit is a direct consequence of the incomplete sulfation of alkali chlorides in the freeboard. This is partly caused by the high amount of calcium, that captures the gaseous sulfur species. The high accumulation of alkali chlorides highlights the invalidity of the S/Cl fuel molar ratio in this case and shows that there is indeed an increased corrosion risk when firing fuel mixtures containing a high amount of calcium. In addition to sodium and potassium chlorides, there were indications of the presence of $CaCl_2$ at the primary superheter region. The amounts of chlorine in the cold-end deposit were low, however, still significant compared to the fuel content. Some corrosion was observed, and it was found to be caused by hygroscopic deposits at 80°C. At higher temperatures, up to 120°C (the highest temperature tested), corrosion was not observed. There were indications of $CaCl_2$ in the deposit, although the XRD-analysis could not confirm its presence. As other hygroscopic salts, such as NH_4Cl, could have possibly caused corrosion as well, the role of $CaCl_2$ on corrosion in this work remains unclear.

Svenska sammanfattning - Kalciumets roll i samband med beläggningsbildning och korrosion vid förbränning av biomassa i fluidiserade bäddar

Den 1 januari 2011 trädde en ny lag i kraft som omfattar beskattningen av avfall som förs till en avstjälpningsplats. För varje ton avfall som förs till avstjälpningsplatsen är skatten 70 euro. Sedan den nya avfallsskattelagen trädde i kraft har intresset för samförbränning av diverse biobränslen tillsammans med olika avfallsslam i fluidiserade bäddpannor ökat (1126/2010). En av orsakerna till detta är deras potential att fungera som bränsleadditiv. I Finland ligger det stor fokus på användningsmöjligheterna av slam som produceras inom skogsindustrin. Dessa slam tenderar att innehålla höga mängder kalcium och kunde fungera som ersättare till kalciumbaserade additiv. Användning av additiv ss. kalksten eller bränslen med höga kalciumhalter är typiska metoder för att binda svavel i rökgasen. Det har även visat sig att kalcium kan ha en inverkan på korrosion av överhettare såväl som korrosion på värmeväxlarkomponenter i den kallare ändan av rökgaskanalen. Eftersom kalcium uppfångar SO_2 och SO_3, kan en ökad mängd kalcium i bränslet leda till försämrad sulfatering av alkaliklorider och således öka risken för högtemperaturkorrosion (Anthony & Granatstein, 2000). Nyligen publicerad forskning har visat att hygroskopisk kalciumklorid orsakar korrosion genom att bilda fuktiga beläggningar i den kallare ändan av rökgaskanalen (Vainio et al., 2016). Målet med denna studie är att utöka förståelsen för kalciumets roll inom beläggningskemi och korrosion vid förbränningen av bränslen med höga kalciumhalter i bubblande fluidiserade bäddpannor (BFB).

Beläggnings- och korrosionsmätningar utfördes i en fullskalig BFB-panna där bränslesträmmar av bark, träflis och fiberslam förbränns under normal drift. Fiberslammet bildas vid reningen av avfallsvatten från kartongproduktion. Figur 1 visar ett tvärsnitt av pannan med mätpositionerna markerade. Sammansättningen, värmevärdet och några nyckeltal hos bränsleblandningen är även inkluderade i figuren. Den extremt höga andelen kalcium i bränslet tyder på att kalciumbaserade medel använts vid kartongbestrykningen. Det är även värt att notera att mängden klor i bränslet är rätt så låg.

Bränsledata	Enhet	Värde
Fukthalt	%	47,5
Aska	%, ts	8,4
Kalorimetriskt värde	MJ/kg	19,5
Ca	mg/kg ts	53 942
Mg	mg/kg ts	1287
Na	mg/kg ts	528
K	mg/kg ts	1918
P	mg/kg ts	538
S	mg/kg ts	660
Fe	mg/kg ts	958
Al	mg/kg ts	7258
Si	mg/kg ts	11 529
Cl	mg/kg ts	138
S/Cl molförhållandet		4,8
Ca/S molförhållandet		81,8

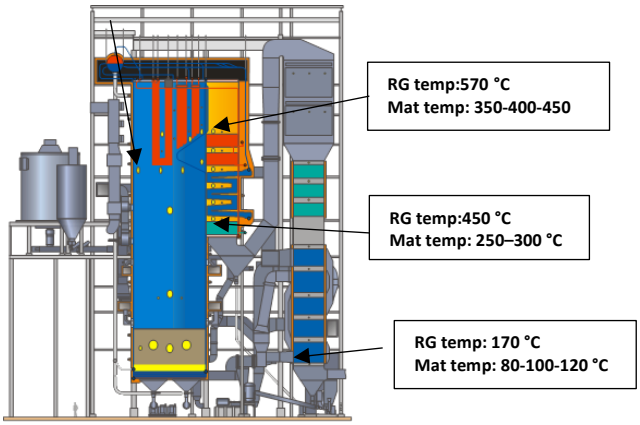

Figur 1. Ett tvärsnitt av BFB-pannan med mätpositionerna markerade. Rökgastemperaturerna under mätningarna och egenskaperna för bränsleblandningen är även inkluderade.

I beläggningsmätningarna användes luftkylda sonder tillverkade av Valmet och Åbo Akademi. En schematisk bild av en beläggningssond presenteras i Figur 2 a). Materialtemperaturen på sondringarna regleras med en inkommande luftström, vars flöde justeras med en ventil och PID-regulator. Hastigheten för ackumulationen av beläggningen (RBU, rate of deposit build-up) beräknades genom att jämföra ringarnas vikter före och efter exponeringen. RBU definieras som mängden beläggning uppsamlat per area och tid (g/m^2h). Bilder på beläggningarna togs med svepelektronmikroskop (SEM) och beläggningarnas elementära sammansättning bestämdes med röntgenelektronspektroskop (EDX). Med instrumentet utfördes area- och punktanalyser på tre olika markerade områden på ringarna; vind (W), sida (S) och lä (L). Vid analyserna beaktas läget på ringen och i vilken riktning placeringen är i förhållande till rökgasflödet. Analysområdenas positioner i förhållande till rökgasflödet framgår av Figur 2b.

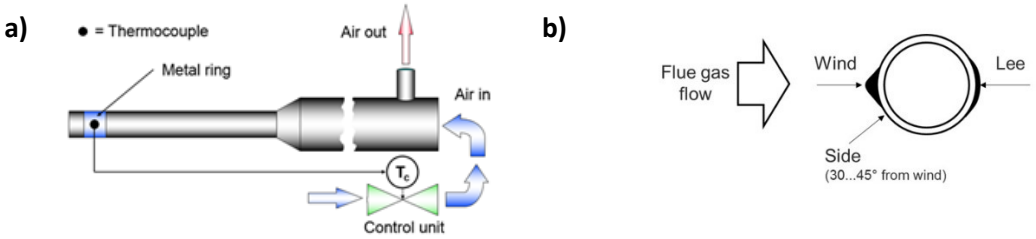

Figur 2. a) En schematisk bild av en beläggningssond. b) Visualisering av analysprincipen för beläggningarna. Sidobeläggnignen ligger 30 – 45° från vindsidan.

I Figur 3 visas de beräknade RBU-värdena och rökgastemperaturen för alla mätningar inom överhettarområdet. Vanligtvis betraktas RBU-värden som överskrider 20 g/m^{2}h som problematiska (Skrifvars, 2005). De uppmätta RBU-värdena är avsevärt lägre än denna gräns och kan därmed beskrivas som mycket låga. Under mätningarna drevs pannan på låg last, vilket resulterade i lägre rökgastemperaturer. Enligt Figur 3 har rökgastemperaturen varit under smältpunkten för ren kalium- och natriumklorid (Haynes, 2014). De låga rökgastemperaturerna har därmed sannolikt haft en inverkan på den låga ackumulationen av beläggning under mätningarna. Dessutom har Scala (2006, 2008) påvisat att en stor andel kalcium kan höja smältpunkten för askpartiklarna i rökgasen, vilket också kan ha varit en orsak till den låga beläggningsbildningen.

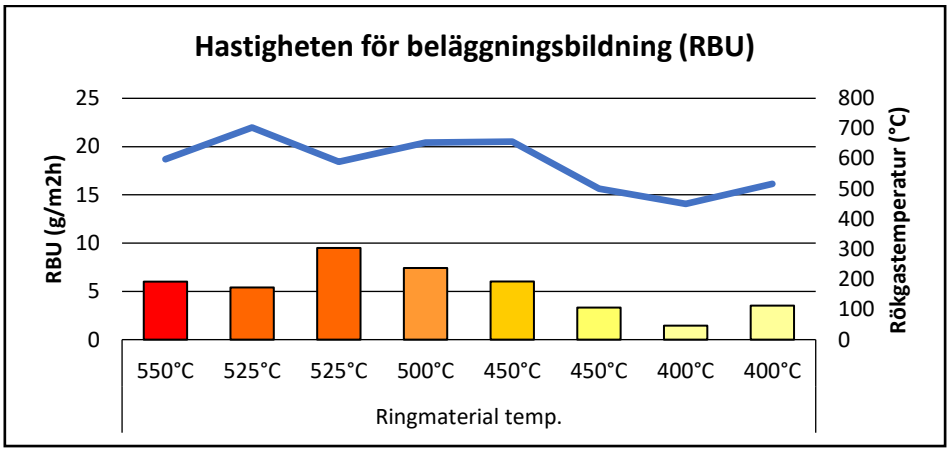

Figur 3. Beräknade RBU-värden för beläggningsproven som uppsamlats i överhettarområdet.

Areaanalyserna från beläggningsproven som uppsamlades före den sekundära överhettaren, vid den primära överhettaren och vid luftförvärmaren presenteras i Figur 4. I analyserna har främst förekomsten av natrium, kalium, klor, järn, svavel och kalcium beaktats och endast deras andelar i beläggningsproven presenteras i Figur 4.

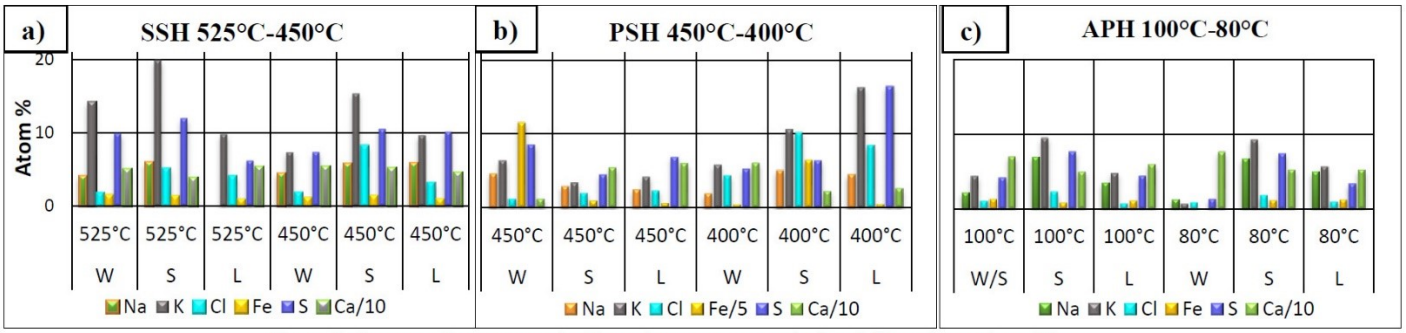

Figur 4. Areaanalyserna av beläggningar uppsamlade a) före den sekundära överhettaren b) vid den primära överhettaren och c) vid luftförvärmaren.

Enligt resultaten i Figur 4 domineras beläggningarna av olika kalciumföreningar. Kalcium förekommer ofta som oxid, karbonat eller sulfat i flygaska men det är svårt att fastställa vilka former som dominerar utgående från den elementära sammansättningen. I Figur 5a presenteras de elementära andelarna av kalcium och svavel samt molförhållandet mellan syre och kalcium för att klargöra i vilken kemisk form kalcium är. Eftersom andelen svavel i beläggningen var låg, var den teoretiskt maximala andelen kalciumsulfat i beläggningen även låg. Molförhållandet mellan syre och kalcium tyder på högre sannolikhet för en beläggning med högre andel av kalciumkarbonat.

I Figur 5b ges mängderna klor i beläggningar tagna vid primära och sekundära överhettarna och vid luftförvärmaren. Ackumulationen av klor i beläggningen var klart högre i överhettarområdet. Klorhalterna i beläggningarna tagna vid luftförvärmaren var mycket lägre, men i förhållande till klorandelen i bränslet är mängderna ändå ansenliga. Korrosion till följd av den höga ackumulationen av klor observerades på ytan av ringarna som bestod av materialet X10CrMoVNb9-1. Visuellt kunde korrosionen tydligast observeras vid materialtemperaturerna 525 °C och 550 °C för de ringar som exponerades vid den sekundära överhettaren och vid materialtemperaturen 450 °C för de ringar som exponerades vid den primära överhettaren. Beläggningarna kan allmänt karaktäriseras som något aggressiva, eftersom höga halter av klor detekterades i förhållande till den låga mängden klor i bränslet. Baserat på SEM/EDX areaanalyser och punktanalyser, kan det antas att kloret förekom som alkaliklorider. Förekomsten av klor tenderade att vara högre på sidan av ringen, oberoende av mätposition.

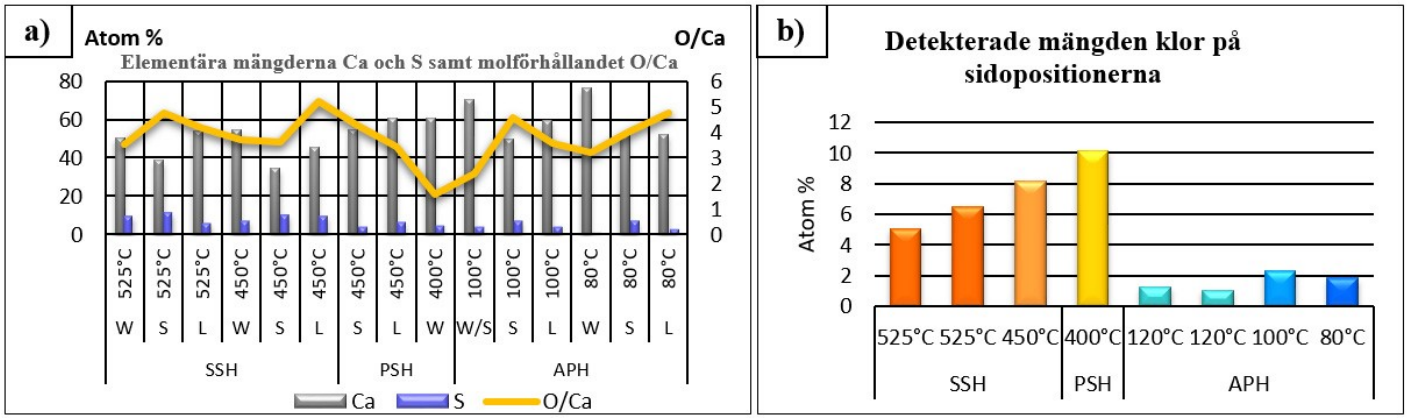

FIgur 5. a) Andelarna av kalcium och svavel i beläggningen i atomprocent. Molförhållandet mellan syre och kalcium är även inkluderat. b) Andelen klor detekterat på sidopositionen av sondringarna.

Ett av mätningarnas syften var att analysera förekomsten av det hygroskopiska saltet kalciumklorid. Utifrån molförhållandena i areaanalyserna kunde dess förekomst inte bestyrkas, men punktanalyser

utförda på prov från den primära överhettaren och luftförvärmaren gav indikationer på att små mängder kalciumklorid kan förekomma i beläggningarna. Punktanalyserna är markerade i SEM-bilderna i Figur 6 a) och b). Vid en del punkter (punkter 2, 4 och 7) förekommer det ett överskott av klor i förhållande till alkali- och järnhalterna. Således kan klor inte endast förekomma som järn- eller alkaliklorider. Förekomsten av kalciumklorid är därmed sannolik.

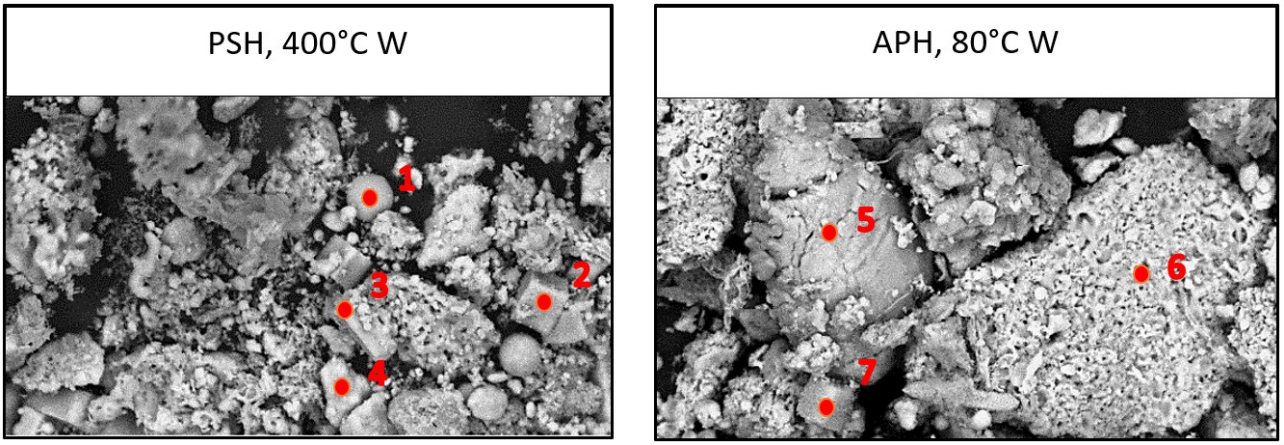

Prov	Analyspunkt	Na [at-%]	K	Cl	Ca	Fe	S	O	(Na+K)/Cl
PSH	1	7,3	5,5	1,0	6,4	0,2	0,1	57,3	12,4
	2	0,3	2,3	4,8	61,0		4,2	25,7	**0,5**
	3	0,7	0,6	1,3	38,8		0,7	56,2	1,0
	4		0,3	2,5	44,8	0,9	0,7	38,1	**0,1**
APH	5	0,3	0,1	0,2	32,8		0,2	64,8	1,8
	6	1,0	0,2	0,1	16,34		0,3	69,8	8,3
	7		0,4	1,1	24,0		1,4	72,5	**0,4**

Figur 6. SEM-EDX-resultat från beläggningsproven tagna vid den primära överhettaren (vänster) och luftförvärmaren (höger).

Sondförsök utfördes i en fullskalig bubblande fluidiserade bäddpanna med syftet att studera beteendemönstret av kalcium vid olika rökgas- och materialtemperaturer. Beläggningarna bestod till stor del av kalcium, vilket var väntat eftersom bränslet hade hög kalciumhalt. Trots att klorhalten i bränslet var låg detekterades relativt höga halter klor i beläggningarna som uppsamlats i överhettarområdet. Tydliga korrosionstecken detekterades på materialet X10CrMoVNb9-1 i överhettarområdet. Visuellt kunde korrosionen tydligast observeras vid materialtemperaturerna 525 °C och 550 °C för de ringar som exponerades vid den sekundära överhettaren och vid materialtemperaturen 450 °C för de ringar som exponerades vid den primära överhettaren. Enligt area- och punktanalyserna av beläggningarna förekom klor högst troligt som alkaliklorider. Den höga halten kalcium i bränslet har sannolikt lett till en minskad förekomst av svavel i rökgasen och därmed ökat ackumuleringen av alkaliklorider i beläggningarna. Punktanalyserna gav även indikationer på att små mängder $CaCl_2$ förekom i beläggningarna uppsamlade vid den primära

överhettaren och vid luftförvärmaren. I korrosionsmätningarna vid luftförvärmaren observerades korrosion på 16Mo3 vid 80 °C medan ingen korrosion noterades vid 100 °C och 120 °C.

Referenser

[1] A.L. Elled, K.O. Davidsson, L.E. Åmand. Sewage sludge as a deposit inhibitor when co-fired with high potassium fuels. Biomass Bioenergy, 34 (**2010**), Pages 1546-1554

[2] E.J. Anthony, D.L. Granatstein. Sulfation phenomena in fluidized bed combustion systems. *Progress in Energy and Combustion Science*, Volume 27 (2) (**2001**), Pages 215-236.

[3] E. Vainio, H. Kinnunen, T. Laurén, A. Brink, P. Yrjas, N. DeMartini. Low-temperature corrosion in co-combustion of biomass and solid recovered fuels. *Fuel*, 184 (**2016**), Pages 957-965.

[4] Bengt-Johan Skrifvars, Patrik Yrjas, Tor Laurén, Mikko Hupa and Martin Dittrich, The Åbo Akademi Database: Ash Behavior Measurements in Full-Scale Boilers, **18th** International Conference on Fluidized Bed Combustion Toronto, Ontario, Canada, May 22–25, **2005.**

[5] Stanislav V. Vassilev, David Baxter, Christina G. Vassileva, An overview of the behaviour of biomass during combustion: Part I. Phase-mineral transformations of organic and inorganic matter, *Fuel*, Volume 112 (**2013**), Pages 391-449

[6] F. Scala, R. Chirone, Characterization and early detection of bed agglomeration during the fluidized bed combustion of olive husk, *Energy & Fuels*, Volume 20 (**2006**), Pages 120–132.

[7] F. Scala, R. Chirone, An SEM/EDX study of bed agglomerates formed during fluidized bed combustion of three biomass fuels, *Biomass Bioenergy*, Volume 32 (**2008**), Pages 252–266.

Preface

This master's thesis was carried out as a collaboration between the Energy R&D department at Valmet Technologies Oy, and the Molecular Science and Engineering at Åbo Akademi University. The completion of this thesis signals the end to a one-and-half-year-stay at the R&D department in Tampere, and I would like to thank all my co-workers for the fun coffee breaks, lunches, and of course, working experiences.

I would like to extend my deepest gratitude to the supervisors of this thesis, Hanna Kinnunen from Valmet Technologies Oy, and Emil Vainio and Patrik Yrjas from Åbo Akademi University. Hanna has coordinated this research with honor and provided valuable support throughout this entire time, despite working a demanding full-time job and a doctoral thesis at the same time. Emil's level of expertise, especially in the untouched field of low-temperature corrosion, was crucial for the outcome of this thesis. Patrik, I wish to thank for reading and commenting on my thesis, and for helping me to improve the quality of my text.

I wish to thank the combustibility team members, Jaakko Tamminen and Davide Fantozzi, for engaging in discussions and providing insightful thoughts on various topics regarding the thesis. I am also grateful to Sonja Enestam, my boss, for providing me with the topic of my master thesis, and the opportunity to develop myself in this team of highly-skilled professionals.

Bomhus Energi AB is gratefully acknowledged for the possibility to carry out the measurements and for the good and helpful co-operation. I would also like to extend my sincere thanks to Linus Silvander and Markus Carlborg, for the SEM- and XRD-analyses conducted on the deposit samples, and to Borås University for providing fractionation references.

Finally, I would like to thank the friends I have made during my student years, my close group of friends back in Helsinki and my family for good moments and support during my years of studies.

1. Contents

1. Introduction

The utilization of waste streams as energy sources has emerged as a solution to two central challenges our society faces today, the replacement of fossil fuels with renewable energy sources and the minimization of landfill waste. In Finland, the attention towards sludges as a waste stream has increased due to the vast amounts generated. It has been estimated that an amount of 750,000 tons of dry sludge was produced in 2012 (Statistics Finland, 2014). The greatest share of sludges was generated by the pulp and paper sector, 67%. The options of sludge utilization are quite limited, and sludges have typically been either spread over land, used as landfill, or incinerated (Usherson, 1992). The results of research of sludges have, however, shown that they may have positive effects in combustion, including high sulfur and aluminosilicates contents leading to increased sulfation of alkali chlorides and capturing of alkali by aluminosilicates (Yrjas et al., 2009; Aho et al., 2010; Aho et al., 2008). The potential of sludges to function as an additive, the prospect of minimizing waste and the utilization of non-recyclable waste-streams as energy, has led to an increased interest in fluidized bed combustion of various biomass fuels together with different sludges. Political measures in the form of a taxations law have also provided incitements for the combustion of sludges. All landfills are now subject to a waste tax, set at 70 €/ton (1126/2010).

However, sludges may also affect combustion negatively. Sludges and especially the ones produced in the forest- and pulp and paper industry, tend to contain high amounts of calcium, which may have an impact on corrosion, both in the superheater region and the cold-end of the fluidized bed boiler. As calcium captures sulfur dioxide (SO_2) and sulfur trioxide (SO_3), a higher fuel content of calcium could lead to a decreased sulfation of alkali chlorides and thus increase the risk of high-temperature corrosion (Anthony and Granatstein, 2000). If HCl is present in the flue gas, hygroscopic calcium chloride may form which has been shown to cause corrosion in the cold-end by forming wet deposits (Vainio et al., 2016). The objective of this work is to understand the role of calcium on deposit chemistry and corrosion at various locations, from the superheater region to the cold-end of the boiler, in fluidized bed boilers utilizing calcium-rich fuels. In order to achieve the objectives of the research, a measurement campaign, consisting of short-term deposit probe measurements at various temperatures was conducted in a bubbling fluidized bed boiler (BFB), firing a fuel mixture, containing high amounts of calcium.

2. Fluidized bed boilers

Before the energy crisis in the late seventies, fluidized bed technology had primarily been used in different physical and chemical processes, such as coal gasification, catalytic cracking, or mixing processes (Oka, 2003). The information that had been gained during the research of these processes provided a good platform for developing the fluidized bed combustion technology. During the beginning of the energy crisis, the research intensified as great potential was seen in the technology. The main advantages of the technology were particularly: the ability to fire a wide range of fuels, the high combustion efficiency achieved at low combustion temperatures, and the high heat capacity of the bed were considered interesting. In Figure 1, the first generation of fluidized boiler is illustrated.

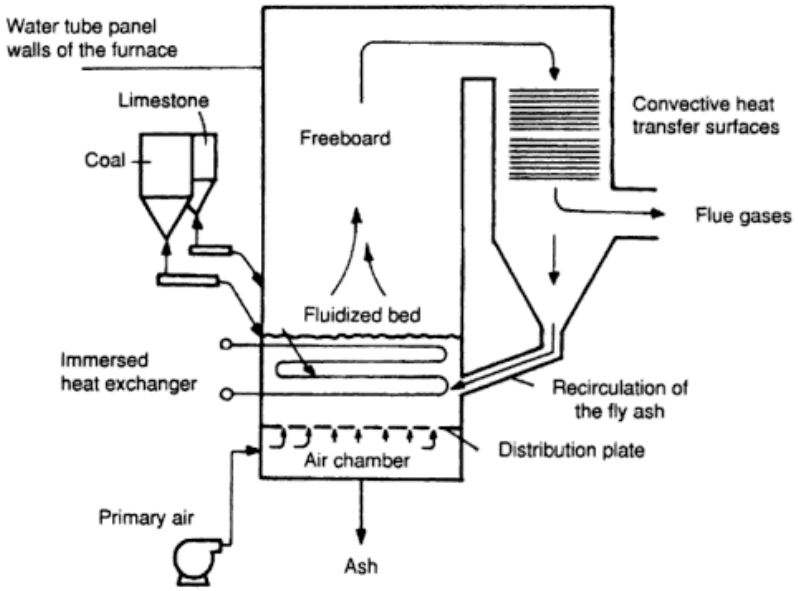

Figure 1: A schematic image of a first-generation fluidized bed boiler (Oka, 2003)

Fluidized bed boilers require a somewhat long start-up time, during which they are heated with either oil or gas burners (Van der Loo and Koppejan, 2002). The combustion temperature is usually required to be kept at relatively low temperatures, typically between 800-900 °C, to avoid ash sintering and defluidization in the bed. In addition, due to the low flue gas temperatures, no thermal nitrogen oxides are produced. The high investment costs required for the plants drive smaller investors towards fixed-bed technology, which is considerably cheaper. A negative aspect with fluidized bed combustion is the high loads of dust accumulated in the flue gas, making dust precipitators and cleaning technology necessary. Regular input of new bed material is also required

as a small fraction of the bed material is lost with the ash or changed on purpose to minimize agglomeration.

When speaking of fluidized bed boilers, two modes of fluidization are usually distinguished based on the velocity of the primary air flow (e.g Van der Loo and Koppejan, 2002). Boilers with a lower inlet air velocity are in the bubbling fluidization mode, while boilers with a higher fluidization velocity are in the circulating fluidization mode.

2.1 BFB

The BFB boilers, which were the first designs of fluidized bed combustors, became commercially available at the beginning of the 1980s (Van der Loo and Koppejan, 2002). It is operated in bubbling fluidization mode, meaning that the particles in the bed are actively moving, but the entire bed remains static. The fluidization velocity is usually kept in the range of 1.0 to 2.5 m/s when using a particle size of 1 mm. The fluidization velocity is controlled by the incoming flow of primary air. Horizontally placed inlets located above the bed introduces the secondary airflow and by further introducing tertiary air from the front and rear walls in the lower furnace, the combustion is completed at temperatures low enough to avoid the formation of thermal NO_x.

In bubbling fluidized bed boilers, an inert, granular bed material is used at the bottom of the furnace (e.g. Van der Loo and Koppejan, 2002). Fluidization occurs when primary combustion air is introduced from the bottom of the boiler, blowing through the layer of solid particles at such a high velocity that the particles separate from one another and attain behavioral properties to that of fluids. The fluidized mixture consists of 90-98 % of bed material, the rest being ash and fuel particles. The fluidization enables good heat transfer and mixing, leading to a low excess air demand as suitable conditions for complete combustion are provided. As the fuel represents merely a small fraction of the total bed mass, stable combustion of fuels with high moisture and low heating value is sustained. Due to the good mixing in the fluidized bed, a wide variety of fuels can be combusted. However, the combustion is limited by larger particles and impurities in the fuel, as too large particles will disrupt the fluidization. Thus, pretreatment of fuel, such as particle reduction and separation of metals is required before combustion. Due to the fluidization technology, erosion is a common challenge in fluidized beds.

In the superheaters (Figure 2), saturated steam is converted into dry steam (Oka, 2003). They are categorized into primary, secondary, and tertiary superheaters, not depending on their

chronological order but on the steam temperature level at their location. The steam temperature in the tertiary superheater is the highest. The temperature level of steam is managed by attemperators located between superheaters, in which steam and water are mixed. The energy in the steam flowing from the superheaters is then either converted into electricity or medium- or low-pressure steam. After the superheaters, the flue gas reaches the economizers. The purpose of the economizer is to utilize as much of the remaining heat content as possible of the flue gas, by pre-heating the feed-water. Simultaneously the flue gas is cooled.

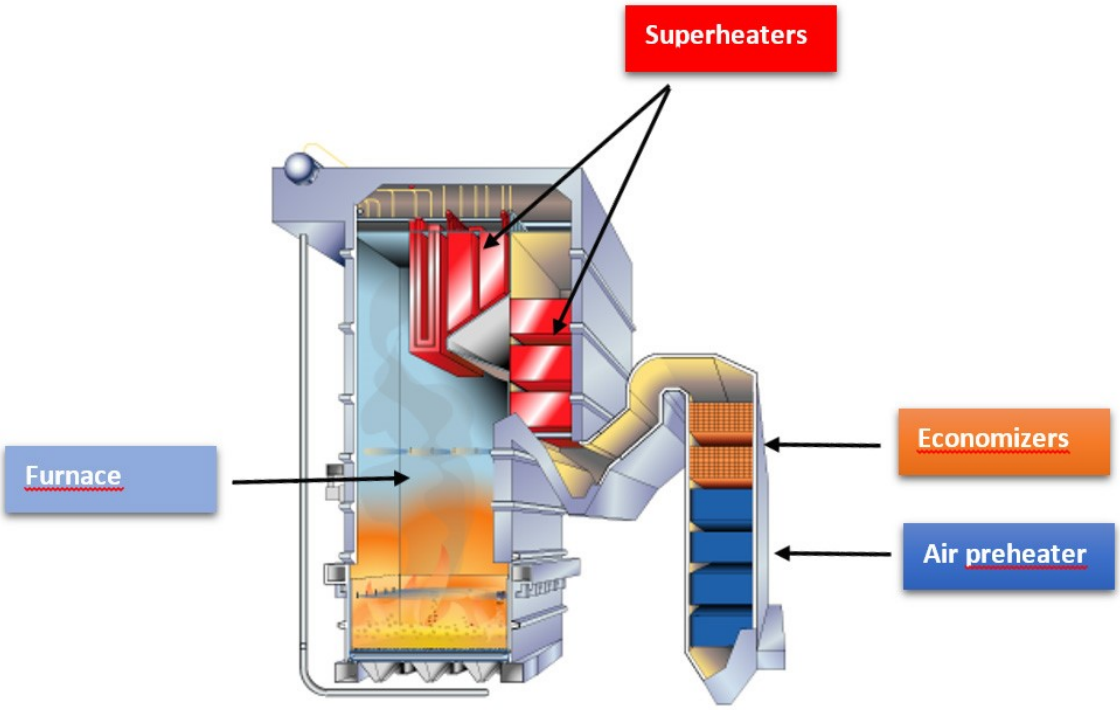

Figure 2: A cross-section of a bubbling fluidized bed boiler, courtesy of Valmet Technologies Oy.

Typical investors in BFB-technology are plants operating above a capacity of 20 MWth and up to 400 MWth (Courtesy of Valmet Technology Oy). The considered advantages with BFB is the possibility to operate the boiler using a wider range of particle size in the bed material, as well as firing fuels with varying moisture content (Oka, 2003). The combustion of fuel mixtures or co-firing different fuels is one of the more important characteristics of the fluidized bed technology. Although the BFB was a revelation when commercialized, dominating conventional coal firing and liquid and gas firing, there existed some flaws with the technology, which made room for improvement. The heat generation per unit area for BFB furnaces was considered limited when burning highly volatile fuels. Some of the flaws are more associated with designing furnaces of larger scale, such as difficulties with lateral fuel mixing. Larger scale boilers are more challenging to build, due to the required

number of fuel-feeding points needed to provide proper lateral mixing. The operation of BFB furnaces at partial load, which has long been a major disadvantage for BFB furnaces, has been solved by either splitting or staging the bed. Substantial reduction of erosion remains a challenge in second-generation units.

2.2 CFB

At the end of the seventies, the second-generation fluidized bed boilers emerged (Oka, 2003). The circulating fluidized bed technology was developed as, one wanted to increase the efficiency of the system by recirculating fly ash, allowing unconsumed fuel particles to re-enter the furnace. The boilers are operated in a faster fluidization mode, with solid particles moving towards the upper part of the furnace and into a cyclone (Figure 3), where they are separated and reintroduced to the bottom of the furnace. The fluidization velocity is typically adjusted to between 5 and 10 m/s, and the particles used are typically 0.2 mm to 0.4 mm in diameter size. A higher heat transfer and a more even temperature distribution are achieved by the more intensive fluidization, improving the prospects of stable combustion, the controlling of air staging and the distribution of heat surfaces in the upper part of the furnace (Van der Loo and Koppejan, 2002). Due to the higher erosion risks of CFB:s the lower parts of the furnace, is usually protected by, e.g. a weld overlay. When compared to BFB:s, the negative aspects with CFB furnaces are the larger investments required due to their greater size of the boilers, a greater amount of dust load, the higher amount of bed material entrained in the flue gas, leading to an increased loss of particles. In addition, some fuel pretreatment is usually required to obtain smaller sized fuel particles, which are needed for a higher fluidization velocity, causing increased investments. It is also challenging to operate a CFB at part load.

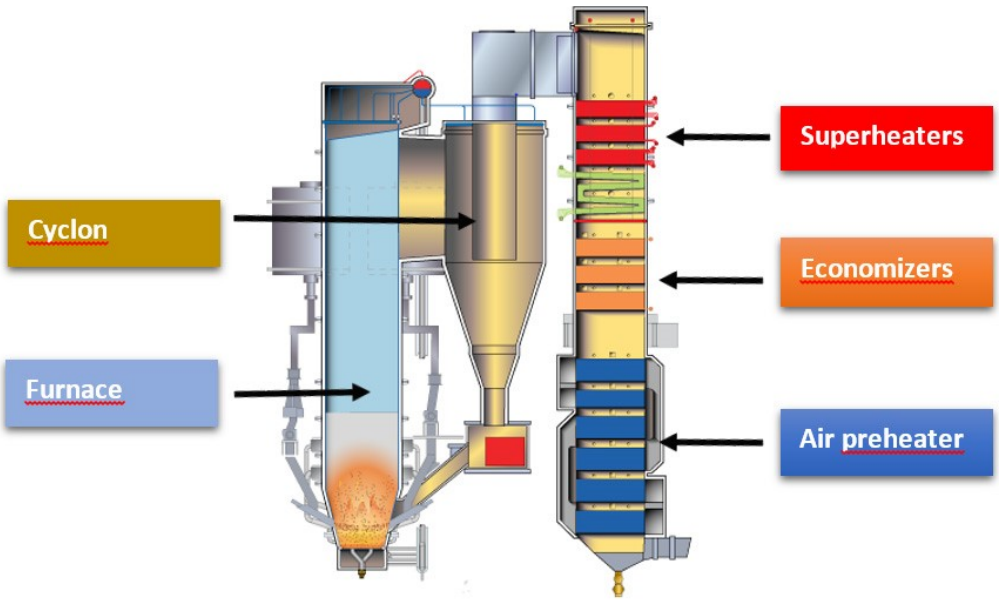

Figure 3: A cross-section of a circulating fluidized bed boiler, courtesy of Valmet Technologies Oy.

The technology of CFB:s regarding the combustion of heterogenous fuels has paved the way for using solid biobased fuels, however, some challenges remain (Van der Loo and Koppejan, 2002). In order to comply with the energy price, rising energy demand, and availability of biomass when shifting from fossil fuels, a wide variety of renewable fuels must be utilized for energy. However, there is a clear correlation between fuel price and the challenge of combustion. Lower-priced fuels tend to be more challenging to fire, which is the case for e.g.: fast-growing wood, agricultural residues, and waste streams. In the introduction, the increased interest in sludges as fuel was mentioned and that the co-combustion of sludges, together with other biomass fuels, is still a relatively unexplored area and requires further research. Therefore, analyses of sludges and the fuels they are typically co-combusted with will be presented and discussed in the following section.

3. Fuel analysis methods and backgrounds

The ash formed during combustion is a source of severe problems in boilers, such as slagging, bed agglomeration, fouling, and corrosion. The behavior of the ash can be better understood through detailed fuel analysis, to obtain information such as the amount of ash produced and in which chemical form the major ash-forming elements are present as (Baxter, 1993). In this section, fuels essential for co-combustion of sludges will be discussed. The focus lies on the chemical composition of the fuels and fractionation results, which provide further information about the reactivity of the major elements. As the origin of the sludges greatly influences the fuel properties, the background

of all fuels will be discussed. An attempt to clarify the differences between sludges and their fuel properties will also be made, as the definition of different sludge streams is somewhat vague.

Most of the sludges brought up in this work, originate from different processes in the wood- and paper industry. They are typically combusted close to their production facility, together with other forest residues. Therefore, wood and bark of common species in the Nordic countries and eucalyptus, which is growing more and more popular, are included in this section to represent examples of wood-based fuels.

3.1 Standard fuel analysis

Standard fuel characterization of new fuels typically consists of proximate, ultimate, and elemental analyses. The determination of the fuels' calorific value is also normally included. Proximate analysis yields information about the amounts of moisture, volatile matter, ash, and fixed carbon content in the fuel, while ultimate analysis refers to the content of carbon, hydrogen, nitrogen, sulfur, chlorine and oxygen, including also moisture and ash. In addition, often the determination of the major (Al, Ca, Fe, Mg, P, K, Si, Na, Mn and Ti) and minor (As, Ba, Cd, Co, Cr, Cu, Hg, Mn, Mo, Ni, Pb, Sb, V, Zn) ash-forming elements present is of high interest.

3.2 Chemical fractionation

Chemical fractionation is one of the established main methods of fuel characterization at Åbo Akademi University (Zevenhoven et al., 2012). In this method, the leachabilities of the fuel elements are determined by stepwise leaching of the fuel sample. The increasingly aggressive solvents used in chemical fractionation are usually: water, an ion exchangeable solvent, and acid. Based on each element´s solubility in each of the solvents used, the ash-forming matter can then be categorized. In Figure 4, a simplified scheme of the process is presented.

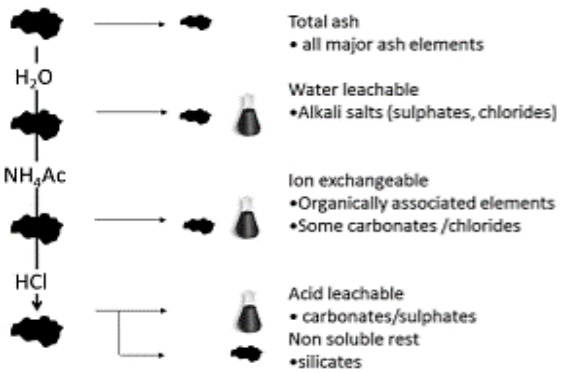

Figure 4: A simplified process scheme of the fractionation method (Zevenhoven et al., 2012).

Ash forming matter is generally categorized into four groups, depending on its chemical form. These categories are organically bound matter, dissolved salts, excluded minerals, and included minerals (Reid, 1984). Metal cations of K, Na, Mn, Ca, Mg, Fe, and Al can be bound to anionic organic groups in biomass. These metals are often capable of undergoing ion-exchange with ammonium acetate. Elements recurrently detected in the organic phase are sulfur, which is present as bridges between organic molecules in several amino acids (Baxter, 1994). Calcium has a similar role in the cell wall of plants. Phosphorus is also known to be present in various organic forms (Brinch-Pedersen et al., 2002; Marschner, 2011; Skrifvars et al., 1998).

The moisture or fluids in biomass typically contain cations, such as K^+, Na^+ and Ca^{2+}, and anions such as Cl^-, HPO_4^{2-}, $H_2PO_4^{2-}$, SO_4^{2-} and $Si(OH)_3O^-$ (Zevenhoven et al., 2012). The elements in the fluids may also be present in a solid form if the biomass is dried but will remain soluble in water. Biomass or organic residues typically have a higher moisture content, compared to fossil fuels and inorganic waste.

Inorganic structures formed by natural precipitation in biomass is referred to as included minerals. Common examples of these are silica, calcium oxalate, and $Fe_2(SO_4)_3$ and $FePO_4$. These minerals typically demonstrate poor solubility during fractionation. Precipitated silica is insoluble even in acid and thereby is found in the rest fraction (Franceschi and Nakata, 2005). Included minerals of calcium are mostly soluble in acids. However, the solubility of calcium oxalate may vary as it can be present in various crystal structures (Pontoppidan et al., 2007). Excluded inorganic calcium exists as calcium silicates and calcium aluminosilicates in sand and clay material, usually present as contaminations in the fuel. These compounds typically remain insoluble.

3.3 Wood

Forests cover more than 70 % of the total land area of Finland (Ministry of Agriculture and Forestry, 2019). As forests are the main natural resource in Finland, the forest industry has through the years become a vital part of the national economy. In 2018 a total of 78 million m^3 of wood was harvested in Finland. Of this only 11 % was utilized directly as energy in the heating of houses and farms. Most of the wood-based fuels combusted in power plants are residues from the forest industry, such as wood chips, sawdust, and bark. Sawdust can also be used in the production of pellets and briquettes.

Wood-based fuels can be combusted without any challenges (Stromberg and Herstad Svard, 2012). The nature of the ash is not aggressive, and the ash does not typically cause corrosion. The fuel

generates a low amount of ash, which has a high melting temperature and therefore leads to low amounts of deposit build-up on heat exchanger components. Fractionation results from the wood of spruce, pine, and birch are presented in Figure 5. These species of wood were chosen as they are the most common in the Nordic countries. The fractionation data of the pine was obtained from the Fractionation Database of Valmet Technologies Oy. The data of the spruce (Sample ID: 90) and birch (Sample ID: 221) were obtained from the Fractionation Database of Åbo Akademi University.

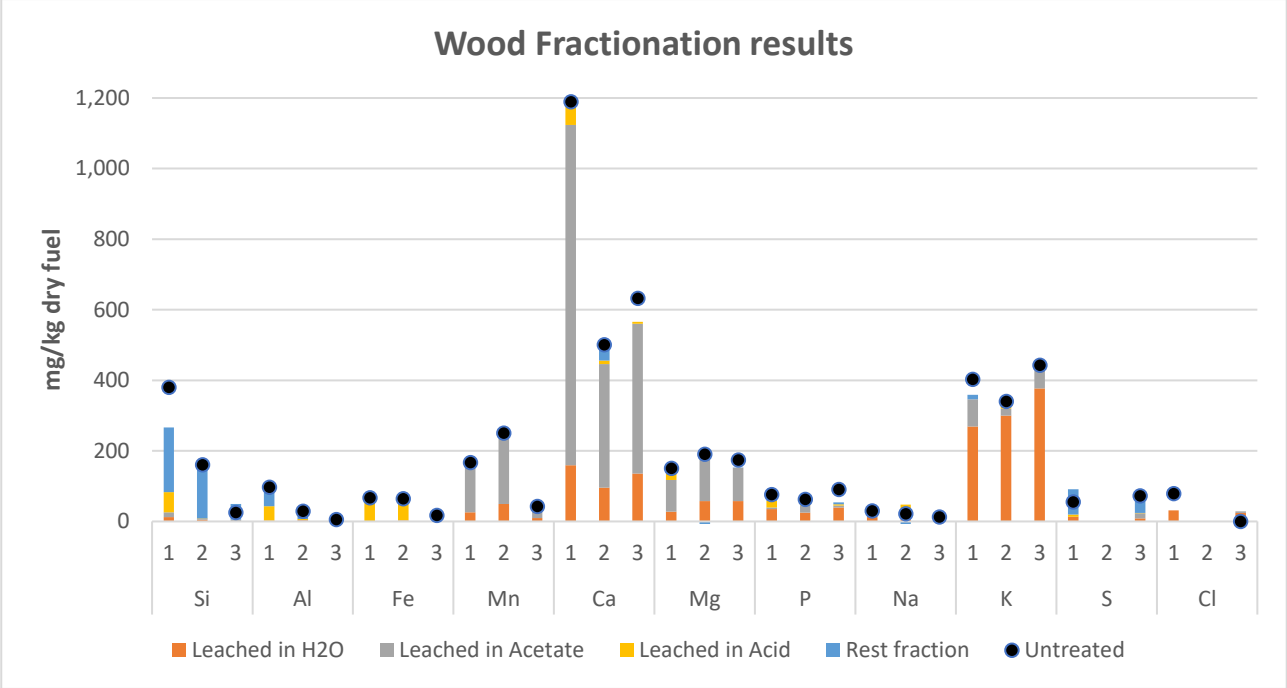

Figure 5: Fractionation results from the stem wood of the species spruce (nr. 1), pine (nr. 2) and birch (nr. 3).

Overall, the concentrations of main ash-forming elements detected were quite low. The elements present in the highest concentrations were calcium, potassium, and silicon. Calcium was found to be soluble mainly in the organic and water phase. A small portion of calcium in the spruce was also found in the acidic phase. Potassium was mainly present in an easily soluble form, although the concentrations are so low that it cannot be considered a challenge for combustion. Silicon was primarily insoluble. The concentration of chlorine was low in all samples.

3.4 Bark

A significant amount of the total tree weight consists of bark, around 10%, meaning that bark is a rather large residue stream for forest industries (Senelwa and Sims, 1999). As a fuel, the characteristics of bark differ somewhat from that of wood. There are typically more ash forming compounds in bark compared to wood, which naturally results in a higher ash content for bark. Especially, calcium belongs to this group of elements (Werkelin et al., 2010). Surplus of calcium in

the tree is usually transported to the outer parts of the wood and precipitated as calcium oxalate in the inner part of the bark. Challenges with the leachability of calcium oxalate have however been reported (Werkelin, 2010). It is suspected that the non-leached fraction of Ca consisted of calcium oxalate, which did not dissolve in acid. However, the non-leached Ca-fraction corresponded to less than 10% of the acid leached fraction. In Figure 6, fractionation results of bark from spruce, pine, birch, and eucalyptus are presented. The eucalyptus species was also added as the production of eucalyptus pulp has increased. Eucalyptus bark also contains high amounts of calcium. The fractionation data of the pine and eucalyptus bark was obtained from the Fractionation Database of Valmet Technologies Oy. The data of the spruce (Sample ID: 67) and birch bark (Sample ID: 79) were obtained from the Fractionation Database of Åbo Akademi University.

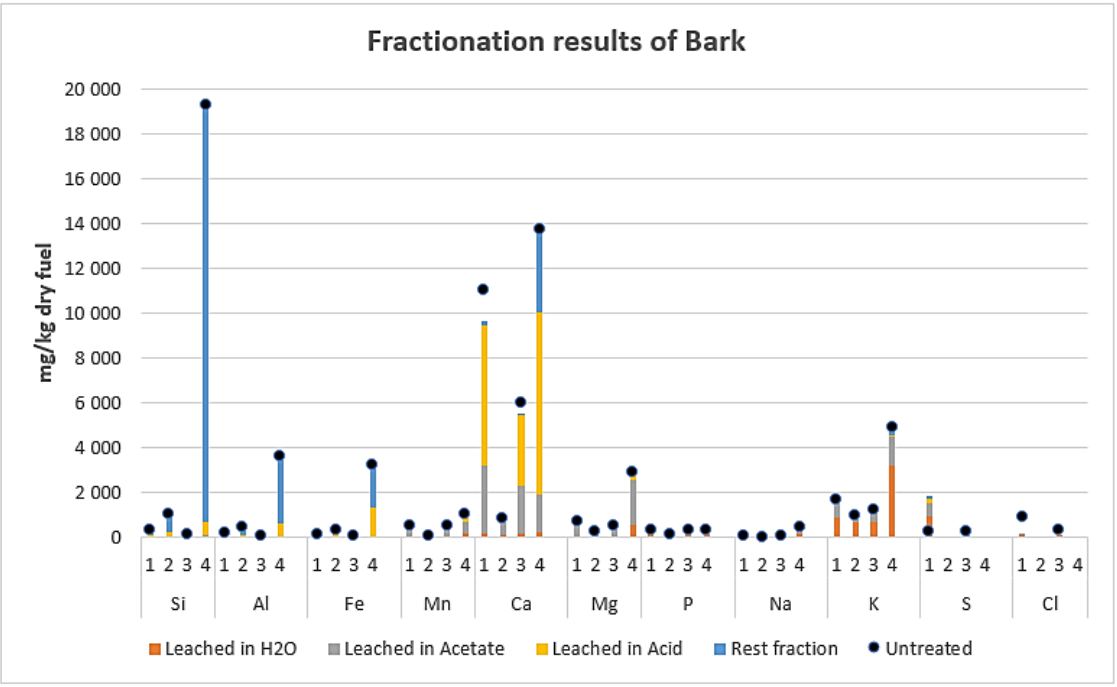

Figure 6: Fractionation results from the bark of spruce (nr. 1), pine (nr. 2), birch (nr. 3) and eucalyptus (nr. 4).

The fractionation results in Figure 6 show that the ash content of bark is higher, compared to stem wood (Figure 5). The bark ash consisted mainly of calcium and potassium. For the eucalyptus bark, one can recognize the same pattern, which became apparent in the research made by Werkelin et al. (2012). It appears that the major part of calcium is dissolved in acid, much likely as calcium oxalate (Handbook of combustion, Vol 4). However, the amount of Ca in the rest fraction is much more significant. It is unclear if differences of calcium solubility have an impact on the behavior of calcium particles during combustion.

3.5 Sludge

The solid remains of wastewater streams from industrial and municipal sources are called sludges (Tchobanoglous & Burton, 1991). Their disposal is problematic due to several reasons. If released into water, the oxygen available to the aquatic environment would be reduced as it is consumed during the breakdown of the organic material in sludge. The high content of pathogens and toxic elements poses a danger to human beings, flora, and fauna as well. Sewage sludge is typically more harmful, but high levels of legionella have also been detected in samples taken during the biological treatment of wastewater from pulp and paper mills (Allestam et al., 2006). Additionally, the high nutrient content of sludges could lead to the overpowering growth of aquatic plants. Because of their harmful nature, the processing of sludges is conducted to improve both chemical and physical characteristics, making future handling and disposal more comfortable and environmentally friendly.

The water treatment of sludges is a process conducted in several stages. During these stages, sludges with different characteristics are formed and separated into different waste streams. The process can vary from plant to plant, but the treatment is typically conducted in three stages. In Figure 7, a simplified overview of the treatment process of wastewater is presented.

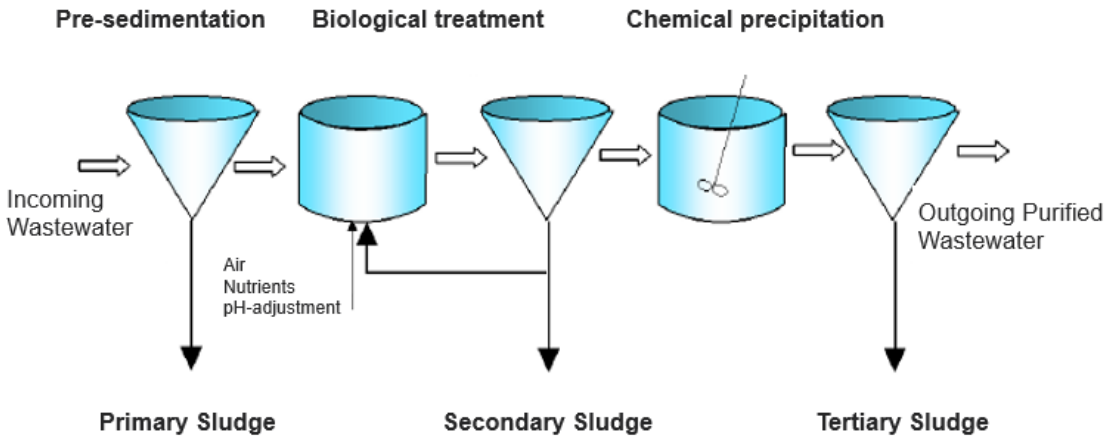

Figure 7: A simplified process scheme of the wastewater treatment process (Stromberg and Herstad Svard, 2012).

In the first stage, primary sludge is produced when solids and floating materials are separated from the wastewater in sedimentation tanks (Tchobanoglous et al., 1991). The wastewater which has undergone primary treatment still contains nutrients, organic matter, and colloidal particles that need to be removed during a secondary treatment process. The most common type of process is the activated sludge process, where added micro-organisms accomplish the decomposition of

organic content and removal of nutrients. The micro-organisms consume the nutrients in the wastewater during the decomposition of organic content and colloidal particles. The decomposition can be of aerobic, anaerobic nature, or a hybrid of those two. A sludge is then formed when the micro-organisms increase in size and number. The sludge created during this stage consists of biomass, which is formed when micro-organisms break down organic matter. In some treatment systems, the wastewater is chemically processed in a third stage to improve the characteristics of the wastewater further. The objective of this type of water treatment is typically to reduce toxicity, suspended solids, and organic matter, as well as to clarify the liquid. Ternary sludge is produced during the treatment when particulate matter is removed from the wastewater by utilizing chemical coagulation and precipitation.

The sludge-streams formed during the wastewater treatment is much diluted and requires further treatment to improve handling and combustibility. However, the poor dewatering properties of sludges makes it challenging to lower their water content (McGhee and Steel, 1991). By utilizing conventional dewatering methods such as thickening and mechanical dewatering, the moisture content can be lowered to approximately 75 % (Manzel, 1989). Additives are required to decrease the moisture content further. Stabilization and conditioning of sludges, which are used to remove pathogens and decrease toxicity, are other popular methods for sludge treatment, but they are more often utilized for sewage sludges.

3.5.1 Sludge from pulp and paper mills

The sludge-streams formed during the different stages of wastewater treatment in the pulp- and paper industry are fiber sludge, bio-sludge, and chemical sludge (Stromberg and Herstad Svard, 2012). These sludges may either be combusted as a sludge mixture or as separate streams. An amount of 560 000 tons of dry sludge per year is estimated to be produced in the Swedish forest industry. The size of the different fractions can be observed in Table 1.

Table 1: The yearly production of sludge streams in Sweden (Stromberg and Herstad Svard, 2012).

Stream	Tons of dry substance/year
Fiber sludge	186 000
Chemical sludge	42 000
Bio-sludge	72 000
De-inking sludge	185 000
Others	74 000
Total	**560 000**

The sludge-streams are challenging to compare, as the chemical and physical properties of the sludges are dependent on the type of industrial process the wastewater originates from and the raw material used, the stage of wastewater treatment they are produced in and the treatment the sludge receives after production. The use of recycled fiber as a raw material in the process generally leads to a higher volume of waste (Scott and Smith, 1995). The characteristics of the sludges will be discussed separately. Other sludge streams are also known, but there is limited data available on them.

3.5.1.1 Fiber sludge

The sludge recovered from the primary treatment of wastewater from pulp and paper mills is typically rich in fiber and is therefore referred to as fiber sludge. Due to its fibrous nature, it is generally easier to handle in comparison to other sludge streams, although this may vary. As the primary treatment is conducted without the addition of chemicals, the ash content of pure fiber sludge is generally low. However, the ash content can increase if the wastewater contains chemicals from the process stage during which wastewater is generated. Examples of these are coating agents and filler material used in paper production. Fiber sludge is generally easier to dewater and is therefore included in sludge mixtures with chemical and bio-sludge to improve their dewatering characteristics. Figure 8 presents an estimation of the amounts of the main ash forming elements in fiber sludges. The data was obtained from “The fuel handbook 2012” (Stromberg and Herstad Svard, 2012) and represent the mean values from several fiber sludges in Sweden.

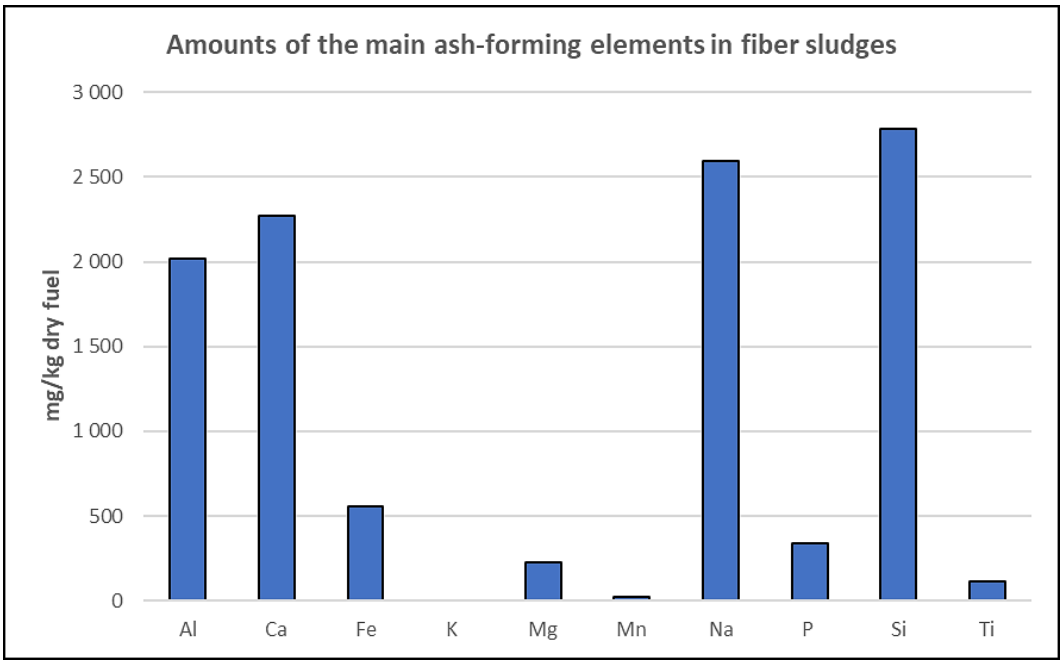

Figure 8: The average amounts of main ash forming elements in fiber sludges, based on data from "The fuel handbook 2012".

Figure 8 shows that the average fiber sludge contains low concentrations of ash-forming elements. Aluminum, calcium, sodium, and silicon are the dominating elements, but none of them reaches higher than 3000 mg/kg.

3.5.1.2 Biological sludge

The sludge recovered from the secondary treatment process is referred to as biological sludge. Compared to other sludge streams in general, bio-sludge has proven to be the most challenging to handle. Exposure to bio-sludge can be harmful, as high amounts of legionella pathogens have been detected in bio-sludge. The bacteria can be contagious if present as aerosols. The moisture content of bio-sludge is typically higher compared to fiber and chemical sludge, which makes it challenging to transport. Bio-sludge is difficult to dewater as it contains high amounts of bound water, and only free water can be removed during mechanical dewatering. A method where heat from steam causes the destruction of cell membranes has been used to decrease the moisture content of bio-sludge. Due to the poor dewatering characteristics, bio-sludge is often included in mixtures with fiber sludge. Figure 9 presents an estimation of the amounts of the main ash forming elements in biological sludges. The data was obtained from "The fuel handbook 2012" (Stromberg and Herstad Svard, 2012) and represent the mean values from several bio-sludges in Sweden.

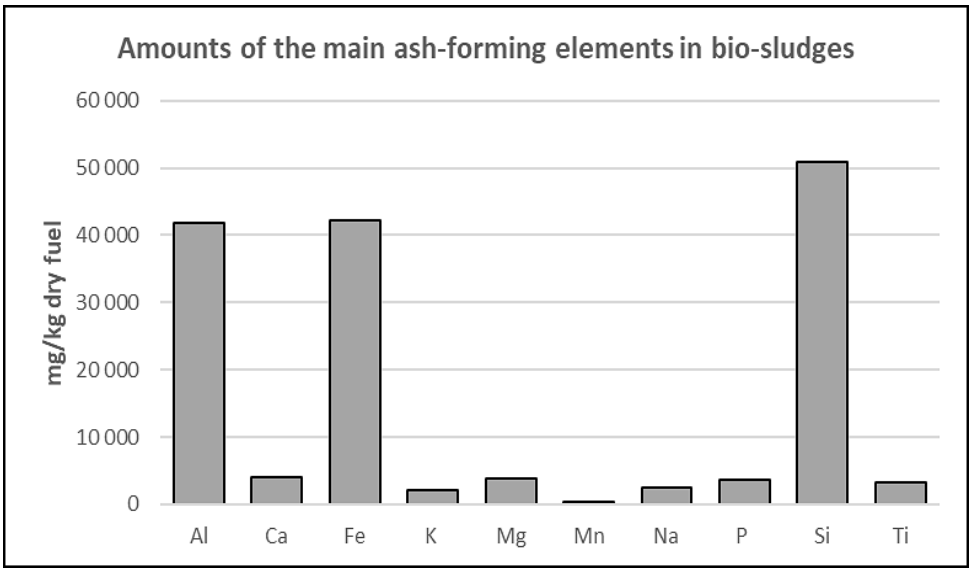

Figure 9: The average amounts of main ash forming elements in bio-sludges, based on data from "The fuel handbook 2012".

The figure shows that the ash forming elements in bio-sludges are dominated by aluminum, iron, and silicon. Aluminum silicate is a highly efficient coagulant, often utilized by industrial and municipal plants in wastewater treatment. Aluminum silicate is also a common filler material in the production of board to improve optical properties, printability, and other physical properties of the products. Iron is also known to be used in wastewater treatment as a coagulant, adsorbent, and redox catalyst. The presence of aluminum, iron, and silicon in high amounts is not typical to bio-sludge as chemicals are commonly not used during the secondary treatment. It is, however, not surprising, as elements can remain from the process, where the wastewater is generated. Elements may also originate from sludge processing, where additives might be needed to decrease the moisture to an acceptable level. Sometimes chemical treatment is conducted in combination with biological treatment. The ash content for pure bio-sludge is usually low but increases if chemicals have been used. When firing bio-sludge, its high nitrogen content needs to be considered, as the risk of NO_x formation increases.

3.5.1.3 Chemical sludge

Chemical treatment of wastewater can be conducted during different stages in the treatment process, sometimes even in combination with biological treatment. Therefore, it is challenging to characterize chemical sludges based on their fuel properties as their elemental compositions are typically inconsistent. The most influential parameter of a chemical sludge is the selection of chemicals (coagulants) used during the treatment process. The chemicals remain with the sludge after the treatment and are typically seen in significant concentrations in the sludge. Not only does

the added chemicals remain with the sludge, but the choice of coagulant could have an impact on the sulfur and chlorine concentrations as well. On average, the moisture content of chemical sludge is lower compared to biological sludge, although it can still be high if it contains organic matter. Fiber sludge is usually incorporated into chemical sludge to improve its poor dewatering capabilities. Figure 10 presents an estimation of the amounts of the main ash forming elements in chemical sludges. The data was obtained from "The fuel handbook 2012" (Stromberg and Herstad Svard, 2012) and represent the mean values from several chemical sludges in Sweden.

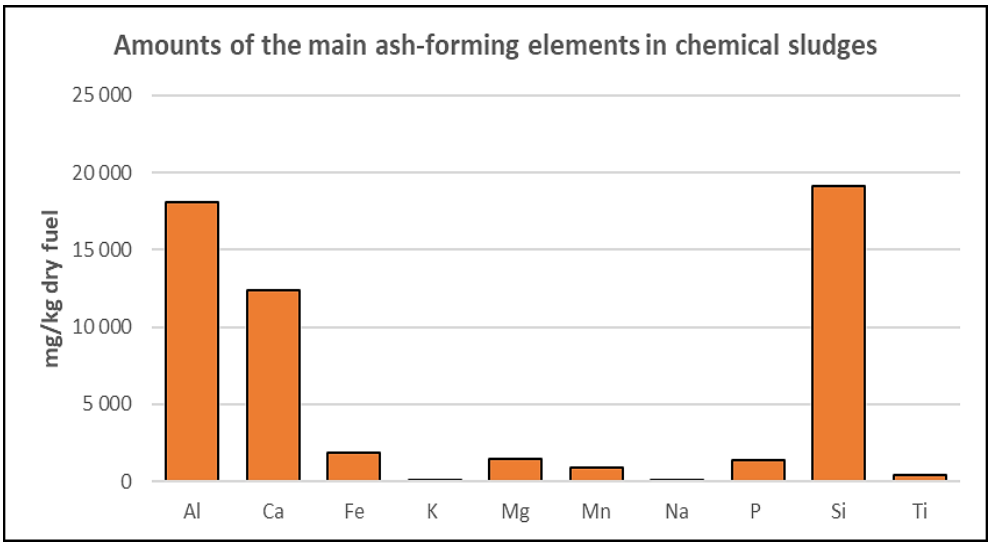

Figure 10: The average amounts of main ash forming elements in bio-sludges, based on data from "The fuel handbook 2012".

Although they are not found in as high concentrations as in bio-sludge, both aluminum and silicon are present in a typical chemical sludge. As mentioned earlier, aluminum silicate is a common coagulant and filler material, and its presence in chemical sludge is accordingly expected. Calcium, which is also used as a coagulant during water treatment and as a paper filler, is also present in relatively high concentrations.

Due to the shifting nature of chemical sludges, the experiences when firing chemical sludges are different and challenging to compare. However, the general perception of a chemical sludge is that it does not tend to contribute to bed agglomeration. Involvement in corrosion depends on the amounts of sulfur, chlorine, and calcium.

3.5.1.4 De-inking sludge

Removal of ink, along with other components, such as paper coatings, is required if wastepaper is to be recycled. The sludge formed from this process is known as de-inking sludge (Stromberg and Herstad Svard, 2012). A substantial amount of sludge is produced during de-inking when the paper

contains higher fractions of non-cellulosic compounds. De-inking sludges are easy to dewater and, therefore generally trouble-free to handle before combustion. However, the high amounts of ash formed when firing de-inking sludges results in increased demands of ash handling. The amount of ash produced is dependent on the paper source. In Figure 11, fuel fractionation data from three de-inking sludges are presented. The fractionation data of these fuels were obtained from the Fractionation Database of Valmet Technologies Oy. In these fuels, chlorine had either not been analyzed, or was not detected.

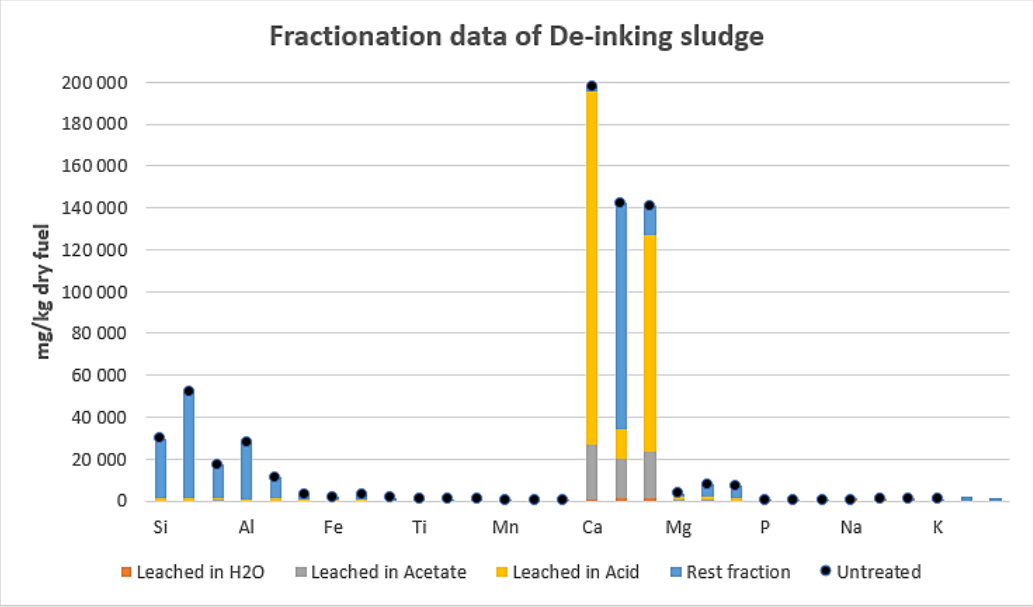

Figure 11: Fractionation results from three de-inking sludges.

The extremely high content of calcium is likely due to calcium-based filler material leached from the paper source. While the left-hand side sludge contains a high fraction of calcium soluble in acid, the concentration of the rest fraction is low. For the second sludge, the situation is different since it has a high fraction of insoluble calcium and a low fraction dissolved in acid. The differences are likely related to the choice of filler material in the paper. The calcium-based compounds present could be calcium carbonate and clay calcium bentonite, which are both used during paper manufacturing as filler materials (Murray, 2002). While calcium carbonate is known to dissolve in acid, clay calcium bentonite is not. The choice of filler material could, therefore, define the chemical characteristics of the sludge.

De-inking sludge can be fired in significantly higher fractions, compared to other sludges. Experiences from firing de-inking sludge have shown it tends to decrease sintering and, in some cases, corrosion as well (Stromberg and Herstad Svard, 2012). However, based on the amount of

calcium present in the de-inking sludges investigated (Figure 11), the combustion of some de-inking sludges could lead to corrosion. The extreme amounts of calcium present in de-inking sludges may result in close to a complete desulfurization and, therefore, a decreased sulfation effect of potassium- and sodium chloride. However, the choice of a paper filler that contains insoluble calcium may impact on this type of behavior.

3.5.2 Sewage sludge

Sewage sludge is a by-product produced from wastewater treatment of municipal and industrial waste, which has been transported to the treatment plant via sewers. A yearly mass of eight million tons of sewage sludge has been estimated to be produced inside the EU (Wzorek, 2012). The same treatment process is utilized as in the treatment of wastewater from pulp and paper mills, a combination of mechanical, biological, and chemical treatment. However, the emphasize is stronger on the chemical treatment as sewage wastewater is usually more contaminated. In Figure 12, fractionation data of three sewage sludges is presented. The data of sewage sludges nr 1 & 2 was received from Borås University, Sweden. These sludges were produced in municipal treatment plants in Sweden. Data of the third sewage sludge (Sample ID: 209) was obtained from the Fractionation Database of Åbo Akademi University.

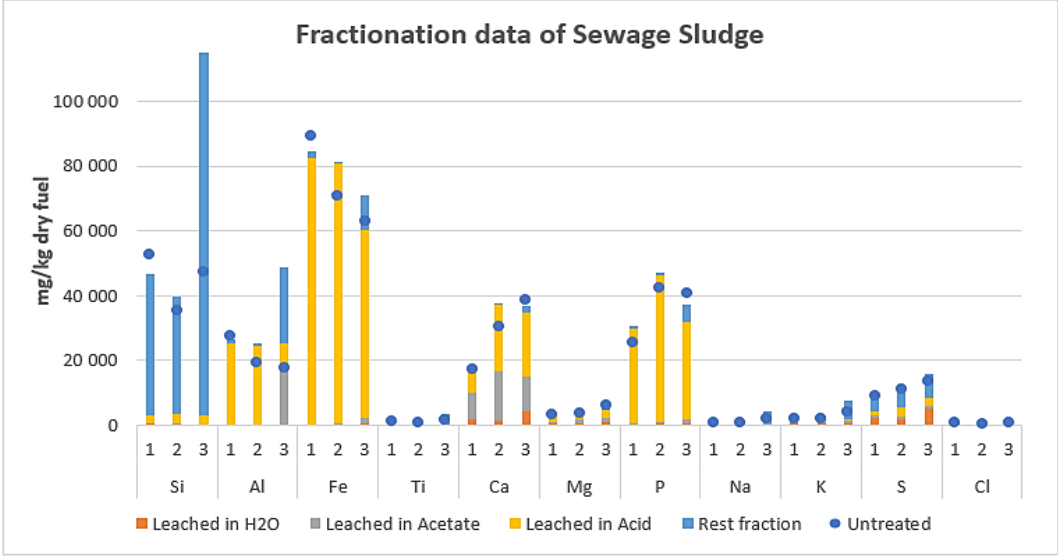

Figure 12: Fractionation results of sewage sludge.

The most noteworthy concentrations detected are those of silicon, aluminum, calcium, phosphorus, and sulfur. The concentration of aluminosilicates or zeolites in sewage sludge is typically high, as they are included in washing powder to de-harden water (Schwuger, 1996). There are suggestions that zeolites might mitigate the adverse effects of heavy metals during combustion. Nitrogen and

phosphorus are effectively removed from the sludge by coagulation during the chemical treatment, which explains the high concentrations of phosphorus. Due to the high content of iron, an iron-based coagulant is likely used. Ferric chloride or sulfate and ferrous sulfate are all widely used for phosphorus removal (Stromberg and Herstad Svard, 2012). Calcium is also found in relatively high concentrations and may originate from the stabilization of sludge with calcium-based agents (Tchobanoglous and Burton, 1991). During stabilization, calcium may react with carbonates in the sludge, which could explain the high fraction of calcium soluble in the acid phase. Zeolites undergo several ion-exchanges in the washing water, where sodium cations are usually replaced with either calcium, magnesium, or potassium cations (Pettersson et al., 2008). Organic calcium is also found in high concentrations, which is expected due to the amount of organic waste accumulating in the sewers. The fraction of calcium dissolved in the water phase is significant compared to previous sludges, around 10 % for sewage sludges nr. 1 & 2.

The combustion of sewage sludge as a primary fuel is not feasible (Stromberg and Herstad Svard, 2012). Co-combustion of lower fractions of sewage sludge together with biomass is, on the other hand, considered interesting. Although the ash content of sewage sludge is high, the characteristics of the ash species are generally regarded as positive. The melting temperatures of ash particles are increased by the high content of aluminum and calcium, and therefore improve the operational conditions in the furnace by decreasing bed agglomeration problems. Sewage sludge has also shown tendencies to hinder corrosion by reducing the number of corrosive ash species in deposits. Sulfur, which is present in high amounts in sewage sludge, is known to react with alkali species and could, therefore, be a source for corrosion reduction. Phosphorus is also known to react with alkali but does so less when calcium is also present. The properties of sewage sludge ash may be negatively affected by a higher presence of heavy metals (Stromberg and Herstad Svard, 2012). However, the high content of zeolites could potentially mitigate the harmful effects of heavy metals in combustion processes (Pettersson et al., 2008).

3.5.3 Summary of sludges

A summary of the characteristics of the sludges presented in the above chapters is shown in Table 2.

Table 2: Summary of the sludges presented.

Type of Sludge	Process Origin	Moisture (wt-%)	Ash amount (dry)	Major elements present
Fiber sludge	Primary (Sedimentary) treatment of wastewater from the pulp- and paper industry	70	2-3 %	Al, Ca, Na, Si
Biological sludge	Secondary (Biological) treatment of wastewater from the pulp- and paper industry	70	30 %	Al, Fe, Si
Chemical sludge	Tertiary (Chemical) treatment of wastewater from the pulp- and paper industry	60	10 %	Al, Ca, Si
De-inking sludge	Treatment of wastewater from de-inking sites	40	60 %	Al, Ca, Si
Sewage sludge	Municipal treatment of wastewater	70	40 %	Al, Ca, Fe, P, S

Calcium, silicon, and aluminum seem to be present in all of the sludges. For the pulp and paper-based sludges, the elements originate likely either from precipitating chemicals used during wastewater treatment or additives used during manufacturing. Although the same elements seem to be regularly present, they may behave in different ways in the flue gas channel, depending on the reactivity of the compounds present. Biological sludge seems to have been contaminated with chemicals in most cases.

When compared to the pulp and paper-based sludges, sewage sludge appears to contain a higher number of ash-forming elements in significant concentrations. As both P and S, which are closely associated with Ca, are present in sewage sludge, the behavior of calcium in a boiler will be more complicated compared to the other sludges.

4. Ash behavior

4.1 Ash formation in fluidized bed combustion

The formation of ash is a complex process, in which a fuel particle goes through several stages, where both its physical and chemical composition is gradually altered. The processes may also overlap as different areas on the fuel particles react in different ways to the combustion environment. When a fuel particle enters the furnace, its temperature will quickly rise, which will cause water evaporation and, consequently, drying of the particle. When the particle is dry, it will start to pyrolyze, meaning that organic content is volatilized. During this stage, the gases are ignited and burned with a visible flame. Highly reactive ash-elements will also be released. Char is the part of the particle remaining when all volatile species have been released. In the final stage of combustion, the char is combusted and then reduced to ashes (Reid, 1984; Zevenhoven-Onderwater, 2001).

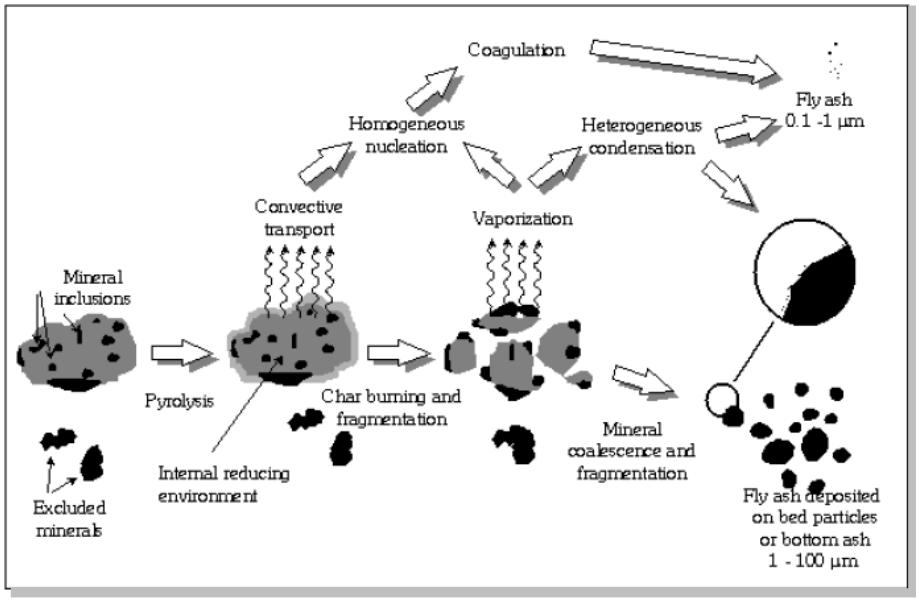

Figure 13: A simplified scheme of the ash formation process (Flagan, 1984).

Two types of ashes are typically distinguished when referring to ashes. Bottom ash consists of larger particles which remain in the bed before they are collected through the bottom of the boiler. Fly ash consists of smaller sized particles, which are transported from the furnace upwards to the second pass with the flue gas. The temperature of the flue gas decreases as it is transported through the flue gas channel, causing condensation of volatile species as the flue gas becomes supersaturated. Condensation of compounds on fly ash particles or heat exchangers is referred to as heterogeneous condensation, while the condensation of submicron particles is referred to as

homogeneous condensation. The distribution between bottom ash and fly ash is influenced by the boiler design, and the sizes and densities of the ash particles (Haynes et al., 1982).

Differences in formation mechanisms force the fly ash particles into different fractions. More reactive elements in the fuel particle can be volatilized during the beginning of the combustion process. The released gaseous species can then react through gas-gas or gas-solid reactions to form aerosols or fine ash particles. The larger ash particles tend to either remain in the bed or fragment into smaller particles during fluidization. If fragmented into a small enough size, they are entrained in the flue gases. Smaller particles can also remain in the bed if deposited on larger particles of ash or bed material.

The reactivity of ash-forming elements, as determined by the fractionation method, gives us an indication of what kind of particles will form during combustion. In biomass, alkaline metals (e.g. Na and K) are often present as compounds soluble in water and/or acetate. These compounds are highly reactive and will thus rapidly volatilize during combustion. Formation of submicron ash particles through condensation, nucleation, and coagulation will also occur. Calcium in biomass is regarded reactive when soluble either in water, acetate, or acid. As opposed to reactive alkali, reactive calcium does not volatilize and is therefore found both in the coarse fraction of fly ash and in the bottom ash (Barrosso et al., 2007; Heinzel et al., 1998). Organically associated calcium will quickly oxidize and form particles of smaller size in the flue gas. Examples of calcium-based compounds soluble in acid are calcium oxalate (CaC_2O_4) and carbonate ($CaCO_3$). It may, however, be risky to consider all CaC_2O_4 as reactive, since some CaC_2O_4 has also been suspected to remain in the rest fraction (Werkelin et al., 2012). When introduced to high temperatures in the furnace, CaC_2O_4 undergoes a series of reactions, where it forms $CaCO_3$ and finally calcium oxide CaO according to Reaction 1.

$$CaCO_3 \rightarrow CaO + CO_2 \qquad (1)$$

The reactivity of acid leached calcium carbonate has not been directly discussed, although its behavior is likely similar to that of CaC_2O_4, as it is converted to calcium carbonate between 400-500 °C. When calcium carbonate has been injected as an additive into the boiler rather than as a fuel component, calcium oxide is also rapidly formed. The formed oxide particles are, however of greater size, which makes them less reactive, as they have a smaller specific surface area. The rest fraction

typically contains calcium silicates, which are known to be inert and therefore insoluble in any of the solvents used in fractionation (Zevenhoven et al., 2012).

4.2 Deposit formation

The accumulation of (ash) deposits is mainly classified into either slagging or fouling (Bryers, 1996). Slagging refers to deposits formed on surfaces in the furnace. When given enough time the slagging deposits typically form two different layers; the inner layer is more fine-grained, while the outer layer is molten or partly molten. The chemical content of slagging is typically high in alkali and silica compounds. Fouling refers to deposition formed by fly ash particles in the flue gas channel. The inner layer of fouling deposits consists of volatile ash components, such as alkali salts, which form a sticky surface due to their lower melting temperature, making it possible for larger particles to stick to the surface (Frandsen, 2010).

Research on transportation mechanisms of ash particles towards the surfaces of heat exchangers and the mechanisms of adhesion have widely been studied. Ash particles are mainly transported by four different mechanisms to surfaces where they are then deposited; by diffusion, thermophoresis, inertial impaction, or chemical reactions with the deposit layer (Baxter, 1993). Transportation by means of diffusion can be induced by condensation (due to the removal) of ash species from the flue gas surrounding the heat transfer surface. Condensation can occur in the flue gas when small particles are formed by nucleated gaseous matter, or directly on the steel surface or on the surface of a formed deposit (Frandsen, 2010). The phenomenon known as thermophoresis is the force that drives a flow from a space with a higher temperature towards a colder. Larger ash particles become attached to the heat exchanger surface by inertial impaction. The excessive momentum of larger particles in the flue gas, causes them to collide with the heat exchanger tubes instead of following the gas flow around them. The adhesion of the particles relies on particle viscosity, the velocity of the flue gas, size, and density.

4.3 Reactivity of calcium in fly ash

The need for a better understanding of calcium impact on deposit chemistry and corrosion both in the superheater region and in the cold-end of the flue gas channel has been raised earlier in this work. In order to fully understand the behavior of calcium in the flue gas, the mechanisms of typical calcium reactions must first be analyzed. In this section, the main flue gas reactions involving calcium will be presented and discussed, based on available data and experiences.

4.3.1 Sulfation

The reaction between sulfur and calcium during combustion is mostly associated with SO_2 capture, which occurs according to the overall Reaction 2, where CaO reacts under oxidizing conditions to form calcium sulfate ($CaSO_4$). The reaction is significant for the boiler operation because lower sulfur emissions can be reached with a higher calcium concentration in the furnace. Thus, injection of limestone or co-combustion of fuels with high sulfur content together with high calcium containing fuels is typically conducted to reduce sulfur emissions. However, sulfur capture could have an impact on corrosion, as it leads to a lower availability of sulfur for the sulfation of alkali chlorides.

$$CaO + SO_2 + 0.5\ O_2 \rightarrow CaSO_4 \qquad (2)$$

In addition to $CaSO_4$, other compounds can also form in the reactions between sulfur and calcium (Anthony and Granatstein, 2000). The outcome depends mainly on temperature and the partial pressures of SO_2 and O_2. In oxidizing conditions, calcium sulfite ($CaSO_3$) is also formed, although it becomes thermally unstable at temperatures above 700 °C. In reducing conditions, calcium sulfide (CaS) can be formed as described by Reaction 3. Nevertheless, in the presence of sulfur, $CaSO_4$ is the main calcium compound formed at normal furnace temperatures in fluidized bed boilers (800-950 °C).

$$CaO + SO_2 \rightarrow CaS + \frac{3}{2}\ O_2 \qquad (3)$$

Different reaction mechanisms have been suggested for the formation of $CaSO_4$ (Moss, 1970; Moss 1975). Calcium and sulfur can either first react to form $CaSO_3$ as an intermediate, or sulfur is first oxidized to SO_3 before it reacts with calcium oxide to form $CaSO_4$. Thus, $CaSO_4$ is either formed through reactions 4 and 5 or through reactions 6 and 7. Further research of the reaction series is however still required, as researchers disagree over which the dominant route is. While some has preferred formation of $CaSO_4$ through the latter route (Lin, 1994; Schouten et al. 1995; Schouten 1989), others have argued that SO_3 is unlikely to be present in significant concentrations in the furnace during normal fluidized bed conditions (Anthony and Granatstein, 2000).

$$CaO + SO_2 \rightarrow CaSO_3 \quad (4)$$

$$CaSO_3 + 0.5\ O_2 \rightarrow CaSO_4 \quad (5)$$

$$SO_2 + 0.5\ O_2 \rightarrow SO_3 \quad (6)$$

$$CaO + SO_3 \rightarrow CaSO_4 \quad (7)$$

Sulfur capture by calcium in the fuel or in additives is an effective way of mitigating SO_2 emissions in fluidized bed combustion. However, at higher temperatures, SO_2 can become available through the decomposition of $CaSO_4$. Significant decomposition of $CaSO_4$ is, however, not expected at temperatures below 1000 °C.

4.3.2 Reactions with phosphorus

Limited research has been conducted on the reactions between calcium and phosphorus during combustion. Although their relationship is poorly understood, it is well established that they are, much like sulfur and calcium, closely associated. Together they form compounds of calcium phosphates, which are stable components with a high melting temperature (Lindström et al., 2007). A mechanism for the reaction has not been acknowledged, although it has been suggested that phosphorus is volatilized and forms orthophosphates in the flue gas, which then reacts with calcium to produce calcium phosphates (Beck and Unterberger, 2006). Beck and Unterberger suggested that calcium phosphates are formed either by condensation of phosphates on the surface of calcium particles or through a physical process that leads to the formation of small particles of calcium phosphates. Phosphorus and sulfur compete over calcium, leading to decreased formation of calcium sulfate in the furnace. The phenomenon has been observed when firing fuel mixtures containing sewage sludge, which are rich in phosphorus (Åmand and Leckner, 2004).

4.3.3 Carbonation

The reversible reaction of calcination, or carbonation proceeds according to Reaction 8. The reaction is exothermic and thus the activity of the reaction is favored by low temperatures. Carbonation typically becomes active below 800 °C, however when the temperature decreases below 600 °C the reaction rate becomes slow. Therefore, the active window of carbonation is between 600-800 °C. Carbonation can lead to sintering of deposits in the flue gas channel, causing the formation of hard deposits. The stability of $CaCO_3$ vs. CaO is presented in Figure 14.

$$CaO + CO_2 \rightarrow CaCO_3 \quad (8)$$

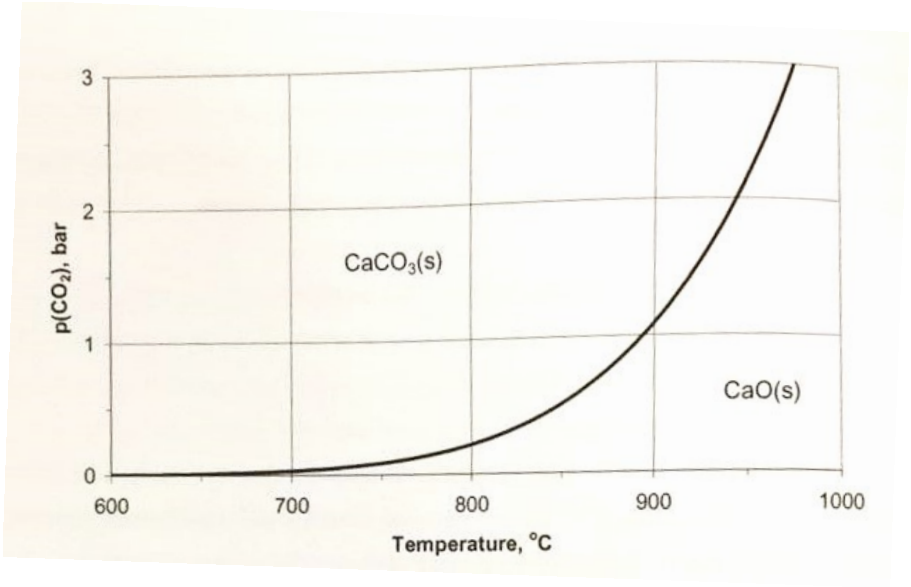

Figure 14: The stabilities of calcium carbonate and calcium oxide as a function of the partial pressue of CO_2 and temperature. (as calculated by Partanen, 2004).

4.3.4 Reaction of HCl with calcium compounds

Chlorides tend to form troublesome compounds during combustion, and $CaCl_2$ is no different. It may cause fouling in BFB boilers and contribute to corrosion, both in the superheater region and cold end of the boiler. Calcium chloride is formed according to the overall reactions 9, 10 and 11. Reaction 10 is dependent on the carbonization of CaO, according to Reaction 8.

$$CaO + 2\,HCl <-> CaCl_2 + H_2O \quad (9)$$

$$CaCO_3 + 2\,HCl <-> CaCl_2 + H_2O + CO_2 \quad (10)$$

$$Ca(OH)_2 + 2\,HCl <-> CaCl_2 + 2H_2O \quad (11)$$

Kosnyrev noticed the formation of calcium hydroxichloride (CaClOH) and the reaction of HCl with calcium compounds and suggested that it acts as an intermediate during the formation of $CaCl_2$ (Kosnyrev et al., 1981 & 1990). A further study of CaClOH reported that the intermediate itself is stable only under certain circumstances (Partanen, 2004). However, the intermediate may form easily and could, therefore, have a significant impact on $CaCl_2$ formation. A structure for the compound, which can be seen in Figure 15, was suggested by Partanen, 2004.

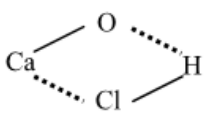

Figure 15: The structure of CaClOH as suggested by Partanen, 2004.

The stability of $CaCl_2$ versus CaO and $CaCO_3$ in the temperature interval 400-1000 °C, and at different moisture concentrations can be observed in Figure 16.

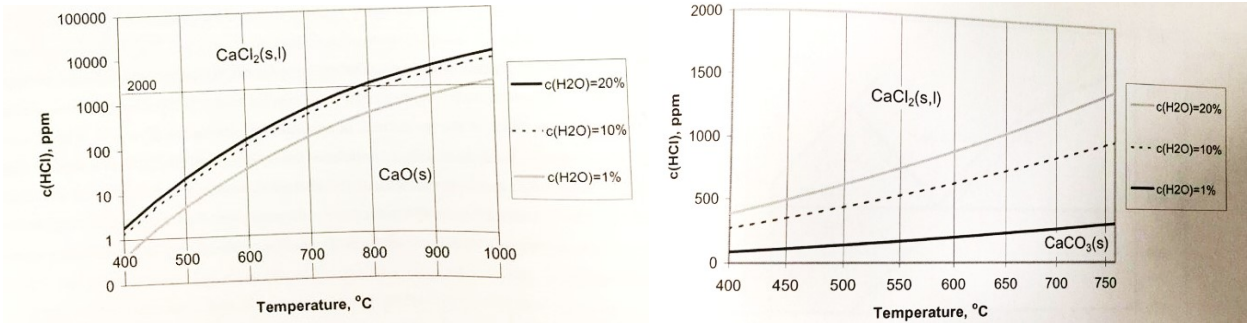

Figure 16: The stability of calcium chloride, with water ass a parameter, versus a) calcium oxide b) calcium carbonate at high flue gas temperatures (Partanen, 2004).

The figure shows that at superheater material temperatures, the formation of $CaCl_2$ from CaO requires much lower flue gas concentrations of HCl, when compared to $CaCO_3$. Therefore, the formation of $CaCl_2$ in the superheater region seems to depend on the presence of CaO mainly. The probability of formation increases along with decreasing temperature. The reaction between HCl and $CaCO_3$ to form $CaCl_2$ is much favored by low water vapor pressure, as the figure shows. When the flue gas temperature decreases below 400 °C, $Ca(OH)_2$ is thermodynamically favored (Weinell et al., 1992). The stability of $CaCl_2$ versus $Ca(OH)_2$ and $CaCO_3$ in the temperature interval 100-400 °C can be observed in Figure 17.

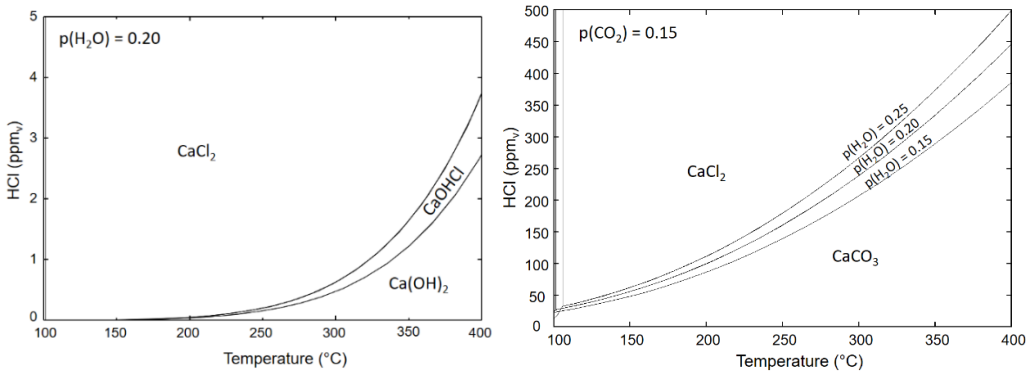

Figure 17: The stability of calcium chloride versus a) calcium hydroxide at a water partial pressure of 0.2 bar b) calcium carbonate at low flue gas temperatures, with water as a parameter (Vainio et al., 2019).

Low temperatures favor the formation of $Ca(OH)_2$ from CaO. According to thermodynamics, below 200 °C, $Ca(OH)_2$ is not stable and will form $CaCl_2$ even at very low HCl concentrations. The formation of $CaCl_2$ from $CaCO_3$ requires much higher concentrations of HCl. Even at a temperature of 100 °C, the required HCl concentration is close to 25 ppm. Therefore, the formation of $CaCl_2$ through $Ca(OH)_2$ is likely the primary mechanism at the air preheaters.

4.4 High-temperature corrosion

One of the main challenges with boiler operation is corrosion of the furnace, wall tubes, and superheater tube steel materials, which are located in the hotter part of the boiler. In case corrosion occurs, it causes significant costs due to unscheduled shutdowns, material replacement, and /or the use of higher quality materials to avoid corrosion. In 1982, problems due to corrosion were estimated to cost energy-related industries 122 billion dollars per year (Bhaskaran et al., 2005). It is therefore essential to pay specific attention to corrosion and every detail of the corrosion mechanism. It is common knowledge that corrosion in power boilers are mainly caused by chlorine-containing compounds. Primarily alkali chlorides are associated with increased corrosion rates of heat exchangers at higher temperatures. Stainless steels are a popular choice as a material for superheaters, as they are more resistant to corrosion (Folkeson, 2010). However, at high material temperatures, alkali chlorides may also cause corrosion on stainless steel. Research has shown that the alkali-cation is responsible for initiating corrosion by reacting with the protective oxide layer to form chromate, according to Reaction 12 (Lehmusto et al., 2012; Pettersson et al., 2005).

$$8KCl(s) + 2Cr_2O_3(s) + 5O_2 \rightarrow 4K_2CrO_4(s) + 4Cl_2(g) \qquad (12)$$

In conditions with a higher moisture content, reaction with the protective layer can also occur according to Reaction 13.

$$2Cr_2O_3 + 8KCl + 4H_2O + 3O_2 \rightarrow 4K_2CrO_4 + 8HCl \quad (13)$$

The formation of chromate reduces the chromium content in the oxide layer, causing it to lose its protective characteristics. The corrosion process is then accelerated as chlorine ions can penetrate the scale. Chlorine induced corrosion is a cycle mechanism during which the protective oxide layer is continuously degraded. The mechanism is also known as active oxidation (Grabke et al., 1995).

$$\frac{x}{2}Cl_2(g) + Me(s) \rightarrow MeCl_x(s) \qquad (14)$$

$$yMeCl_x(g) + \frac{z}{2}O_2(g) \rightarrow Me_yO_z(s) + \frac{xy}{2}Cl_2(g) \qquad (15)$$

Corrosion is typically aggressive when the salt is in a molten phase. Mixtures of salts often have a lower melting point than pure salts. These are referred to as eutectic mixtures. Because of the more rapid transportation of ions in the liquid phase, molten phase corrosion can proceed at much faster rates in comparison to corrosion occurring with solid-state diffusion. Calcium has typically been classified as a compound that lowers the melting temperature of eutectic mixtures. However, if

compared to alkali metals, their impact on temperature lowering is much less pronounced. In Table 3, the melting temperatures of pure salts and eutectic mixtures containing calcium has been listed. For comparison, a few compounds containing alkali metals have been included as well. The melting temperatures have been obtained from the Factsage database and Karlsson (2012).

Table 3: The melting temperatures of pure deposit compounds, some corrosion products, and some eutectic mixtures

Pure deposit compounds		Pure Corrosion products		Eutectic mixtures	
KCl	771	$FeCl_2$	677	$CaCl_2 - NaCl$	504
$NaCl$	801	$FeCl_3$	303	$CaCl_2 - MgCl_2$	617
$CaCl_2$	782	$CrCl_2$	820	CaF_2–$KCaCl_3$	650
$ZnCl_2$	318	$CrCl_3$	1150	$CaCl_2$–$FeCl_2$	585
$PbCl_2$	498	$NiCl_2$	1030	$CaCl_2$–$PbCl_2$	462
K_2SO_4	1069	K_2CrO_4	973	$CaCl_2$–□□□	744
Na_2SO_4	880	K_2CrO_7	398	$CaCl_2$–□□□	638
$CaSO_4$	1460	Na_2CrO_4	792	$CaCl_2$–□□□	596
K_2CO_3	901	Na_2CrO_7	357	K_2SO_4–Na_2SO_4–$CaSO_4$	776
Na_2CO_3	851	$CaCrO_4$	1020		
$CaCO_3$	825				

4.4.1 The role of calcium chloride

In a previous study, it has been reported how alkali and alkaline earth metals behave when coming in contact with the protective oxide layer of a 304L stainless steel at a temperature of 600 °C and an atmosphere with high moisture content (Karlsson et al., 2012). Based on an XRD analysis, it was reported that $CaCl_2$ may react with the oxide layer according to Reaction 16. However, the reaction proved to be limited as only small amounts of chromate ions were detected near the $CaCl_2$. Karlsson et al. (2012) suggested that the unstable nature of $CaCl_2$ limits the formation of calcium chromate, due to the rapid formation of CaO according to Reaction 17. Lehmusto et al. (2011) have on the other hand shown that $CaCl_2$ remains unreactive when exposed to a dry environment in the temperature range of 400-600 °C. Karlsson et al. (2012) further suggested that calcium oxide, at 600 °C and in a gas with 40% H_2O, can react with the protective oxide layer according to Reaction 18 and form $Ca_2Fe_2O_5$. They also deemed it possible for CaO to be able to react directly with the protective oxide (Reaction 19), although this is only likely to proceed near the salt deposit, as CaO was found to be quite immobile. Karlsson et al. (2012) also argued that an oxide layer consisting of $Ca_2Fe_2O_5$ might have given rise to a protective behavior.

$$Cr_2O_3 + 2CaCl_2 + 2H_2O + \frac{3}{2}O_2 <-> 2CaCrO_4 + 4\,HCl \quad (16)$$

$$2CaCl_2 + H_2O <-> CaO + 2\,HCl \quad (17)$$

$$Fe_2O_3 + 2CaO <-> Ca_2Fe_2O_5 \quad (18)$$

$$Cr_2O_3 + CaO + \frac{3}{2}O_2 <-> 2CaCrO_4 \quad (19)$$

4.4.2 Prediction of corrosion

When aiming to prevent corrosion, it is essential to build an understanding of the fuel properties and the potential risks during combustion. Basic prediction of high-temperature corrosion can be conducted by observing values of molar ratios between elements involved in essential reactions from a corrosion and deposit point of view (Stromberg and Herstad Svard, 2012). In this section, the focus will lie on molar ratios including calcium or molar ratios with elements affected by the presence of calcium. Furthermore, it is important to remain critical of the fuel indexes as they merely give an indication of how the fuel could behave in the boiler. When corrosion in the cold-end of the flue gas channel is better understood, molar ratios predicting low-temperature corrosion can also be developed.

In the previous chapter, it was stated that corrosion is reduced when alkali metals are present as sulfates instead of chlorides. Thus, it is of interest to consider the fuels' own theoretical ability to sulfate its alkali content. The molar ratio between sulfur and chlorine characterizes this ability and therefore provides an indication of alkali chloride content in the boiler deposits. A higher value (over four) presents an increased probability of a reduced amount of alkali chlorides. A value below two is typically considered to be in the risk zone of corrosion.

As sulfur and calcium are closely associated, a higher amount of calcium present in the fuel could lead to a decreased sulfation of alkali chlorides and thus increase the risk of corrosion. The molar ratio between sulfur and calcium is, therefore, important as it provides an indication of the fuels' ability to capture sulfur. A high value of Ca/S indicates that also a higher S/Cl ratio is required for the sulfation of alkali chlorides. In some cases, it is also necessary to include phosphorus in the molar ratio between calcium and sulfur, as phosphorus is also closely associated with calcium and can thus impact the fuel's ability to capture sulfur. However, this is only worth to take into consideration for fuels containing higher amounts of phosphorus. If the aim is to reduce the accumulation of chlorine

in deposits by injecting a sulfur additive or including fuel with high sulfur content in the fuel mixture, then a Ca/S molar ratio below one is considered as favorable. When the fuel mixture also includes a high phosphorus content, a Ca/(S+1.5P) molar ratio below 1.5 is considered as favorable (Stromberg and Herstad Svard, 2012). In Table 4, the calculated molar ratios of S/Cl, Ca/S and Ca/(S+1.5P) are presented for chosen examples from the fuel analysis section. Wood species was not included, due to their low ash content and data of pine bark was not found.

Table 4: Molar ratios of S/Cl, Ca/S and Ca/(S+1.5P) for the fuels presented in the fuel analysis-section.

Fuel	S/Cl	Ca/S	Ca/(S+1.5P)
Fiber sludge	25.0	0.7	0.6
Bio-sludge	7.4	0.2	0.2
Chemical	8.0	2.2	1.5
Sewage Sludge	19.2	1.8	0.3
Deinking sludge	1.9	169.0	88.0
Bark (Spruce)	0.3	39.3	13.7
Bark (Birch)	2.0	14.6	5.9
Bark (Euca)	0.1	80.0	18.6

4.5 Low-temperature corrosion at air preheaters

The main objective of combustion is to recover as much energy as possible from the flue gases. However, at some point, it becomes challenging to decrease the flue gas temperature due to rising challenges with low-temperature corrosion. For some time, it has been thought that low-temperature corrosion in biomass firing has been caused by condensed sulfuric acid as in coal firing. However, recent findings have shown that during the combustion of biomass fuels, rich in elements able to capture sulfur, the corrosion mechanism is different. During a measurement campaign conducted by Åbo Akademi University, the impact of sulfur acid (H_2SO_4) on low-temperature corrosion was investigated by conducting measurements in the second pass of a full-scale bubbling fluidized bed boiler (Vainio et al., 2016). A technique, where either SO_3 or H_2SO_4 is trapped in a KCl salt plug, was used to determine the amount of H_2SO_4 in the flue gas. The fuel was a mixture of bark, sludge, and solid recovered fuel. The sludge consisted primarily of paper-mill and sewage sludge. During the measurement campaign, no SO_3 was detected in the cold-end and instead it was suggested that the corrosion was caused by the hygroscopic salt, $CaCl_2$, due to high contents of

calcium and chlorine in the deposits on corrosion rings. The material temperatures of the probe rings were 100 °C during the measurements.

Hygroscopic salts are known to be able to cause corrosion as they form wet deposits at temperatures much higher than the water dew point (Lindau and Goldschmidt, 2008; Retschitzegger et al., 2015; Vainio et al., 2016). The formation of wet deposits occurs when hygroscopic salts present in the ash deposits dissolve in the water they absorb from the flue gas. This ability is called deliquescence and occurs when the water vapor pressure reaches above a critical point, which is specific for the hygroscopic salt in question. The critical point, which is also known as DRH (Deliquescence relative humidity), is a temperature-dependent function (Tang and Munkelwitz, 1993). Generally, salts with a higher solubility express stronger deliquescence behavior. In Table 5, examples of two salts that may be present in fluidized beds that also display hygroscopic properties, are presented.

Table 5: The hygroscopic properties of calcium and zink chloride (Retschitzegger et al., 2015).

Salt	Solubility 100g H2O	DRH (15%)moisture)	DRH (25% moisture)
$CaCl_2$	81,3 g	95 °C	110°C
$ZnCl_2$	408 g	127°C	~140°C

Based on solubility, probability of presence, and stability at low temperatures, it has been suggested that $CaCl_2$ could play an important part in low-temperature corrosion (Lindau and Goldsmith, 2008). Zink chloride ($ZnCl_2$) was also considered as another potential candidate. The ability of $CaCl_2$ to deliquesce has been determined empirically and the results are shown in a moisture concentration versus temperature diagram in Figure 18 (Vainio et al., 2019-A).

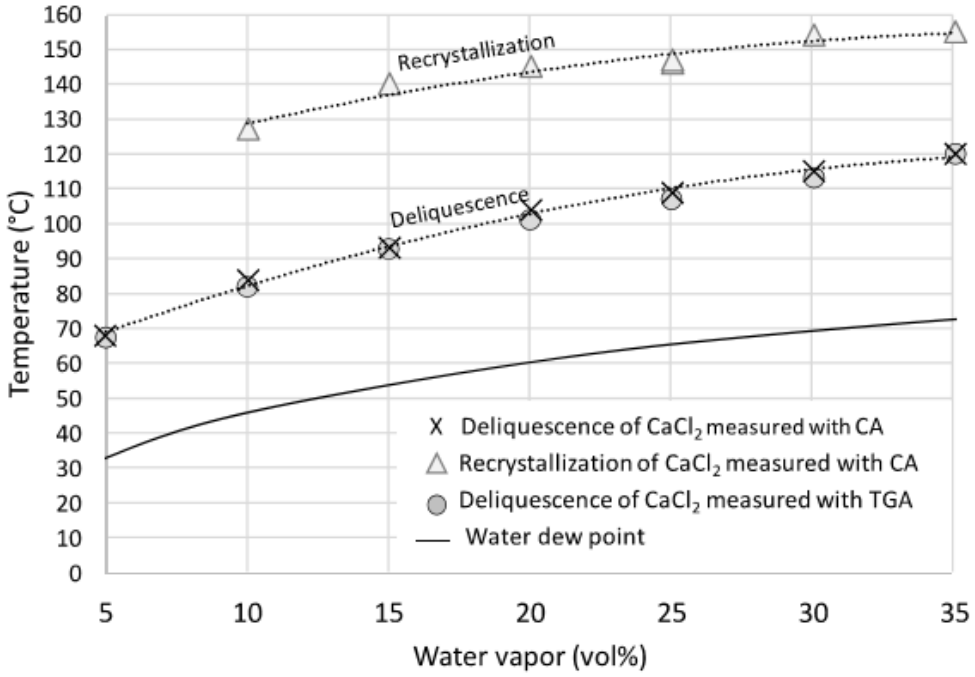

Figure 18: The deliquescence of calcium chloride at different water vapor pressures (Vainio et al., 2019-A).

The figure shows that at a flue gas moisture of 18%, which can be considered a normal level during biomass combustion, the deliquescence of $CaCl_2$ occurs at 100 °C. At higher moisture levels, the DRH temperature also increases. The flue gas temperature is typically operated at temperatures well above this, 130-150 °C are considered low flue gas temperatures in the air preheater section. Therefore, $CaCl_2$ does not deliquesce in the flue gas. However, in some plants, the material temperature of the air preheaters can be lower, due to lower feedwater temperatures. Accordingly, the risk of wet deposit formation increases.

The lack of knowledge in the area of low-temperature corrosion at air preheaters generally causes much uncertainty about the flue gas temperature in this section and at what level it needs to be maintained. Typically, a lower safety temperature is determined based on the dewpoint of sulfuric acid. However, the reported findings from the research conducted by Åbo Akademi University has pointed out significant flaws in this strategy and highlighted that the operational temperature at the air preheaters needs to be determined based on the behavior of hygroscopic salts instead. Although first, the understanding of hygroscopic salts must be improved by further research.

5. Experimental

The behavior of calcium was investigated at different temperatures during a measurement campaign in a 150 MW bubbling fluidized bed boiler burning bark, fiber sludge, forest residues and wood chips. During the campaign, samples of the fuel, fly and bottom ash fractions were collected for determination of their chemical composition. Deposit probe measurements were conducted using Valmet and ÅA manufactured air-cooled probes. Initially, only 2 h measurements were planned to be conducted in the superheater region. However, the low amount of deposit yield led to a change of plans, and thus two longer measurements were conducted at the secondary and primary superheater locations as well. The deposit samples collected were further analyzed by means of SEM/EDX (Scanning electron microscope, energy-dispersive X-ray) to gain information about their chemical compositions and structures. The deposit build-up rate was also evaluated for all samples. TGA (Thermogravimetric Analysis) analysis was only performed on the deposit collected during the longer exposure at the primary superheater due to the low amount of deposit yield. XRD (X-Ray diffraction) was conducted as a final analysis of two chosen samples.

5.1 Background

Now that the interest in combustion of sludges has increased, a better understanding of the impact high amounts of calcium will have on the deposit chemistry, is required. At the moment, there is a lot of question marks surrounding the corrosivity of calcium compounds. It is unclear if calcium is directly involved in high-temperature corrosion or promotes conditions that are suitable for corrosion (Karlsson et al., 2012; Choi, 1985). It has been shown that hygroscopic $CaCl_2$ is corrosive when present as a wet deposit (Vainio et al, 2016). However, more research is required to clarify the role of calcium on corrosion in the cold-end of the flue gas channel, as well as its formation. Therefore, it was decided to conduct a measurement campaign in a BFB-boiler firing a calcium-rich fuel, to gain more information about the behavior of calcium in the boiler. The BFB boiler of Bomhus Energi Ab was chosen for the measurements.

5.2 Test site

The power boiler in which the measurements were conducted is a full-scale BFB with a thermal efficiency of 150 MW and a steam flow of 57 kg/s at a temperature of 520 °C and a pressure of 120 bar. The boiler is located in the municipality of Gävle in east-central Sweden and produces electricity, hot water for local district heating, and steam for industrial applications. Waste streams from the nearby paper production facilities of BillerudKorsnäs AB; bark, wood chips, and fiber sludge are the primary sources of fuel. The fiber sludge contains high amounts of calcium, which originates from the packaging board coating process. The chlorine content of the fuel mixture is rather low (0.14 wt-% d.s).

In Figure 19, a schematic image of the boiler is presented. The boiler itself is equipped with ammonia injection to reduce the formation of nitrogen oxides. The flue gas passes a catalyst to reduce the amount of ammonia and nitrogen oxides further. During the measurements, no detection of (SO_2) was made in the flue gas leaving the chimney. The amount of HCl was also low (max. 0.27 ppm).

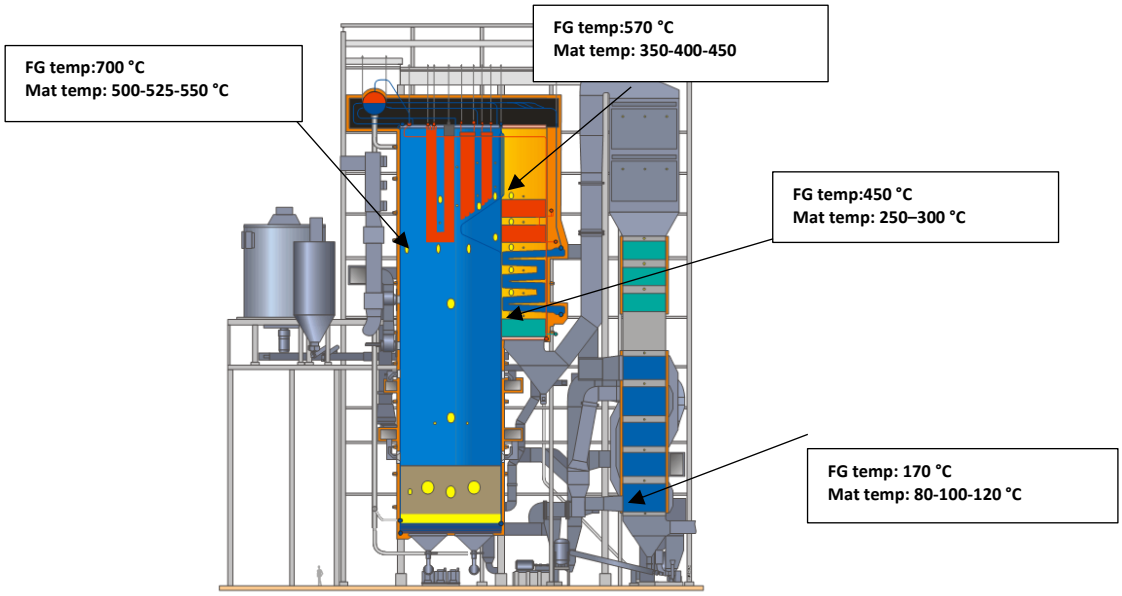

Figure 19: A schematic image of the boiler with the measurement locations pointed out.

In total, four different locations in the boiler were used as measurement points during the campaign. Measurements at higher flue gas temperatures were conducted just below the secondary superheater and at the primary superheater (Figure 19). At these measurement points, the impact of calcium on high-temperature deposit chemistry and corrosion was studied. Measurements at locations with lower flue gas temperatures were conducted at the economizer and air preheaters. In the economizer area, very little deposit was accumulated on the probe rings, and the

measurement point is therefore excluded from the discussion. A corrosion probe was used for the measurements at the air preheaters, as it made it possible to conduct tests with different materials and material temperatures at the same time. The objective of these tests was to gain more information about the corrosive behavior of $CaCl_2$. In Figure 19, all measurement points are marked along with the material temperatures used for the probe rings and the average flue gas temperature at the location. The standard chemical compositions of the materials used during the measurements are shown in Table 6.

Table 6: The standard compositions of the materials used during the measurements.

Main alloying elements [wt-%]					**Steel grade**	
C	**Cr**	**Ni**	**Mo**	**Other**		
≤ 0.2	≤ 0.3	≤ 0.3	≤ 0.08	Mn, Si, Fe	**P265GH**	Carbon steel
0.12 - 0.2	≤ 0.3	≤ 0.3	0.25 - 0.35	Mn, Si, Fe	**16Mo3**	Low-alloy steel
0.08 - 0.12	8 - 9.5	≤ 0.4	0.85 - 1.05	Mn, Si, V, Nb, Fe	**X10CrMoVNb9-1**	High-alloy ferritic steel
≤ 0.035	18 - 20	8 - 13		Mn, Si, N, Fe	**TP304L**	Austenitic stainless steel

5.3 Method

The deposit measurements were conducted using air-cooled probes inserted at different positions in the boiler. Deposit probes are sampling devices, which commonly consist of merely one material and temperature zone. The material temperature is maintained by an air-flow inside the device, which is regulated by a valve. The probe requires connections to an external source for air and electricity. The design and function of a corrosion probe are similar to that of a deposit probe, the only difference being that more parameters can be studied at the same time as a corrosion probe sometimes has several temperature zones. Deposit samples were taken from three positions on the exposed rings; wind, side and lee. A schematic figure of a deposit probe and the placement of the sampling locations are explained in Figure 20.

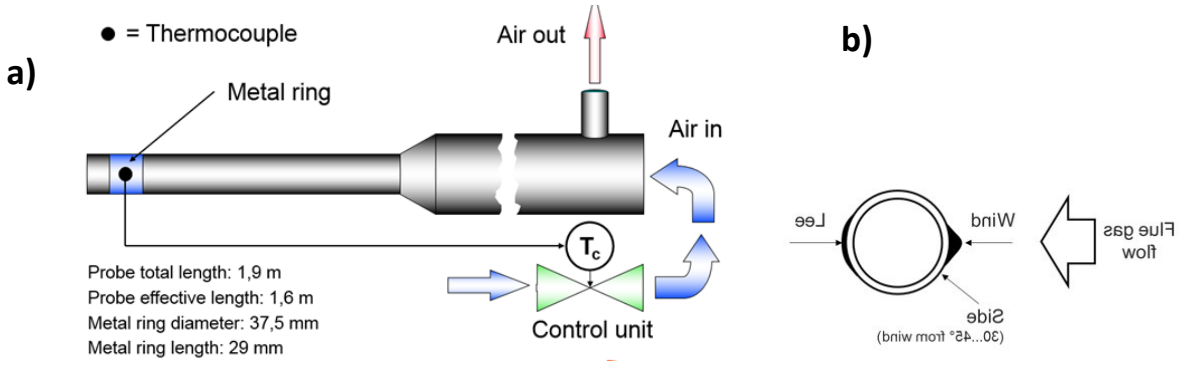

Figure 20: a) A schematic figure of a deposit probe. b) The analyzing principle of the deposit samples. Side location indicated at 30 – 45° from the wind side.

In most of the measurements, the deposit probes were installed in connections located in the opening of man doors. Examples of the connections and the corrosion probe in use can be observed in Figure 21.

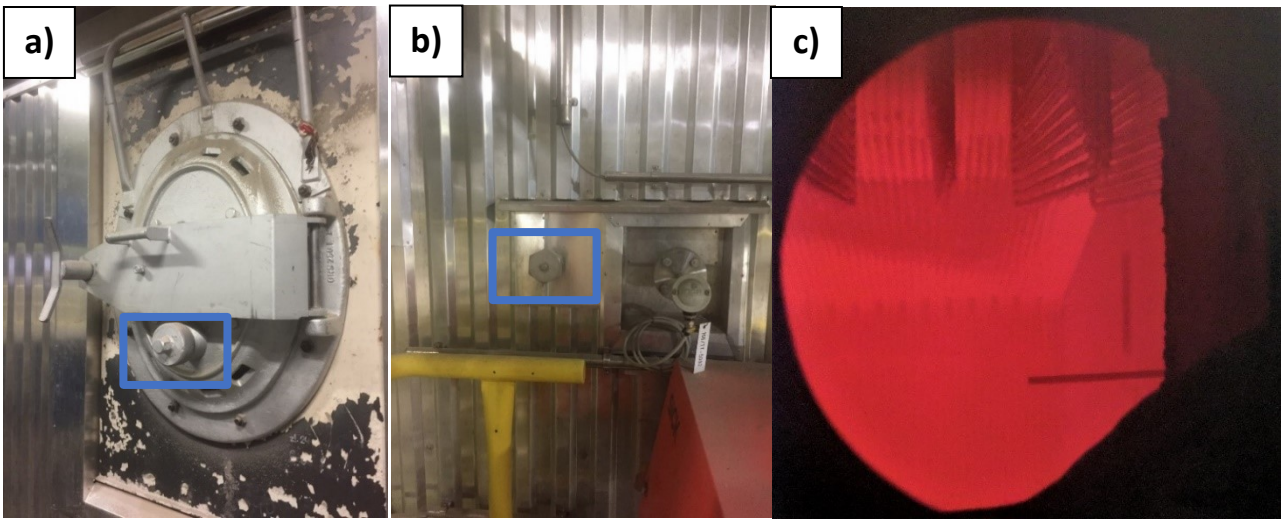

Figure 21: a) A measurement connection located in the opening of a man door is highlighted. b) A measurement connection located below the air preheaters is highlighted. c) Image of the corrosion probe in use just below the SSH.

5.4 Deposit analysis

5.4.1 Rate of deposit build-up (RBU)

The RBU is defined as the amount of deposit collected per projected surface area of the probe per unit time (g/m^2h). By weighing the probe rings before and after exposure, the rate of deposit build-up (RBU) was determined.

5.4.2 Corrosion rate index (CRI)

The CRI is defined as the decrease in thickness of the probe ring per unit time (µm/h). The corrosion rate index was determined by comparing the weight of the probe rings after being washed in acid, to the original ring weight.

5.4.3 SEM-EDX (Scanning electron microscope, energy-dispersive X-ray)

The SEM analysis was conducted under high-vacuum with an SEM instrument of model Leo 1530 Gemini SEM. The instrument was also equipped with a Thermo Scientific Ultradry EDX-system, which was utilized to screen the elemental composition of selected areas on the deposit samples. The acceleration voltage of the microscope was set at 20 kV for both the imaging and EDX-analysis. The magnification of the images was 30x, the pixel size was 3,906 µm. The signal used during imaging was of the type QBSD, meaning that the images were generated with radiation of backscattered electrons (Lloyd, 1987). This type of radiation highlights differences in mass on the sample surface

by displaying areas containing heavier molecules with a lighter shade and areas containing lighter molecules with a darker shade. Only images generated with backscattered electrons will be displayed in this work.

5.4.4 XRD (X-Ray diffraction)

Two samples in which $CaCl_2$ possibly was identified in the SEM-analyses were were analysed by XRD. With XRD the phases of the crystalline matter present can be determined by scanning the intensity of diffracted signals. The analysis was conducted using an instrument of model Bruker AXS D8 Advance powder X-ray diffractometer, which system was operated in 2θ mode utilizing CuKα radiation. A Våntec-1 linear detector was used to detect the diffracted signal. The phases present were identified by comparing the diffractograms to the PDF4 database. The weight fractions of the phases present were then estimated by Rietveld refinement, utilizing crystal data from the inorganic crystal structure database (ICSD).

5.4.5 TGA-DTA (Thermogravimetric analysis-Differential thermal analysis)

The thermal behavior of a deposit sample collected at the primary superheater was analyzed with a TGA-apparatus. In the analysis, the sample and a reference sample, which in this case was calcium carbonate, was heated up to 1000 °C. The weights and the temperature difference between the samples were also monitored. The objective of the analysis was to increase the understanding of the deposit composition, by analyzing the phase changes.

5.5 Fuel and ash analysis

The typical fuel mixture fired on the site consists of bark, wood chips, forest residues, and fiber sludge. During the measurement campaign, mainly fiber sludge and bark of birch-wood was fired.

Figure 22: Photographs of dried fiber sludge (left), samples of wood chips, forest residues and bark (center), and a close-up of the bark sample (right). The photographs were taken at the site during the measurement campaign.

Although the sludge is referred to as a fiber sludge at the site the sludge is, in fact, a mixture of sludge formed during the primary and secondary treatments of wastewater from paperboard manufacturing at the nearby facility. Sludges collected from other sources could also be included, for example, sludge from the lime kiln. Mechanical and sun-drying is utilized to lower the moisture of the sludge. No difficulties with handling the sludge have been experienced.

In Table 7, fuel analysis data for the separate fuels and the fuel mixture are presented. The data of the fiber sludge was obtained from a fuel analysis conducted on a sample taken during the measurement campaign. The fuel data of birch bark was obtained from the Fuel Database of Valmet Technologies Oy. The composition of the fuel mixture was calculated based on the individual fuel data. The wet fuel share was used for the calculation, because of the small differences in moisture shares.

Table 7: Some analyses data and properties of the fuel mixture, fiber sludge, and bark.

		Fuel mixture (calculated)	Fiber Sludge	Bark
Fuel share in mixture	wt-%, wet		13	87
Moisture	wt-%	47,5	49,6	45,15
Dry solids composition				
Carbon, C	wt-% ds.	49,82	28.2	53.05
Hydrogen, H	wt-% ds.	5,22	3	5,55
Nitrogen, N	wt-% ds.	0,31	0,38	0,3
Oxygen, O	wt-% ds.	36,20	30,1	37,11
S	wt-% ds.	0,05	0,22	0,03
Cl	wt-% ds.	0,01	0,039	0,01
Ash content 815°C	wt-% ds.	9,28	38,20	3,95
Higher heating value	MJ/kg	19,24	9,56	21,02
Major Elements				
Ca	mg/kg fuel ds	31771	178 012	9919
Mg	mg/kg fuel ds	987	2 407	775
Na	mg/kg fuel ds	375	1 222	249
K	mg/kg fuel ds	1808	879	1947
P	mg/kg fuel ds	438	2100	384
Fe	mg/kg fuel ds	711	1 986	520
Al	mg/kg fuel ds	4022	25 976	742
Si	mg/kg fuel ds	7447	32 776	3662
Fuel Indexes				
S/Cl molar ratio in the fuel		5	5,6	3
Ca/S molar ratio in the fuel		63,5	178	33,1

Overall the fuel mixture appears to be combustion-friendly. The inclusion of sludge in the fuel mixture raises the levels of calcium, aluminum, and silicon dramatically. These elements may impact on the combustion positively by increasing the melting temperature of ash compounds. Aluminosilicates may also capture alkali and release chlorine into the flue gas, thereby limiting corrosion. From a corrosion point of view, the molar ratio of the S/Cl ratio can be considered reasonable. However, the amount of calcium in comparison to sulfur in the fuel mixture is also high, as the Ca/S molar ratio shows. The high content of calcium available will undoubtedly decrease the sulfation of alkali chlorides in the flue gas. Therefore, the S/Cl ratio must be regarded with caution. The amount of alkali in the fuel is considerable.

The sulfur content of the fuel mixture is low, and the chlorine content even lower. Based on the molar ratio of S/Cl alone, it could be assumed that the fuel is not corrosive. However, the calcium will most likely react with most of the formed SO_2, allowing more chlorine to form potassium chlorides. Therefore, some alkali chloride deposition is to be expected.

The ash composition of the fuel mixture, presented as atomic percentages of the major elements, is shown in Table 8. The shares will be used for comparison with SEM/EDX results to clarify the enrichment of elements in the deposit. The enrichment of chlorine is of particular interest.

Table 8: The atomic shares calculated from the sum of all major ash forming elements in the fuel mixture.

Element	At-%
Ca	81.4
Mg	1.53
Na	0.55
K	4.52
P	0.87
S	1.02
Fe	1.34
Al	1.23
Si	7.22
Cl	0.31

In Figure 23, fractionation data of the fiber sludge sample from Bomhus, and of a reference of a birch bark sample are presented. The fractionation data of the birch bark was obtained from the Fuel Database of Valmet Technologies Oy. The figures show that most of the alkali content in the bark is in reactive form, as opposed to alkali in the sludge. Large shares of the most abundant

elements, calcium, aluminum, and silicon were all found in the rest fraction, indicating that some calcium-aluminosilicates-based compound has been used as coating-agent during cardboard manufacturing. Calcium-aluminosilicates do not decompose during combustion and therefore do not influence on the content of calcium oxide, calcium carbonate, and calcium sulfate particles in the flue gas.

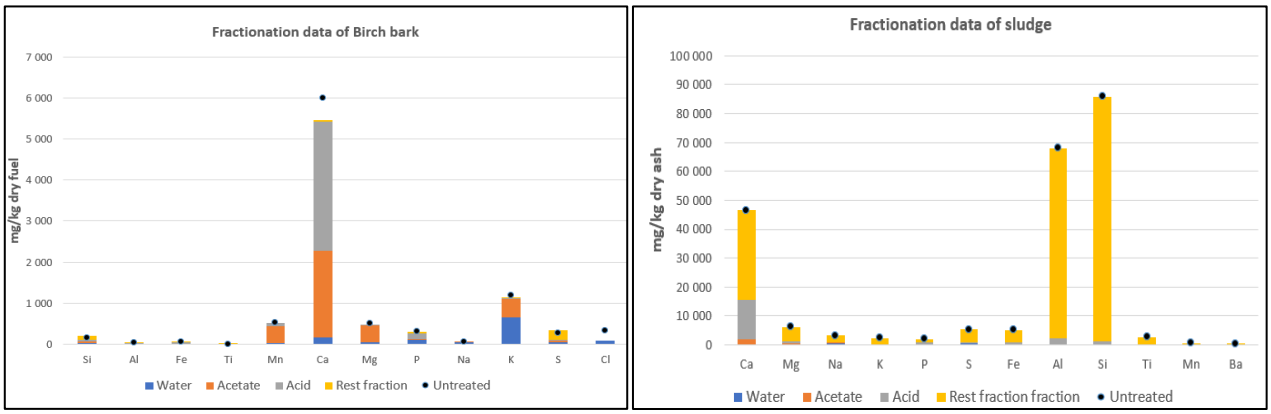

Figure 23: Fractionation results from the fiber sludge sample obtained in Bomhus and one birch bark reference obtained from the Valmet Fuel Database.

Photographs of the bottom ash and the fly ash , which were taken during the measurement campaign, are presented in Figure 24.

Figure 24: Photographs of the bottom ash (left) and fly ash (right) collected at the site.

The site has gathered monthly data on the quantities of disposed bottom and fly ash. On average, 14% of the ash forms bottom ash, and 87% fly ash. A rough estimation of the elemental distribution between bottom ash and fly ash can be made based on this data and the results from the IC analyses conducted on both ash fractions. The results are presented in Table 9.

Table 9: The distribution of ash-forming elements between bottom ash and fly ash.

Major Elements	Bottom ash(mg/kg, ds)	Fly Ash (mg/kg, ds)	Bottom ash	Fly Ash
Ca	10780	266600	4 %	96 %
Mg	2520	2666	49 %	51 %
Na	2100	7310	22 %	78 %
K	7000	20640	25 %	75 %
P	294	4128	7 %	93 %
Fe	1400	6708	17 %	83 %
Al	6160	36980	14 %	86 %
Si	37800	94600	29 %	71 %

The results indicate that both calcium and phosphorus are almost entirely entrained in the fly ash, while, of these elements, magnesium seems to have the highest tendency to stay in the bed. The large share of silicon detected in the bottom ash originates most likely from the bed material.

6. Results and Discussion

In this chapter, the results from the measurement campaign, gained by the analysis methods mentioned in the experimental chapter, will be presented. The results gained from different measurement points will be discussed separately.

6.1 Secondary superheater area (SSH)

The results from the short-term deposit measurements just below the secondary superheater (SSH) are presented in this section. In addition to the 2 h short-term deposit measurements, a 4 h test was also conducted with a material temperature of 525 °C. The measurements are listed in Table 10.

Table 10: The tests done in this study just below the SSH.

Sample	Material temperature, °C	Material	Duration, h
A	550	X10CrMoVNb9-1	2
B	525	X10CrMoVNb9-1	2
C	525	X10CrMoVNb9-1	4
D	500	X10CrMoVNb9-1	2
E	450	X10CrMoVNb9-1	2

The appearances of the exposed rings were similar. On all of the deposit probe rings from this measurement point, larger particles accumulated likely by inertial impact on the wind side, while the fine ash particles accumulated on the side and lee position, likely by diffusion or thermophoresis.

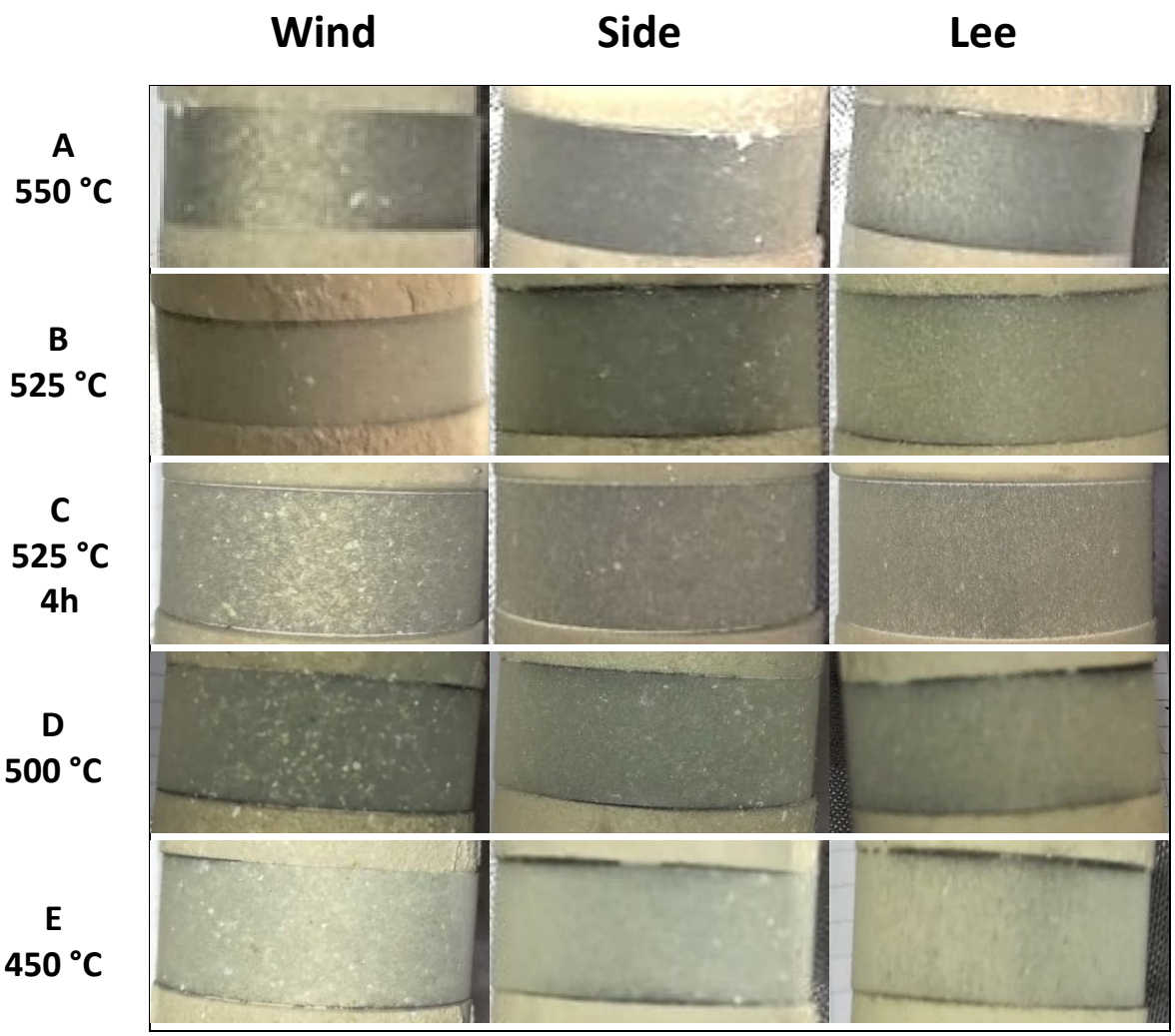

Figure 25: Probe samples from the measurements just below the SSH.

Clear corrosion on Sample A, which had the highest material temperature, was observed after exposure. When the material temperature of the probe ring decreased, spalling of some corroded material occurred and flakes detached from the metal surface. The corroded ring is displayed in Figure 26. Spalling also occurred on the side and lee positions of Sample C, although no detachment of flakes was observed. The outer surfaces of the B, D, and E steel rings were clearly more intact, and no clear signs of corrosion could be observed by visual inspection.

Figure 26: A photograph of the corroded ring (Sample A).

The RBU values for each test run are presented below in Figure 27, along with the flue gas temperatures during each measurement. An RBU value exceeding 20 g/m^{2}h is considered to be problematic and has been marked in the figure for comparison (Skrifvars et al., 2005). The error margin for Sample A may be more significant compared to the other ones, because of the spalling of the ring.

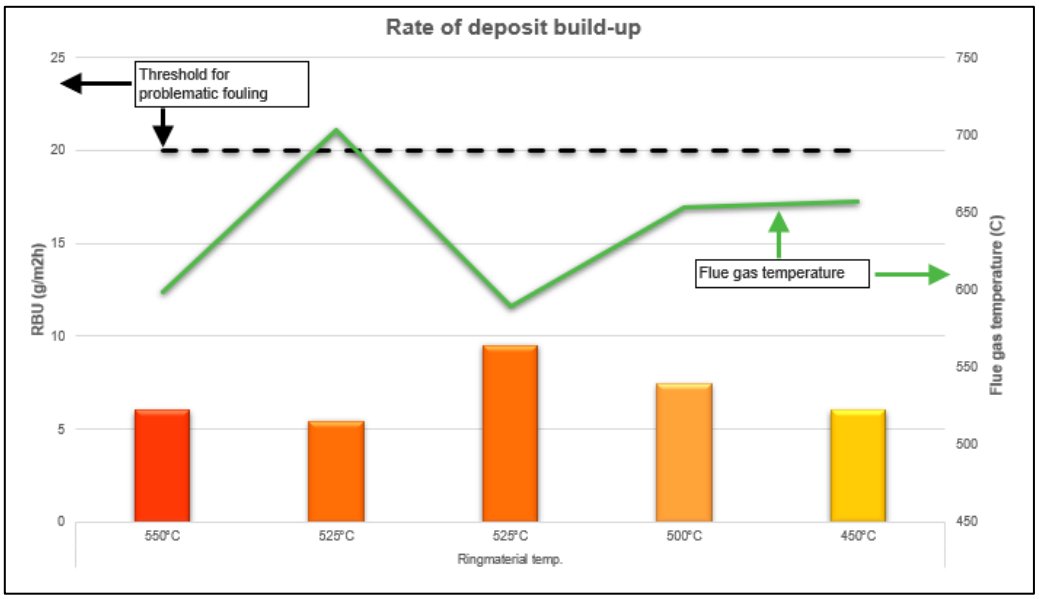

Figure 27: The RBU values for the samples collected just below the sec. superheater.

Overall, the deposit build-up during the deposit probe measurements can be regarded as rather low, maybe somewhat lower than expected. Even the highest measured RBU values are well below the threshold for problematic fouling. The boiler was operated at low load during the measurements, hence the low flue gas temperatures in the superheater area. The average flue gas temperature was below the melting point of pure KCl for all tests. The low flue gas temperatures may, therefore, have contributed to the relatively low deposition rates by decreasing the melting of ash particles in the flue gas. Other parameters influencing the rates may be the high content of compounds with high melting points, such as calcium aluminosilicates, which presence was

indicated by the fuel analysis. These compounds are known to have higher melting temperatures in the range of 1300-1500 °C (anorthite, gehlenite, grossular, gismondite) (Vassilev et al., 2013). The large share of other calcium compounds in the sludge also contributes to a higher melting temperature of the fly ash (Scala and Chirone, 2006; Scala and Chirone, 2008). Accordingly, the inclusion of sludge appears to decrease ash induced problems in the combustion process.

In Figure 28, SEM-images of deposit samples collected during the measurements just below the secondary superheater are presented. In some cases, the low amount of deposit that was collected made it challenging to scrape of the sample for SEM/EDX analysis. In all SEM-images, the positions of area and spot analyses conducted are marked. In the EDX results presented in Figure 29, elemental oxygen has been excluded from the composition.

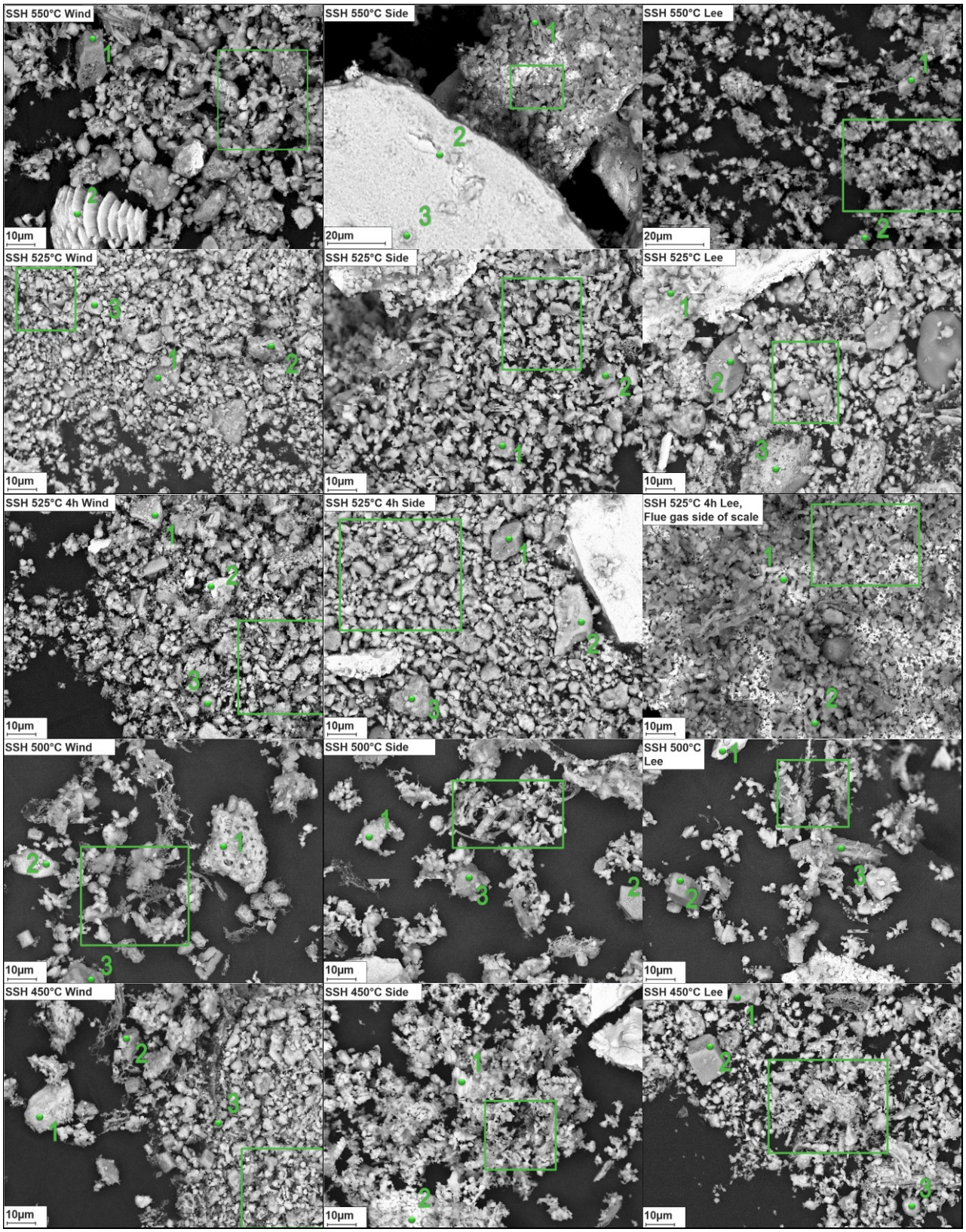

Figure 28: SEM images of the samples collected just below the secondary superheater.

Figure 29: The elemental composition for the area and spot analyses conducted on the samples collected just below the secondary superheater (SSH). Oxygen has been excluded. The units of the y-axes and the color codes of the elements are the same for or all graphs.

The area analyses show that the content of the deposit is largely dominated by calcium, irrespective of the analysis location on the ring, and the material temperature. Sulfur and potassium were also present in significant quantities. The other major elements which were found in notable shares in the deposit were sodium, magnesium, aluminum, silicon, phosphorus, and chlorine. The shares of aluminum, sodium, sulfur, and chlorine (when detected) seemed to be heavily over-represented in the deposit when compared to their shares in the fuel. Silicon was detected in similar quantities when compared to the fuel content.

Some differences in the ash compositions could be observed between the analysis positions on the rings. More calcium seemed to accumulate on the wind and lee positions of the ring (around 50 at-%) compared to the side position, where the lowest detected amount was 20 at-% (Sample A). In combination with the lower calcium content, higher amounts of chlorine, sulfur, and potassium were typically observed on the side position. The lower calcium and higher chlorine content contribute to a lower melting point of the ash. However, the system does not have a low enough melting temperature to explain the melted ash formed on the side position of Sample E (material temperature = 450 °C). If the ash has not melted in flight, one possible explanation could be the presence of iron chloride (Side, Spot 1), which may contribute to a lower melting temperature. The binary systems KCl-$FeCl_2$ and NaCl-$FeCl_2$ have several eutectic points below the material temperature in the interval 340-394 °C. The melting temperatures were obtained from the Factsage database.

The size range of the particles present in the deposit is roughly between 0,1-30 µm (indicated by the scale bar). The types of particles encountered in the deposit are discrete particles above a size of 10 µm, coarse particles with a size below 10 µm, and fine ash particles. According to the spot analyses, calcium was recurrently detected in high quantities in larger particles. It is not clear whether the calcium is present as oxide or carbonate, as the oxygen content in SEM analyses is not very accurate. However, the elemental compositions of the spot analyses, in combination with the stability diagram as presented in Figure 14, supports the assumption that calcium is mainly present as a carbonate in this measurement point. The O/Ca molar ratio for particles dominated by calcium is presented in Figure 30. As the figure shows, the overall high O/Ca ratio indicates a significant presence of calcium carbonate.

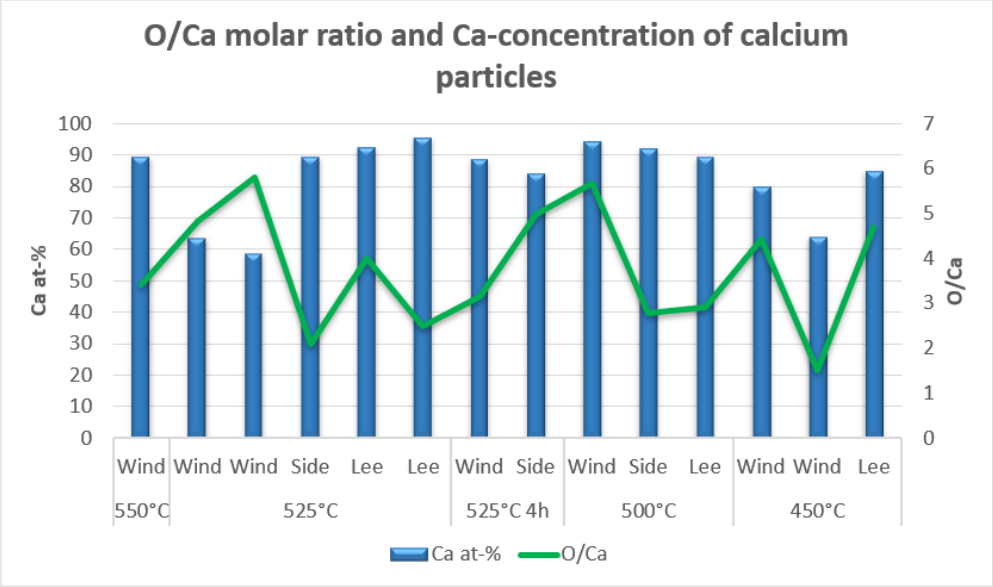

Figure 30: The O/Ca molar ratio and the atomic calcium share of discrete calcium-based particles collected before the secondary superheater.

The flue gas temperature during the measurements before the secondary superheater varied between 589 and 703 °C. As has been noted before, the re-carbonization of calcium oxide is mainly active in at 600-800 °C (Zevenhoven et al., 2012). Therefore, the formation of calcium carbonate in the deposit will most likely occur before the secondary superheater and not at the other measurement point close to the primary superheater. Calcium, aluminum and silicon were also detected in larger quantities (Sample D wind spot 1, Sample C side spot 3) with magnesium (Sample C side spot 2) and alkali (Sample E wind spot 3, Sample A lee spot 2, Sample D side spot 2) sometimes included in these systems. Furthermore, particles, which shapes resemble the trigonal crystal structure of $CaCO_3$ (Sample D Lee spot 2) were observed in the SEM images. In spot analysis 2 of Sample E (lee) a cubical particle that resembles the crystal structures of CaO and calcium oxalate was also observed. These particles appear to be less frequently encountered compared to the trigonal structures.

The deposit that was collected just below the secondary superheater, can be described as somewhat aggressive, due to the high levels of chlorine. The chlorine contents were higher than expected in the area analyses on the side position of the Samples C, D, andE, which material temperatures were 525, 500 and 450 °C, respectively. The contents were 21 to 27 times higher in comparison to the chlorine share in the fuel ash. All chlorine enrichment coefficients are presented in Table 11. Based on the continually high atomic percentages of both potassium and chlorine detected in the area analyses conducted on the side and lee positions (Figure 29), and on the chemical composition of

some spot analyses with higher chlorine contents (Sample C lee, spots 1 & 2; Sample D lee spot 3), chlorine seemed to be mainly present as alkali chlorides. At this measurement location, there was no indication of $CaCl_2$ formation according to the EDX results.

Table 11: Chlorine enrichment coefficients in deposits collected before the secondary superheater.

Sample	Position	Chlorine enrichment coefficient
A (550 °C)	Wind	4.9
	Side	No Cl
	Lee	No Cl
B (525 °C)	Wind	5.7
	Side	16.4
	Lee	13.1
C (525 °C 4 h)	Wind	2.0
	Side	21.1
D (500 °C)	Wind	4.6
	Side	20.7
	Lee	20.3
E (450 °C)	Wind	5.8
	Side	26.5
	Lee	10.1

Evidence of corrosion was also found in the deposits. Of all samples, at least one detection of iron chloride was made. Detached scales from ring A and from the lee position of Ring C were further examined for details about the corrosion mechanism. SEM images of the scales of Ring A are presented in Figure 31.

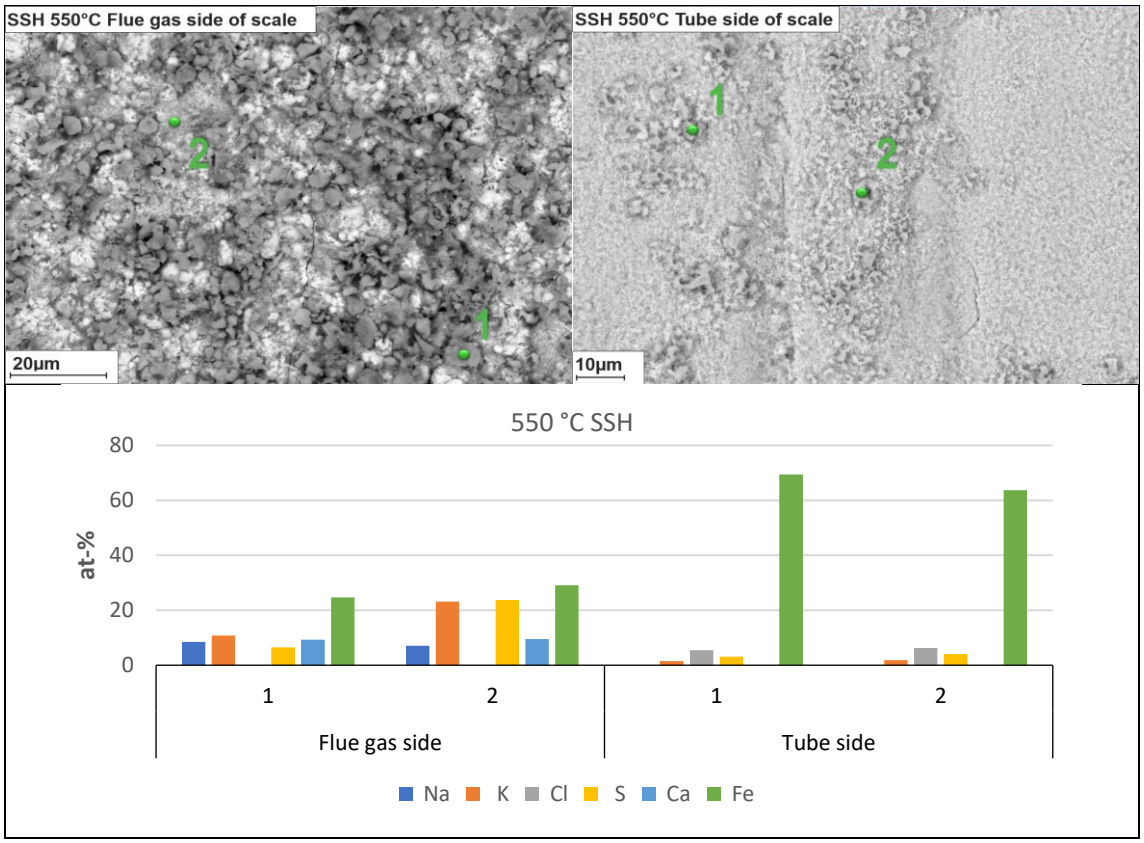

Figure 31: SEM/EDX results of the oxide scale collected from Ring A with a material temperature of 550 °C.

The spot analyses conducted on the detached flake revealed that it consisted of high amounts of iron oxide, which is a corrosion product. High amounts of alkali, calcium and sulfur were detected together with iron oxide in the spot analyses conducted on the flue gas side of the flake, suggesting that alkali induced corrosion had occurred. The alkali chlorides had likely been consumed as chlorine was not detected on the flue gas side. Significant amounts of chlorine were, however, detected on the tube side of the flake. Chlorine was likely present as iron chlorides on the tube side of the scale, based on the low amounts of potassium detected at the same location. On the scale of Ring C, the alkali chloride salts had not been consumed, indicating that the corrosion was at a less progressed stage in comparison to Ring A (Sample C, lee, spots 1 & 2).

The initial thought of the corrosion was that the high content of calcium might cause a decreased formation of alkali sulfates, as calcium captures sulfur, leading to an increased presence of alkali chlorides in the deposit. It appears some sulfation of alkali chlorides have occurred as they are regularly detected together in area analyses in the deposit. Some detections of alkali sulfates have also been made in the spot analyses (Sample C wind spot 2, Sample E side spot 2). However, based on the alkali induced corrosion and the amount of alkali and chlorine detected in the deposit, the effect seems indeed decreased.

It has been stated that aluminosilicates are known to restrict the effects of high-temperature corrosion by reacting to form potassium-aluminosilicates. However, based on the amount of chlorine and potassium accumulated in the deposits, it can be determined that no clear sign of corrosion limitation by aluminosilicates was observed in this case. In some spot analyses, alkali-species have been detected in the Ca-Al-Si systems, but for the most part, this system seems to remain unreactive in the flue gas and in the deposit.

6.2 Primary superheater measurements

The results from the measurements at the primary superheater (PSH) are presented in this section. The samples, along with their ring material temperature, are listed in Table 12.

Table 12: List of the test runs conducted at the primary superheater.

Sample	**Material temperature,°C**	**Material**	**Duration, h**
F	450	X10CrMoVNb9-1	2
G	400	X10CrMoVNb9-1	2
H	400	X10CrMoVNb9-1	12

If the accumulation of deposit just below the secondary superheater was low, it was even lower at the primary superheater. As shown in Figure 32, some probe rings even reflected light when photographed. At the time it was deemed unclear if the 2 h short-term probe tests could provide reliable data, due to their low sample amounts. Therefore, it was decided to conduct an additional 12 h overnight test at this measurement point with the aim to gather a more representative sample.

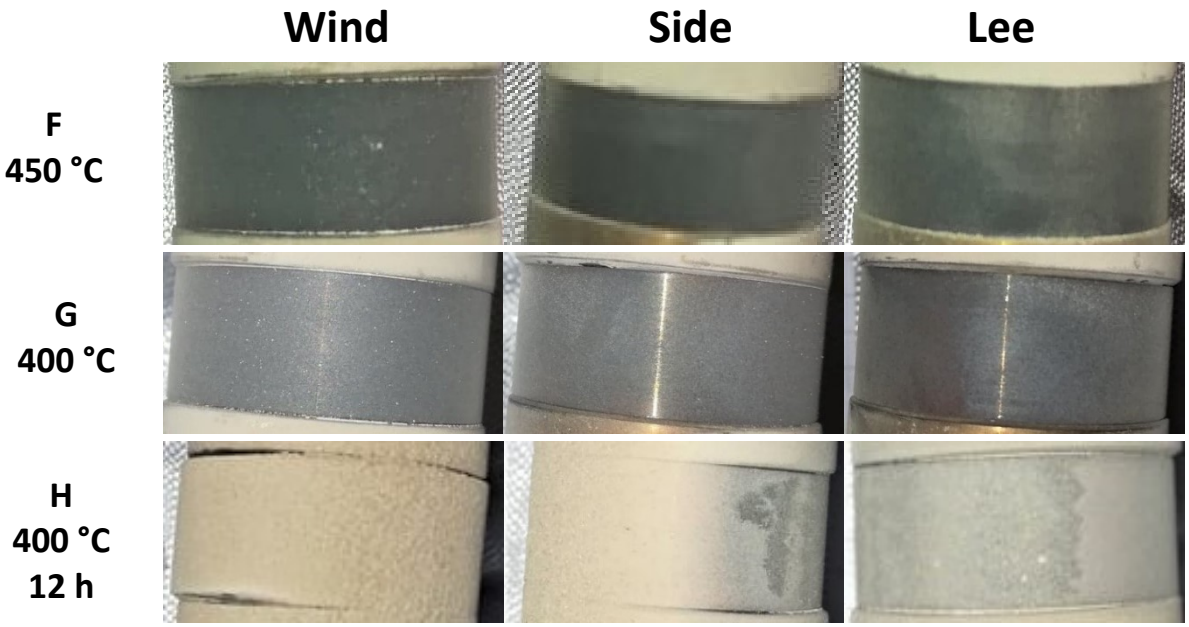

Figure 32: Probe samples from the measurements at the primary superheater.

Clear signs of corrosion were observed on the ring with the highest material temperature (Ring F). Spalling of the ring occurred, however, the spalling of the oxide scale was not as significant as in the case with Ring A. The corroded ring is shown in Figure 33. Interestingly, Ring F which was exposed at the primary superheater area appeared to be more corroded than the sample with the same material temperature at the secondary superheater. On the lee and side positions of the 12 h-sample, spalling was also observed.

Figure 33: A close-up of Ring F.

The calculated RBU values for each test run are presented below in Figure 34. The rates from the previous measurement point are also included for comparison. As the figure shows, the location of the measurement point has a small impact on the RBU. The deposition occurred at a somewhat higher rate just below the secondary superheater when compared to the rates at the primary superheater.

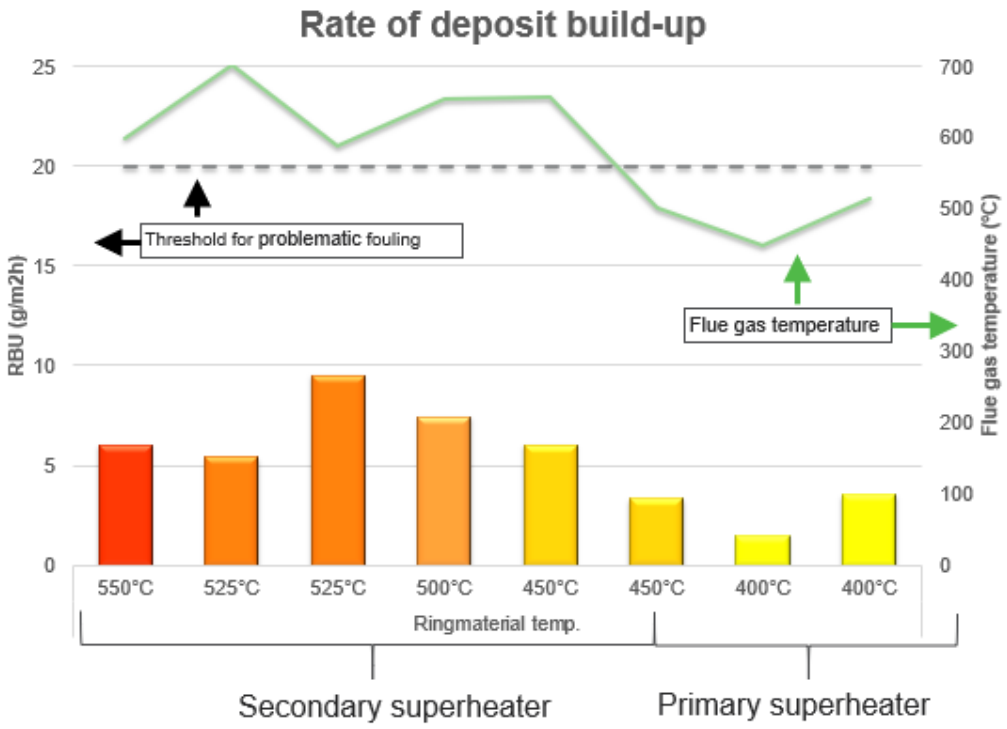

Figure 34: Calculated RBU for the samples collected before the secondary superheater and at the primary superheater.

In Figure 35, SEM-images of deposit samples collected during the measurements at the primary superheater are presented. Problems with obtaining enough sample for SEM-analysis were also experienced for the two shorter tests at this location. Results from the spot and area EDX-analyses as marked in Figure 35 are presented in Figure 36.

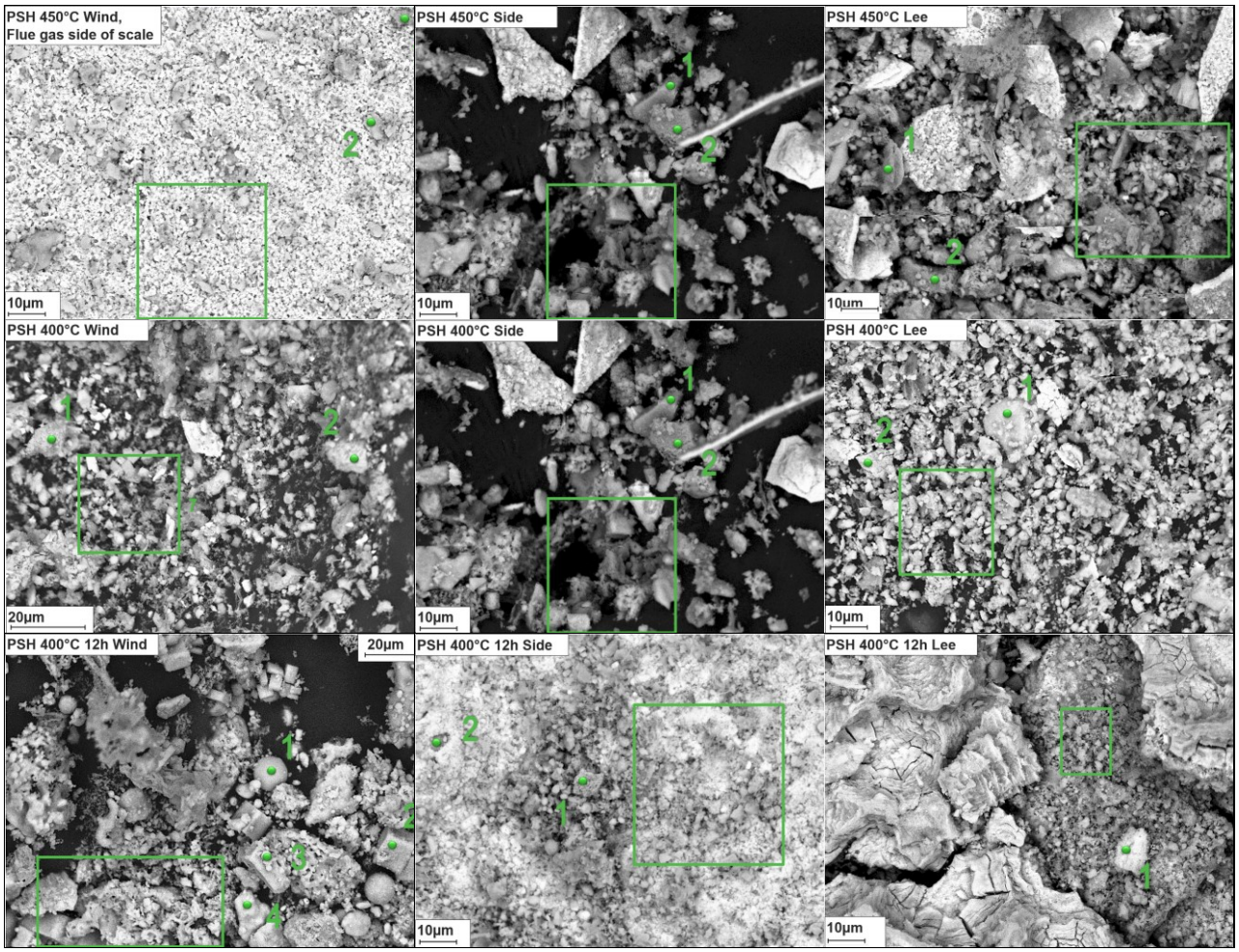

Figure 35: SEM-images of the samples collected by the primary superheater.

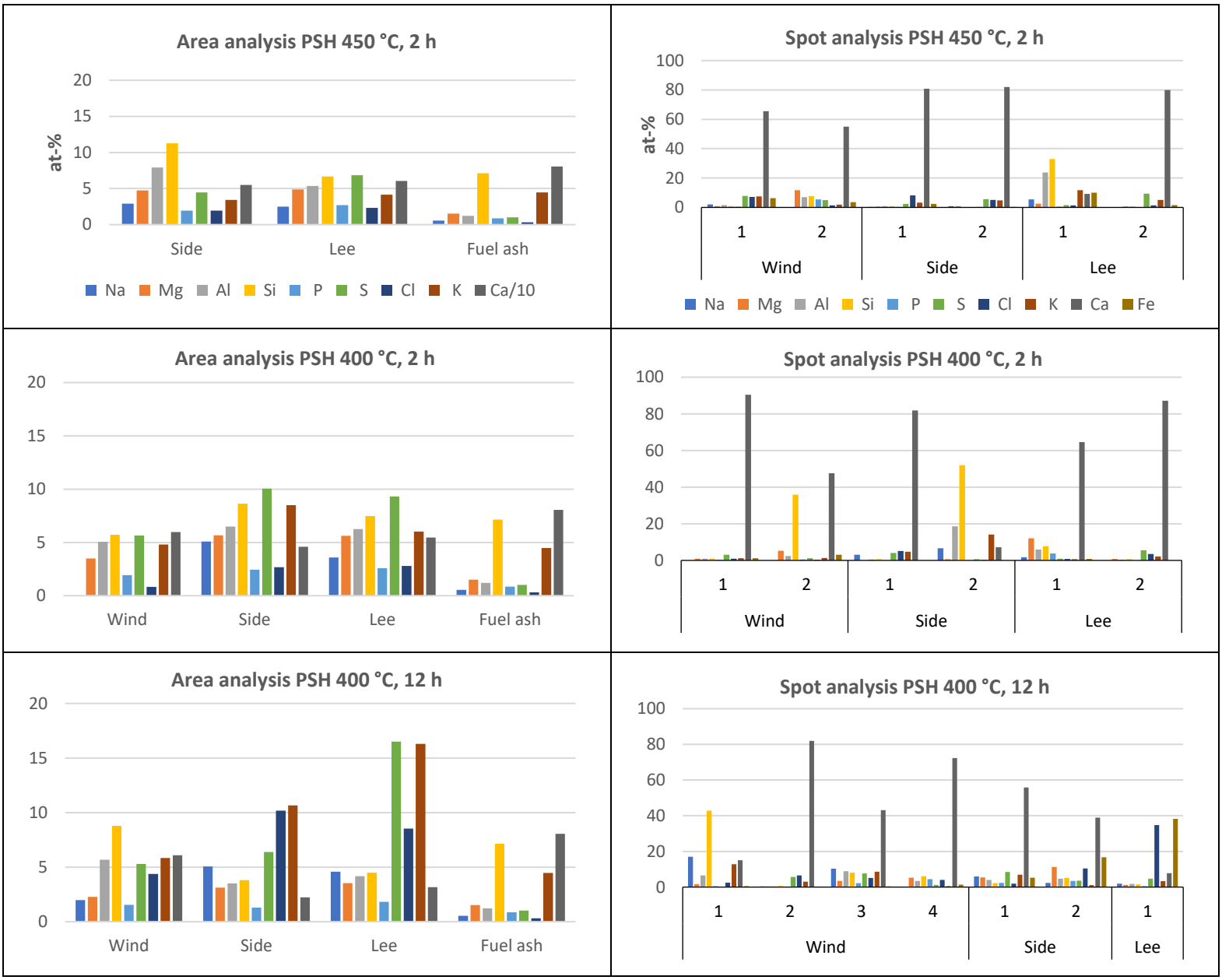

Figure 36: The elemental compositions for the area and spot analyses conducted on the samples collected at the primary superheater (PSH). The units of the y-axes and the color codes of the elements are the same for or all graphs.

The composition of the deposit collected in the primary superheater region is somewhat similar to those obtained just below the secondary superheater. The deposit consists mainly of calcium, while the other major elements present in significant shares are S, K, Mg, Na, Al, Si, Cl and P.

The elemental compositions of the deposits on the 2 h samples appear to be more consistent, regardless of position on the ring, while clear differences in the elemental compositions of the 12 h wind, side, and lee samples were detected. The deposit composition on the 12 h wind position was dominated by calcium, with lower amounts of sulfur, chlorine, and alkali. On the 12 h side and lee

positions the calcium content is still significant, but much lower compared to the wind position. In addition, sulfur, potassium, and chlorine were found in quite high shares at the same locations.

The size range of the particles present in Samples F and G is between 0,1-10 µm. In addition, in the H sample not only discrete coarse particles were detected, but also spherical and cubical particles. More agglomerated particles were detected in Sample H, as well, when compared to Sample F and Sample G. The amount of agglomeration detected in the long-term sample did not necessarily deviate when compared to the samples exposed just below the secondary superheater, however, the sizes of the agglomerated particles were more substantial in the former. The melting of the ash particles likely caused the spherical forms. These particles seem to be a mixture of alkali- and calcium-aluminosilicates. It has been reported that Ca-K-Al-Si systems can be formed when K-Ca sulfates react with aluminosilicates or when potassium sulfate react with calcium-aluminosilicate (Priyanto et al., 2016). The inclusion of potassium into Ca-Al-Si systems may drastically decrease the melting temperature of a particle, leading to increased deposit accumulation (Priyanto et al., 2016). The presence of calcium oxide in the deposits at the primary superheater and further along the flue gas channel may become more frequent due to a decreased effect of re-carbonization at lower flue gas temperatures. To better understand the form of calcium in the deposit, the O/Ca molar ratio was calculated for discrete calcium-based particles collected on the probe rings in the primary superheater region. The O/Ca molar ratios, along with the particles calcium shares, are presented in Figure 37.

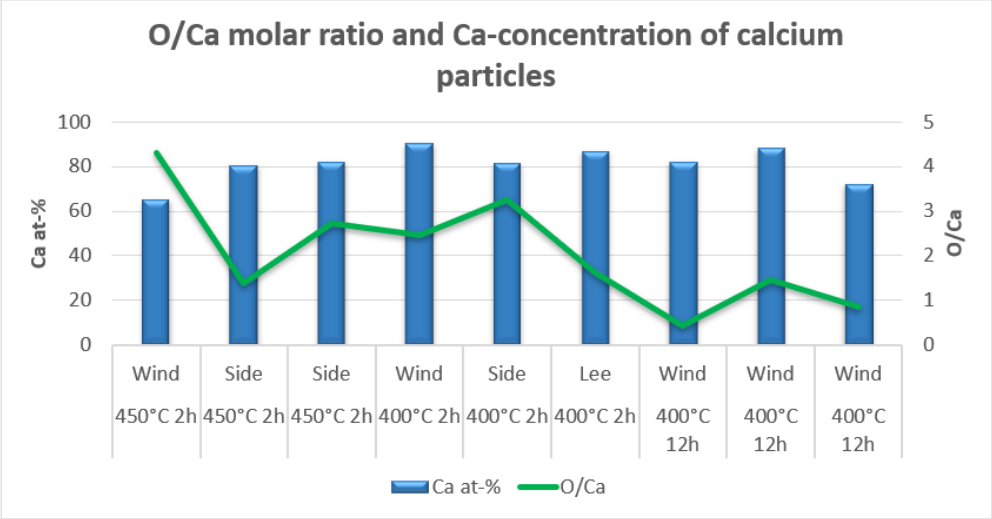

Figure 37: The O/Ca molar ratio and Ca-concentration of discrete calcium-based particles collected at the primary superheater.

As compared to the samples collected close to the secondary superheater (Figure 30), a clear shift towards lower O/Ca ratios has occurred at the primary superheater, especially in Sample H (12 h). The lower molar ratios of O/Ca of discrete calcium particles in combination with the lower flue gas temperatures suggests a more prominent presence of CaO at the primary superheater.

The chlorine enrichment factors in the deposits collected at the primary superheater are presented in Table 13. The chlorine enrichment coefficients are based on the chlorine content in the deposit and in the fuel.

Table 13: Chlorine enrichment coefficients in deposits collected at the primary superheater.

Sample	Position	Chlorine enrichment coefficient
F (450 °C)	Wind	Not enough sample for SEM
	Side	6.3
	Lee	7.5
G (400 °C)	Wind	2.6
	Side	8.7
	Lee	9.0
H (400 °C, 12 h)	Wind	14.1
	Side	32.9
	Lee	27.6

There was a significant difference in the accumulation of chlorine in the short term and long-term samples. On the short-term samples, the chlorine content was significantly lower than in the long-term samples, which is clearly pronounced in the side and lee analyses. For the short- term exposures the chlorine enrichment coefficients at these positions were between 6 and 9. However, a dramatical change in chlorine content could be observed for the long-term test with chlorine contents of 10 and 8.5 at-% in the side and lee samples. The chlorine enrichment factors in these samples were 33 and 27, respectively. In the wind sample of Sample H, the content of chlorine was much lower but still significant.

Based on the molar ratios between potassium and chlorine in Figure 36 and on detections from the spot analyses (Sample F wind and side spot 2; Sample G side spot 2, Sample H wind spot 2), chlorine seemed to be mainly present as alkali chlorides. In some of the spot analyses on the deposits collected in tests G and H, $CaCl_2$ may also have been present. Two probable observations of $CaCl_2$ were made on sample H (wind spots 2 & 4) and one on sample G (lee spot 2). Based on the locations of the analyses, the formation of $CaCl_2$ seems to occur on discrete particles of CaO or $CaCO_3$. Other

formation mechanisms are also possible, but more challenging to determine from SEM/EDX analysis.

According to the stability diagrams of calcium oxide, carbonate, hydroxide, and chlorine, the stability of $CaCl_2$ increases with decreasing temperature. Based on the chlorine levels in the fuel, the theoretical maximum concentration value of HCl in the flue gas was roughly estimated to be 16 ppm. However, as the chlorine levels are rather low in the fuel, it may fluctuate from time to time. At the stated level of HCl together with the moisture in the flue gas, $CaCl_2$ does not form from $CaCO_3$, only from CaO. The reason why $CaCl_2$ was not detected just below the secondary superheater, may thus be explained by the high amounts of $CaCO_3$ in the deposit. If the temperature of the deposit is the same as the probe material temperature, HCl concentrations around 500-750 ppm would be required for $CaCl_2$ to form from $CaCO_3$ at 450-550 °C.

Evidence of corrosion was also encountered in the deposit composition. Iron chloride, which is a known corrosion product, was detected in spot analyses in the side and lee samples on Ring H (side spot 2, lee spot 1). Some of the ash appears to have been molten since a melt has formed in the deposit in the vicinity of the iron chloride in the lee sample of Ring H. However, it is difficult to determine, whether the melting has occurred in flight or after deposition. The melted ash seemed to consist mostly of calcium, sulfur, potassium and chlorine. The lowest melting point of this particular system (Ca-S-K-Cl) was not determined. However, when considering the lowest melting temperature of the system K_2CO_3-KCl-K_2SO_4 (622 °C) and the fact that calcium is considered to raise the melting temperatures of particles in the flue gas, it seems likely that together, these elements are not able to form a melt at such a low temperature (400 °C) (Bergman and Sementsova, 1958). One explanation could, therefore, be that iron chloride has contributed to a lower melting temperature of the deposit.

The oxide scale on Ring F was loosely attached to the ring and carefully removed from the ring for further SEM/EDX analyses. SEM images of the flue gas side and of the tube side of the withered scale are shown below in Figure 38. The black line on the tube side of the scale is a crack between two flakes.

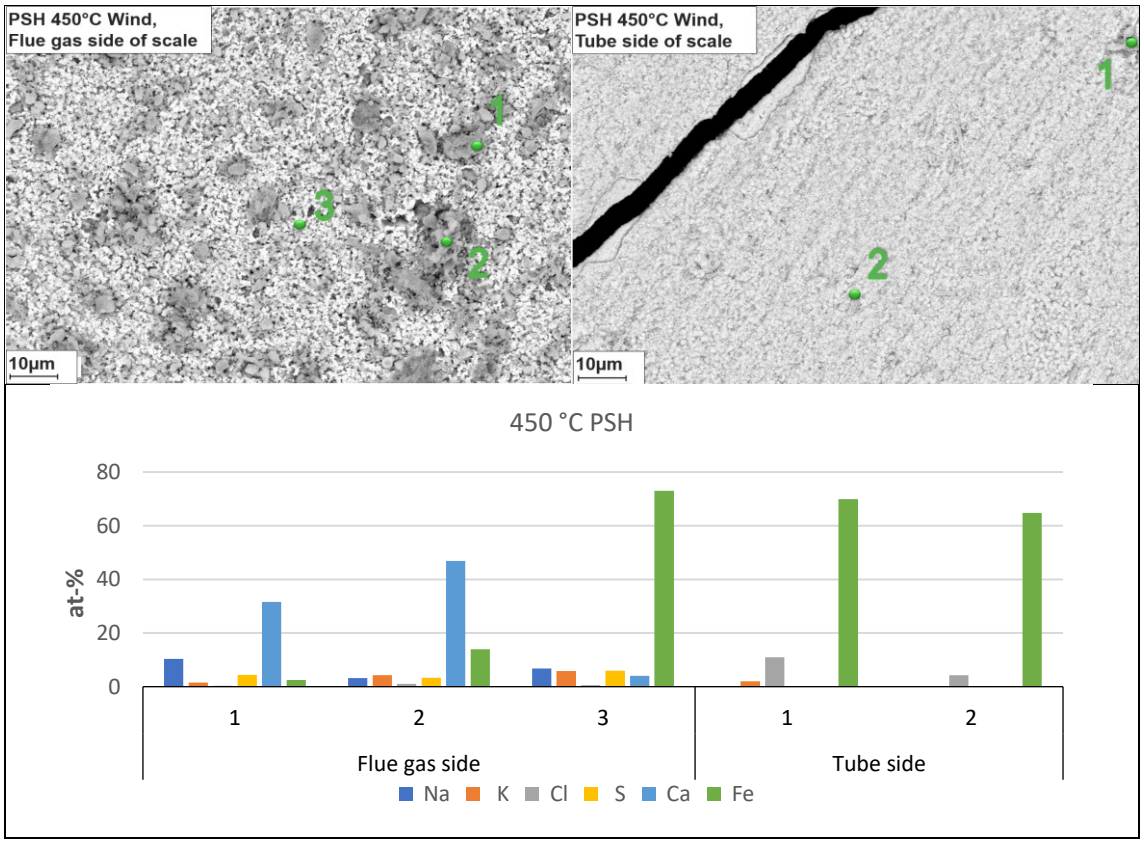

Figure 38: SEM/EDX results of the oxide scale collected from Ring F with a material temperature of 450 °C.

In Figure 38, the SEM-picture of the flue gas side of the scale shows that the scale is mostly covered in areas of a lighter nuance. Based on the chemical composition of Spot 3 on the flue gas side, the areas are rich in iron oxide, which is a corrosion product. Significant amounts of alkali have been detected in all spots on the flue gas side of the flake, which suggests that the corrosion that occurred on the rings exposed at the primary superheater is also alkali-induced. The alkali chlorides have likely been consumed here as well, as no chlorine was detected on the flue gas side of the flake. On the other hand, high amounts of chlorine were detected on the tube side of the flake. This chlorine is likely present as iron chloride, based on the low amounts of alkali present.

All evidence strongly suggests that corrosion is caused by alkali chlorides both at the secondary and primary superheater. However, some questions surrounding the behavior of $CaCl_2$ have not been answered, and thus, it remains unclear if $CaCl_2$ is corrosive at these temperatures. However, the evidence indicates that $CaCl_2$ has no significant influence on corrosion in this case. Calcium chloride seems to be present only locally, and the detected amounts are much lower compared to the content of alkali chlorides in the deposit. Therefore, any impact on corrosion that $CaCl_2$ may have in this area is overshadowed by alkali chloride induced corrosion.

TGA-analysis of Sample H was conducted to gain further information about the types of compounds present in the deposit. As the deposit was expected to mainly consist of calcium-based compounds, $CaCO_3$ and $Ca(OH)_2$ was used as reference samples during the analysis. When $CaCO_3$ and $Ca(OH)_2$ undergo heat treatment, $CaCO_3$ will calcine, while $Ca(OH)_2$ will release water at around 400 °C. Both $CaCO_3$ and $Ca(OH)_2$ will form CaO in the process. The sample weight loss is therefore compared to the weight loss of the references, so that the decomposition of both $CaCO_3$ and $Ca(OH)_2$, may be easier detected from the analysis results. In Figure 39a the temperature difference between the deposit sample and a reference (empty container) is displayed. In Figure 39b, the weight loss of the sample and the reference samples are displayed.

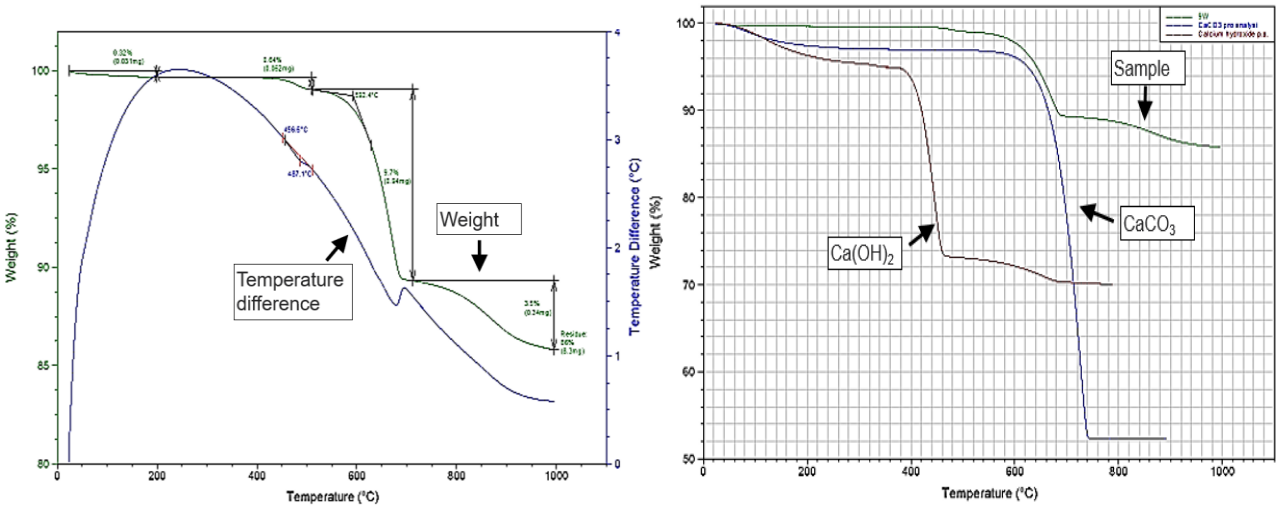

Figure 39: Results from the TGA-analysis of the 12 h deposit sample from the primary superheater.

The deposit sample consisted mainly of calcium compounds (at-% 61), with small shares of alkali, sulfur, and chlorine. A somewhat higher share of aluminum was also detected. Due to the similarities between the sample and calcium carbonate graphs, the loss of weight after the sample reaches 600 °C represents the decarbonization of calcium. The total weight loss amounts to 10 %, meaning that the fraction of $CaCO_3$ in the sample amounts to 23 % if assumed that the whole weight loss is due to carbonates present as $CaCO_3$.

It is difficult to determine what the small weight loss below 600 °C represents, as this could be due to several reasons. Both references express the same behavior. In their cases, the loss of weight represents the evaporation of water. The minor loss of weight occurring after decarbonization is also challenging to determine. One possible explanation could be the evaporation of alkali chlorides, which have occurred above a temperature of 700 °C in thermogravimetric experiments (Broström et al., 2011).

Finally, an XRD-analysis was conducted on the 400 °C wind sample. The compounds detected, and the signal intensities are presented in Table 14. Based on the signal intensities the compounds are categorized into major (***, >15 wt.-%), minor (**, <15 wt.-%), or trace amounts (*, <5 wt.-%).

Table 14: Results from XRD-analysis on Sample H.

Phase	**PSH 400 °C Wind**
CaO (lime)	*
$Ca(OH)_2$ (portlandite)	**
$CaCO_3$ (calcite)	***
$K_2Ca(CO_3)_2$ (bütschliite)	
KCl (sylvite)	**
$K_3Na(SO_4)_2$ (aphtitalite)	*
$CaSO_4$ (anhydrite)	**
MgO (periclase)	*
SiO_2 (quartz)	
Ca_2SiO_4 (larnite)	
$Ca_3MgSi_2O_8$ (merwinite)	
$Ca_2Al_2SiO_7$ (gehlenite)	***
$Ca_3Al_2O_6$	*

The XRD analysis provides valuable support as it confirms some of the hypotheses which have been stated in this work. Previously mentioned evidence has strongly suggested that the corrosion is caused by alkali chlorides and the detection of KCl in the deposit at the primary superheater supports this assumption. Traces of $K_3Na(SO_4)_2$, combined with the detection of minor amounts of $CaSO_4$, confirms indeed that calcium captures sulfur in the flue gas and thus contributes indirectly to corrosion by decreasing the sulfation of alkali chlorides. No $CaCl_2$ was detected in the sample, although the SEM/EDX results suggested it was present at least in minor amounts. The absence of $CaCl_2$ in the XRD analysis will be further discussed in the part of this work that treats the results from the cold-end section of the boiler.

The fuel analysis indicated the presence of calcium aluminosilicates in the sludge, which was confirmed by the strong signals of gehlenite ($Ca_2Al_2SiO_7$) in the XRD-analyses. Alkali was not found in any of the aluminosilicate systems detected in the XRD-analysis, and therefore it is concluded that calcium aluminosilicates do not reduce corrosion by capturing alkali.

After the deposits on the probe rings had been analyzed, the rings were washed in citric acid. The purpose of the washing was to dissolve all corrosion products in the acidic

solution. An ultrasound bath was used for the washing. In Figure 40a, the washed rings can be observed. The corrosion rates of the deposit rings were calculated after weighing the newly rinsed rings, and the results are presented in Figure 40b.

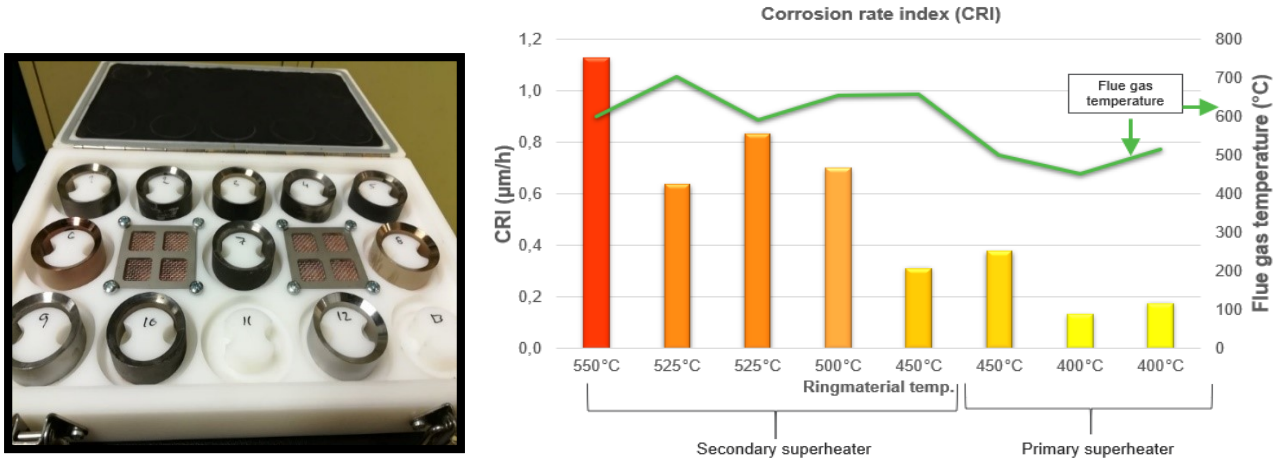

Figure 40: a) A photograph of the rings washed with citric acid, b) Calculated CRI for the samples collected before the sec. superheater and at the prim. superheater.

Judging by the graph in Figure 40, a clear correlation between the corrosion rate and the material temperature can be observed. At temperatures over and at 500 °C, increased corrosion rates can be observed. Below 500 °C, the corrosion is less aggressive. A more alloyed superheater material is used in the secondary superheater region of the boiler, and therefore the real corrosion rates are likely much lower. However, based on the corrosion rates available, one can conclude that X10CrMoVNb9-1 is not fit as a secondary superheater material with the fuel mixture used, due to the high corrosion rates on the sample rings. Sulfur addition would likely be recommended.

6.3 Low-temperature measurements

The results from the measurements at the air preheater (APH) are presented in this section. The samples, along with the type of ring material and material temperature, are listed in Table 15.

Table 15: The sample ID:s for the test run at the air preheater.

Sample	Material temperature, °C	Material
I	120	16Mo3
J	120	304L
K	100	16Mo3
L	100	304L
M	80	16Mo3
N	80	304L

The flue gas pressure at the air preheaters was below ambient, which made it challenging to obtain a sample. In Figure 41, the collected deposit on the probe tip can be observed. Most of the deposit has been removed by the draft in the opening while taking the photo (during the measurement the opening was covered). Furthermore, during probe removal, the under-pressure in this section of the boiler led to that most of the deposit was removed from the probe. Accordingly, the RBU values were not determined for these tests.

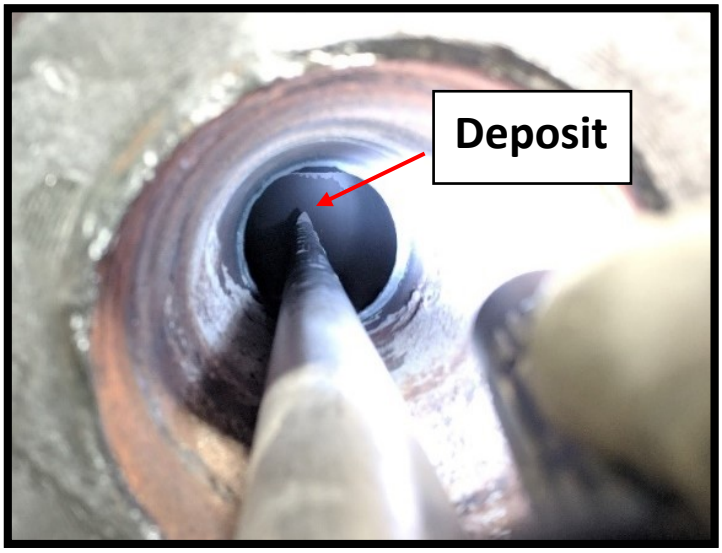

Figure 41: Image of the deposit collected on the deposit probe at the air preheater.

In Figure 42a and Figure 42b photographs of the probe before and after exposure at the air preheater are presented. The exposure time of the test was approximately 48 h. Apparent signs of corrosion of a low-alloy ferritic steel (16Mo3) were visually observed at a material temperature of 80 °C. The corrosion was likely caused by hygroscopic salts since the probe was covered with a thick deposit. No corrosion of the rings was observed at material temperatures between 100 and 120 °C.

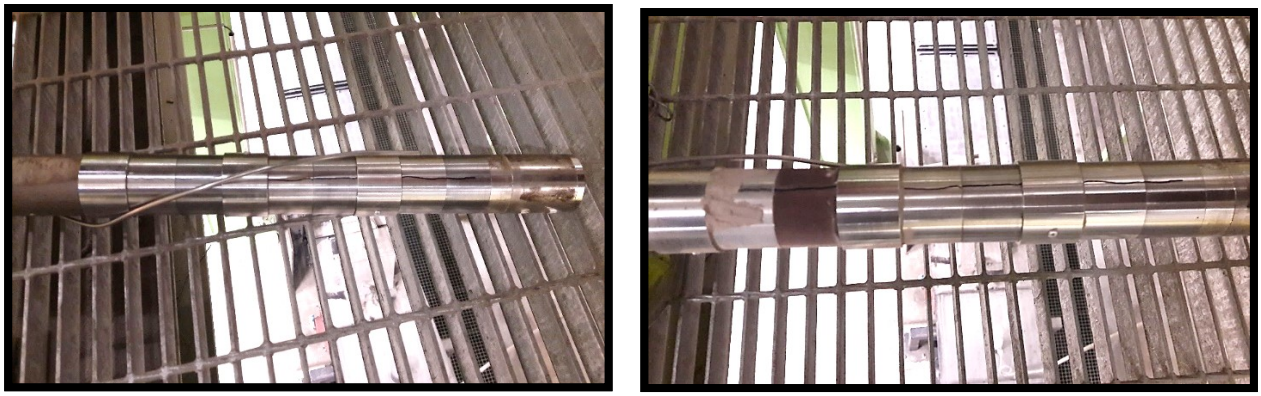

Figure 42: The deposit probe before and after exposure to the flue gas environment at the air preheater.

Short-term corrosion probe tests, with rings of carbon steel (P265GH), were also conducted to determine the corrosion rate in these conditions. The material temperatures in these tests were 100, 90, and 80 °C. Mild corrosion could be observed on the surface of the probe ring at 80 °C, after being exposed for 1.5 h (Figure 43). The average flue gas moisture was also at its highest during this measurement (27.9 %), which may have contributed to the initiation of corrosion. No corrosion was observed at the higher temperatures, 90 and 100 °C. Thus, the corrosion threshold for the carbon steel in the test conditions was somewhere between 80 and 90 °C.

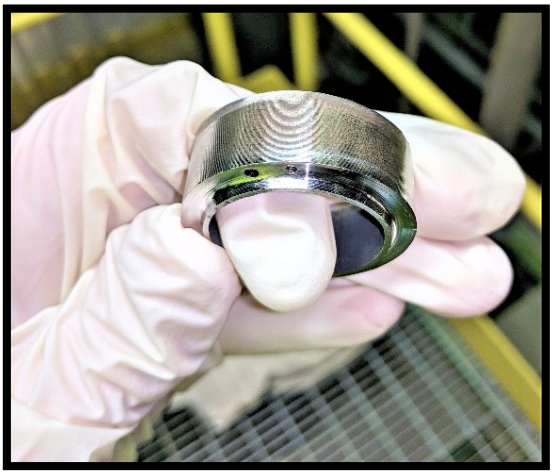

Figure 43: The corrosion probe ring after short-term exposure to the air preheater environment.

In Figure 44, SEM-images of deposit samples collected at the air preheater are presented. In all SEM-images, the locations of both the area and spot analyses are marked. Elemental oxygen was excluded from the EDX results that are presented in Figure 45.

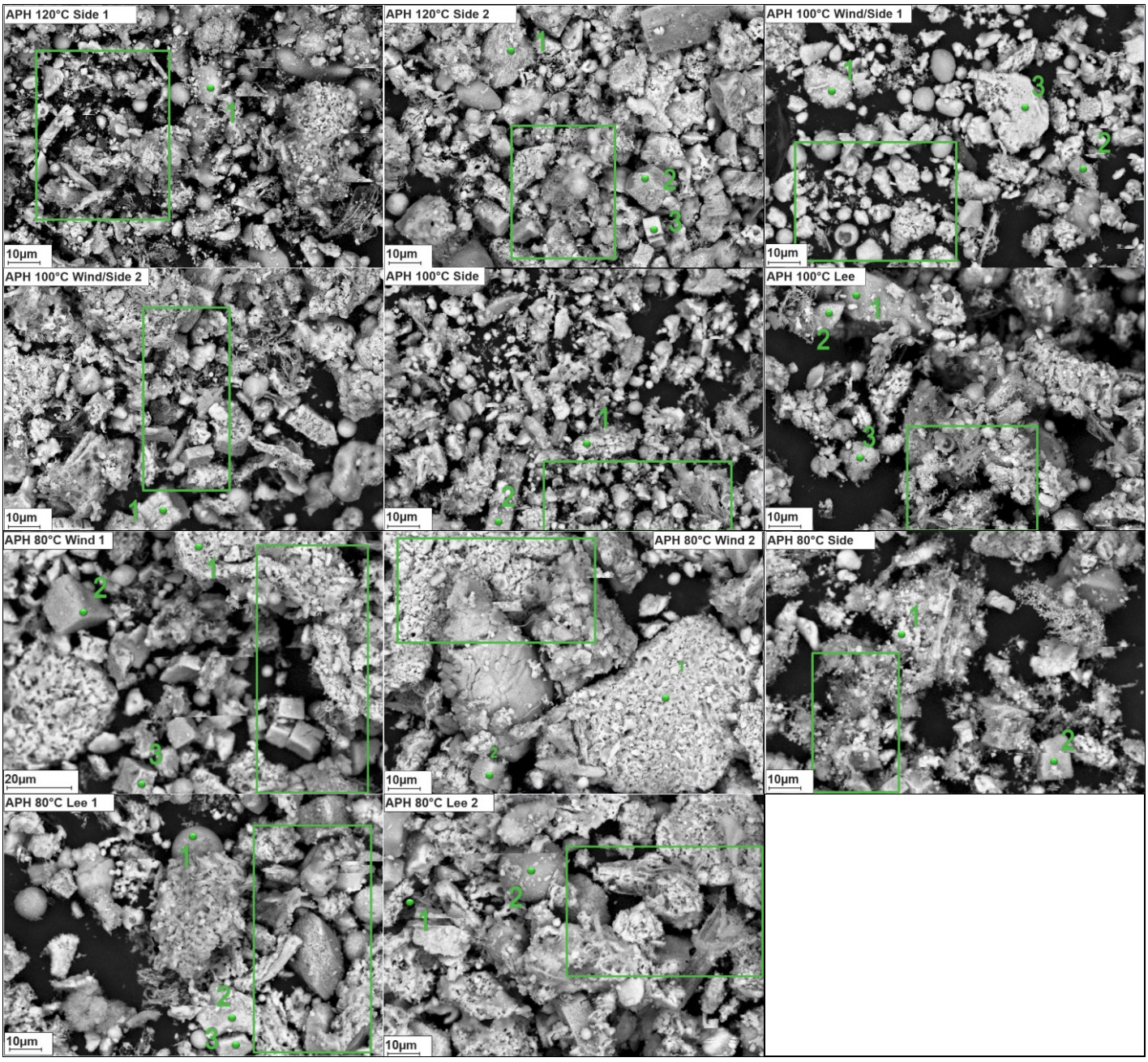

Figure 44: SEM-images of the samples collected at the air preheater.

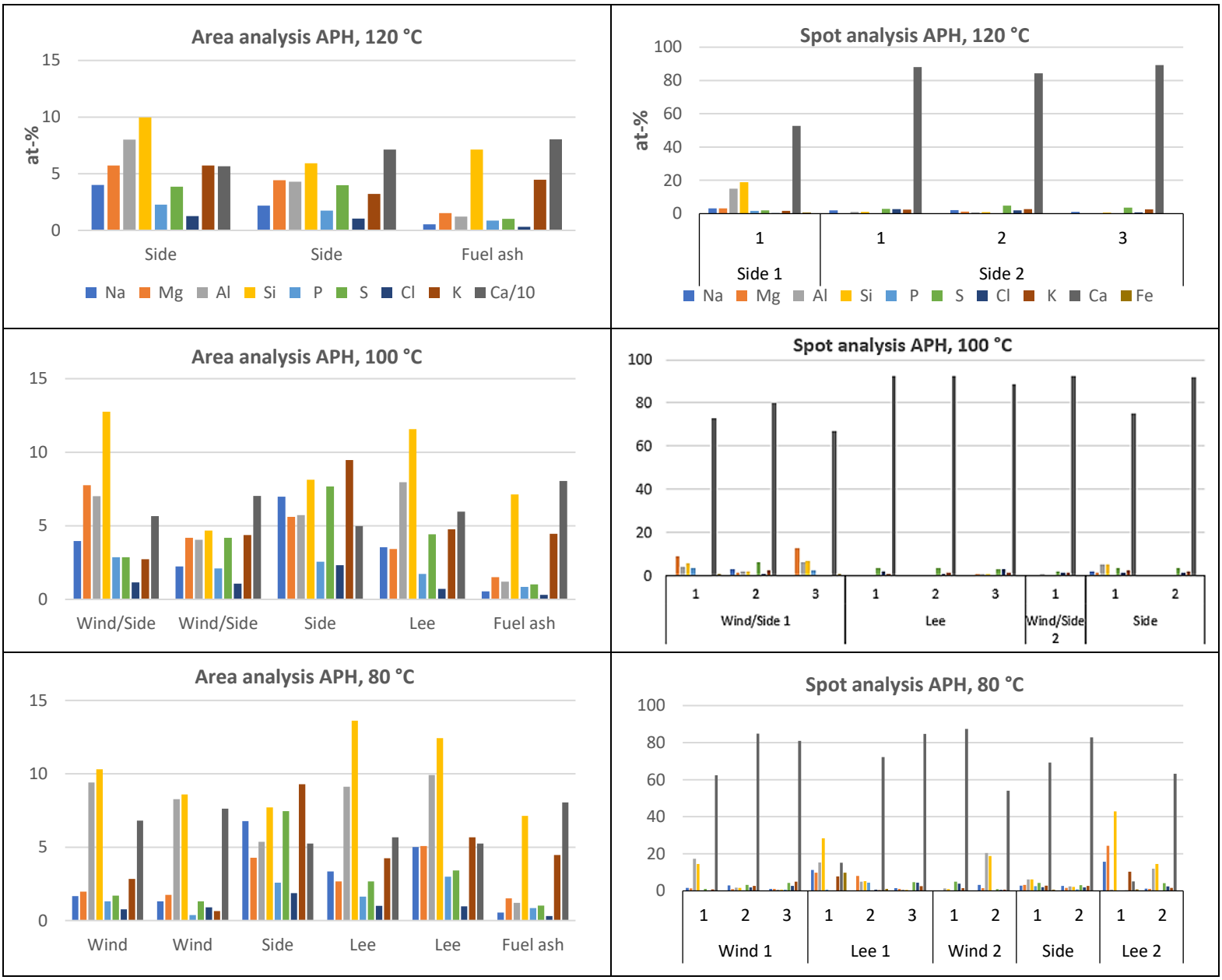

Figure 45: The elemental composition for the area and spot analyses of samples collected at the air preheater. The units of the y-axes and the color codes of the elements are the same for or all graphs.

Like for the higher temperature probe rings, the deposits on the rings exposed in the cold-end contained large amounts of calcium. However, in the cold-end deposits, the shares were even higher, showing an average elemental share of 60 at-%. The high amounts of calcium were observed in all analyses independent on location (wind, side, or lee).

A similar trend of sulfur and potassium accumulation on the side of the rings could also be observed. On the side deposits on rings L and N, the potassium and sulfur contents were somewhat elevated compared to the other samples. Although the average share of silicon in the deposits was still somewhat underrepresented compared to fuel ash, the accumulation of silicon together with aluminum was much higher in the cold-end as compared to the results from the other measurement

locations. The shares are also significantly higher when compared to the sample exposed for 12 h at the primary superheater. In some area analyses, the contents of sodium and magnesium have been made (Sample I side, Sample K wind/side, Sample L side, Sample N side & lee). It is noteworthy that the K/Na ratio is clearly lower in the rings exposed in the cold-end, indicating a higher accumulation of sodium.

There is a wider particle size range in comparison to the samples from the high-temperature measurements. Especially larger agglomerated particles have been detected, which can reach sizes of up to 6 µm. Spot analyses show that some of the larger agglomerated particles are systems of Ca-Al-SI (Sample M wind spot 1, Sample N wind spot 1). The trigonal crystal structure of calcium carbonate was not detected. However, the O/Ca ratio calculated from the EDX analyses indicate that both calcium carbonate and oxide are present as fragmented particles. The presence of cubical particles was detected in somewhat higher contents compared to the higher temperature samples. The frequency of detections increased at a material temperature of 80 °C. No hexagonal crystal structures were detected, although from some angels the calcium crystal structures may look similar. Especially the cubical and hexagonal particles may be mixed. Spot analyses show that the compositions of particles of spherical forms are systems of calcium-silicates and calcium-aluminosilicates, containing varying amounts of magnesium and alkali (Sample M lee spot 1, Sample N lee spot 1).

In comparison to the levels from the higher temperature deposits, the amount of chlorine at the air preheater, was much lower. However, the amounts are still significant as compared to the chlorine content in the fuel. The highest amounts were found on the side positions of Samples L and N. The corresponding chlorine enrichment coefficients were determined to be 7.5 and 6.0, respectively. The amounts of chlorine on these samples show that there are prerequisites for corrosion caused by chlorine-based hygroscopic salts at material temperatures 80 °C and 100 °C in the air preheater region. All chlorine enrichment coefficients calculated for the deposits collected in the air preheater region are presented in Table 16.

Table 16: Chlorine enrichment coefficients in the deposits collected at the air preheater.

Sample	Position	Chlorine enrichment coefficient
I (120 °C)	Side	4.1
J (120 °C)	Side	3.4
K (100 °C)	Wind/Side	3.8
L (100 °C)	Wind/Side	3.5
L (100 °C)	Side	7.5
K (100 °C)	Lee	2.3
M (80 °C)	Wind	2.5
N (80 °C)	Wind	2.9
N (80 °C)	Side	6.0
M (80 °C)	Lee	3.3
N (80 °C)	Lee	3.2

It was more challenging to determine in what form chlorine was present as in the deposit collected at the air preheater. Based on the observation of alkali chlorides in the superheater region, the molar ratios of alkali and chlorine in the deposit, and the fact that alkali chlorides are stable at lower temperatures suggest that alkali chlorides are present, at least to some extent in the deposit. However, due to the low amounts of potassium and chlorine detected, this could not be confirmed. Based on the stability diagram of $Ca(OH)_2$ vs $CaCl_2$ (Figure 17), it was concluded that $CaCl_2$ can be formed if the flue gas contains HCl. While the presence of $CaCl_2$ could not be determined from the area analyses either, it was possibly identified in some of the spot analyses (Sample K wind spots 1 & 2 and lee spots 1-3, Sample M lee spots 2 & 3, and Sample N wind spot 2). In these locations, chlorine did not exist only as alkali or iron chlorides as there were not enough alkali and iron detected. Therefore, the presence of $CaCl_2$ is a possibility. Chlorine was detected on two discrete $CaCO_3$ particles and on one discrete CaO cubical particle. The observations indicate that if $CaCl_2$ was present, it might have formed either from CaO and/or from $CaCO_3$ according to Reactions 9 and 10.

In Figure 17, the stabilities of CaO, $CaCO_3$, and $CaCl_2$ are illustrated. Based on the material temperatures (80-100-120 °C) at the air preheater during the measurements, $CaCl_2$ was more likely to be formed from $Ca(OH)_2$ or CaO according to the stability diagrams. According to thermodynamics at this flue gas temperature (150 °C) and moisture content (25 %), $CaCl_2$ may form from $CaCO_3$ if the flue gas concentration of HCl is above 50 ppm. Calcium hydroxide is not stable under similar conditions and can form $CaCl_2$ even at low flue gas concentrations of HCl.

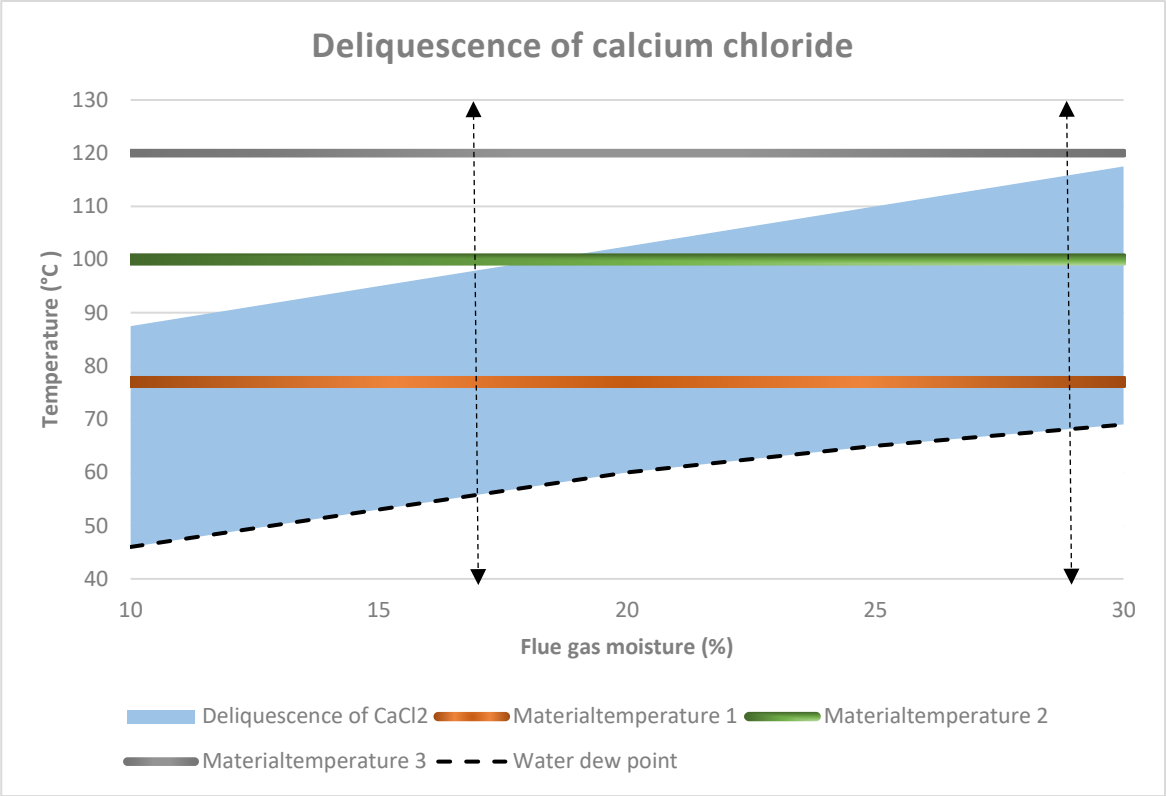

Figure 46: Conditions at which $CaCl_2$ may cause corrosion due to the formation of wet deposits. Blue = corrosion risk area. Adapted from Vainio et al., 2016.

In Figure 46, the deliquescence behavior of $CaCl_2$ is visualized in a temperature versus moisture chart. The blue area marks under which conditions, $CaCl_2$ is present as wet deposits and can cause corrosion. The dashed line marks the reaching of the water dew point. The horizontal lines represent the average material temperatures of the probe rings during the measurements. Based on the flue gas moisture during the measurements, corrosion caused by $CaCl_2$ would have been possible on the probe rings with a material temperature of 100 °C and 80 °C. However, corrosion was observed only for the latter. If the cause was $CaCl_2$, it should have absorbed water also at 100 °C. However, the corrosivity of a deposit containing only some $CaCl_2$ is not well understood. Furthermore, the deposit is a mixture of several different compounds and the hygroscopicity and corrosivity may not fully follow the behavior of $CaCl_2$.

A closer examination of the corroded ring reveals that the corrosion was widely spread over the ring. Typically, the corrosion of hygroscopic salts is more intense on the wind and side positions in the early stages. This was the case in the short-term experiment at 80 °C (Figure 47). Sadly, no photo was taken of the sample from the lee position, only from the wind and side positions. In the figure, a small stripe was observed on the ring, which could be a border between two corroded areas.

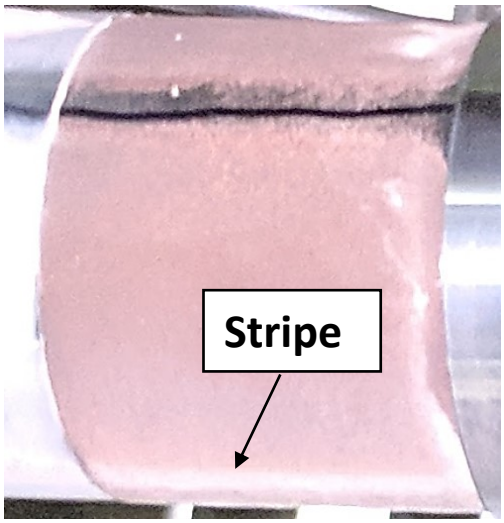

Figure 47: A close-up of the corroded ring.

A cross-section cut of the corroded probe ring was analyzed using SEM/EDX, to provide further information about the corrosion mechanism. A single observation of both iron and chlorine was made on the ring 135° from the wind position. Iron chloride is also hygroscopic but cannot be the only explanation to the occurred corrosion as it is a product of corrosion. Iron chloride could, therefore, intensify the corrosion, but not be the first hygroscopic salt to initiate it. As no other clear observations of hygroscopic salts were made, the cause of corrosion could not be determined. The composition of the ring surface consisted almost entirely of iron oxide, the other elements present being Ca, K, Cl, S, Na, Mg, Al, and Si. In relation to the other elements, calcium, potassium, and chlorine seem to be present in higher amounts. Therefore, corrosion caused by $CaCl_2$ remains possible. Corrosion caused by other hygroscopic salts is possible, as well as a combination of salts since they are often more hygroscopic than individual salts.

Finally, XRD-analysis was conducted on the deposit collected from the wind position on Sample N. The compounds detected, and the intensities of the signals are presented in Table 17. Based on the signal intensity each compound is categorized into major (***, >15 wt.-%), minor (**, <15 wt.-%), or trace amounts (*, <5 wt.-%).

Table 17: Results from the XRD-analysis conducted on the deposit collected on the wind position of Sample N.

Phase	**APH 80 °C Wind**
CaO (lime)	**
$Ca(OH)_2$ (portlandite)	**
$CaCO_3$ (calcite)	***
$K_2Ca(CO_3)_2$ (bütschliite)	*
$K_3Na(SO_4)_2$ (aphtitalite)	*
MgO (periclase)	*
SiO_2 (quartz)	*
Ca_2SiO_4 (larnite)	***
$Ca_3MgSi_2O_8$ (merwinite)	**
$Ca_2Al_2SiO_7$ (gehlenite)	**
$Ca_3Al_2O_6$	**

The XRD results were somewhat surprising as no chlorine-based compound whatsoever were detected in the sample, even though detections of chlorine were made in the SEM-analysis, although in somewhat low contents. Now, as the XRD-analysis was not able to clarify the occurred corrosion and the possible presence of $CaCl_2$, several scenarios remain possible. Each scenario and the probability of it will be discussed henceforth.

Although calcium chloride was not detected in the XRD-analysis, several pieces of evidence point to the presence of $CaCl_2$. First of all, it has previously been shown that the formation of $CaCl_2$ is thermodynamically possible both in the primary superheater region and in the cold-end. The formation of $CaCl_2$ from $Ca(OH)_2$ in the air preheater region is the more probable route in this case. Secondly, the surplus of chlorine compared to the amounts of alkali and iron on quite pure calcium particles suggests the possibility that $CaCl_2$ was present. However, the compound was not detected in the XRD analysis. The following statements could explain the lack of $CaCl_2$ in the sample. First, the amount of $CaCl_2$ may have been too small for detection. The lower limit of detection often lies around 0.5 wt-% but may vary depending on the rest of the sample. The chlorine content of the samples was 0.4 wt% as determined by SEM-EDX, and if assumed that all chlorine is present as $CaCl_2$, its share would be close to 0.7 wt-%. Based on these statements, it is certainly possible that the amounts of $CaCl_2$ may have been too low for detection. Another possible explanation is that $CaCl_2$ has reacted with moisture in the surrounding air, either during storage or during analysis. In that case $CaCl_2$ would be in a non-crystalline state and therefore not detectable by XRD-analysis.

Although corrosion was not observed at 100 °C, where $CaCl_2$ has been established as corrosive, it is not known how the bulk of the deposit affects the corrosiveness of $CaCl_2$. It may be that the bulk of the deposit has absorbed the liquid after $CaCl_2$ has deliquesced. However, if $CaCl_2$ was not the cause of corrosion, other hygroscopic salts are the most likely suspects. Corrosion could not have been caused by H_2SO_4 or HCl either, as there was no SO_2 in the flue gas, and the dewpoint of HCl is close to the water dewpoint. The lack of corrosion at 100 °C and lack of detections of chlorine-based compounds in the XRD-analysis are, on the other hand, arguments in favor of corrosion caused by another hygroscopic salt than $CaCl_2$. Also, the corrosion seemed to be widely spread on the probe ring, while the detection of $CaCl_2$ in the SEM-analysis indicated that $CaCl_2$ is present only in smaller amounts in the deposit.

In addition to $CaCl_2$, the following hygroscopic salts can be considered candidates for the chlorine-induced corrosion on the deposit probe at the air preheater; KCl, NaCl, $MgCl_2$, NH_4Cl. Double salts of these compounds may also cause corrosion, but limited research of them has been conducted, and therefore, they are more challenging to discuss. Of the hygroscopic salts mentioned ammonium chloride can be considered the most likely to cause corrosion, as reduction of nitrogen with ammonia is conducted in the boiler after the economizers. Ammonium chloride may then form at low flue gas temperatures when the partial pressures of ammonia and hydrochloric acid are sufficiently high. Ammonium chloride is a hygroscopic salt, which may cause corrosion in the economizer and air preheater area. The DRH value of ammonium chloride is 77 % at 25°C, which is in a similar range with NaCl (Wexler et al., 1991). Ammonium chloride is difficult to detect, which may explain why chlorine was detected in the SEM-analysis, but no chlorine compounds were present in the XRD sample. In Figure 48, the thermodynamic stability of NH_4Cl is displayed in a NH_3-concentration versus temperature diagram with gaseous HCl as a parameter.

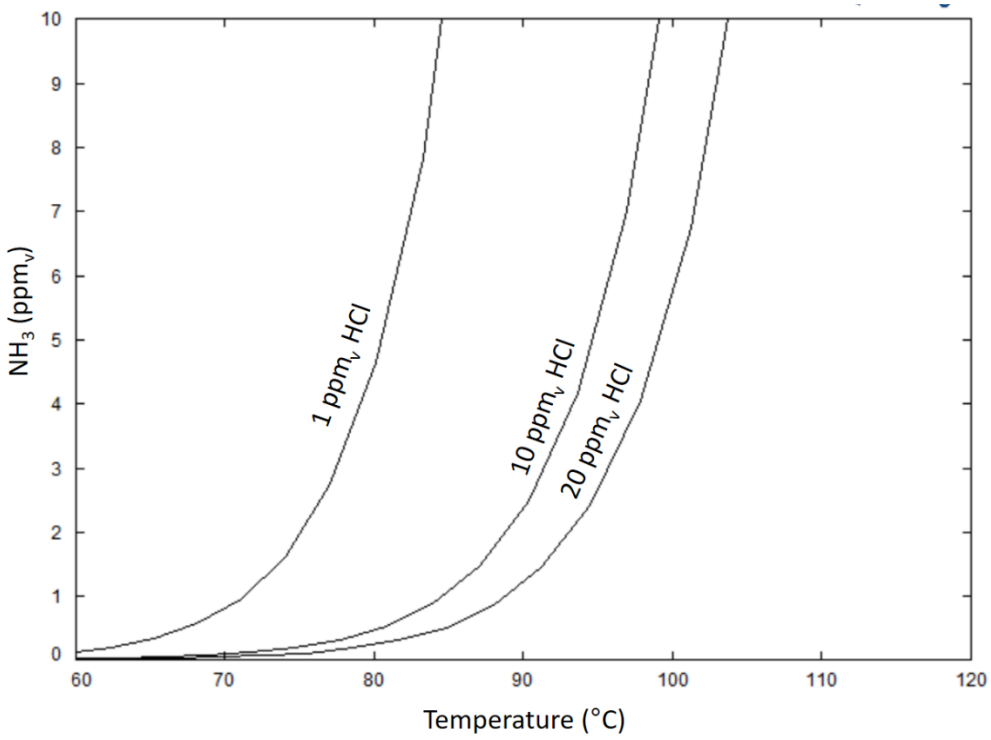

Figure 48: The thermodynamic stability of ammonium chloride calculated with FactSage 7.3.

The average concentration of NH_3 measured in the flue gas during the tests was 5.5 ppm, although significant variation could be observed during some periods. There was no relevant data of HCl concentration available, as HCl was only measured in the chimney. However, the theoretical maximum flue gas concentration of HCl was roughly estimated (based on fuel data) to be 16 ppm. The real chlorine concentration at the measurement point is likely lower than that since the chlorine concentration in the cold-end of the boiler is typically lower when compared to levels in the superheater region. From Figure 48, it is apparent that NH_4Cl can form on a deposit ring at the lowest material temperature used in this work (80 °C). Based on the estimated concentration of HCl, the required HCl-level is likely too high for NH_4Cl formation at 100 °C. This could explain why corrosion was observed at 80 °C but not at 100 °C. If NH_4Cl would form at 100 °C, then $CaCl_2$ would likely be present as well, because the HCl-concentration is so high.

The following hygroscopic salts are less likely to have been the cause of corrosion in this case when compared to $CaCl_2$ and NH_4Cl, but since the research in hygroscopic salts is at such an early stage, it is important to include scenarios that cannot be ruled out. Corrosion caused by hygroscopic alkali chlorides, and especially KCl, in this case, is primarily supported by their availability. The high amounts of KCl at higher temperatures suggests that it is at least to some extent present in the cold-end as well. However, they are much less hygroscopic compared to $CaCl_2$. The solubility of KCl and

NaCl in water is 35.5g and 36g, respectively and their DRH:s are 85 and 75 % at 25 °C (Weast, 1995; Greenspan 1977; Li, 2014). Although their DRH has not been defined at higher temperatures, it is clear that KCl and NaCl deliquesce at much lower temperatures compared to $CaCl_2$ and is, therefore, less likely to have initiated the formation of wet deposits on the probe rings.

The corrosiveness of alkali chlorides in the cold-end may be affected by the presence of other hygroscopic salts. Formation of wet deposits in the proximity of alkali chlorides with higher DRH may raise their solubility and induce corrosion by increasing the presence of chloride ions in the deposit. The sample also contained minor amounts of the compound $K_2Ca(CO_3)_2$. The made detections of this particular double salt in the cold-end and not in the primary superheater region could point to the crystallization from a water phase, as a formation mechanism. If true, then calcium, potassium, and carbonate ions have all been present in the wet deposit. While $CaCO_3$ is poorly soluble in water, K_2CO_3 is easily soluble and a hygroscopic salt with DRH quite close to $CaCl_2$ (Greenspan, 1977). Since the corrosion mechanism appears to be chlorine-based, it is likely not initiated by K_2CO_3. However, the presence of K_2CO_3 in combination with KCl may create a corrosive environment. On a further note, $CaCl_2$ requires very dry conditions to crystallize as it shows hysteresis effect upon drying. That is, a much dryer condition is needed for $CaCl_2$ to recrystallize than the DRH (Vainio et al., 2019). It may, therefore, be possible that $CaCl_2$ initiates the formation of wet deposit but crystallizes as something else from the solution when the probe is removed from the boiler, for example, as $CaCO_3$, which is poorly soluble in water (Onasch et al., 2000).

Traces of the double salt $K_3Na(SO_4)_2$ was found in the deposit at the air preheater, and also in the deposit collected at the primary superheater. That the detections were made in both XRD-samples, indicate that the compound was formed in the flue gas. The salt is however not hygroscopic as sulfates are poorly soluble in water (Greenspan, 1977; Tang and Munkelwitz, 1993). There are, however, other hygroscopic salts that may form at high temperatures in the flue gas. Figure 49, shows that the double salt of calcium and potassium chloride is thermodynamically stable at higher temperatures. Chlorocalcite ($KCaCl_3$) is known to be hygroscopic and may, therefore, cause corrosion (Retschitzegger et al., 2015). The hygroscopic properties of $KCaCl_3$ have been estimated by experimental testing of its solubility in water at 25 °C. Its solubility in water was determined to be 40 g/100 g H_2O, which is far lower than the solubility of $CaCl_2$ (81,3), however, higher than the solubility of KCl and NaCl. Therefore, the hygroscopicity of $KCaCl_3$ likely lies between the hygroscopicity of KCl (71°C) and $CaCl_2$ (110 °C) at a flue gas moisture of 25%, although probably

much closer to the hygroscopicity of KCl. As the average material temperature of the rings was somewhat below 80 °C (For Ring M: 77 °C (±) 2 °C and for Ring N 78 °C (±) 1.5 °C), it may have been possible for $KCaCl_3$ to deliquesce if present. Based on the melting diagram of Calcium and sodium chloride, a double salt of these components does not form.

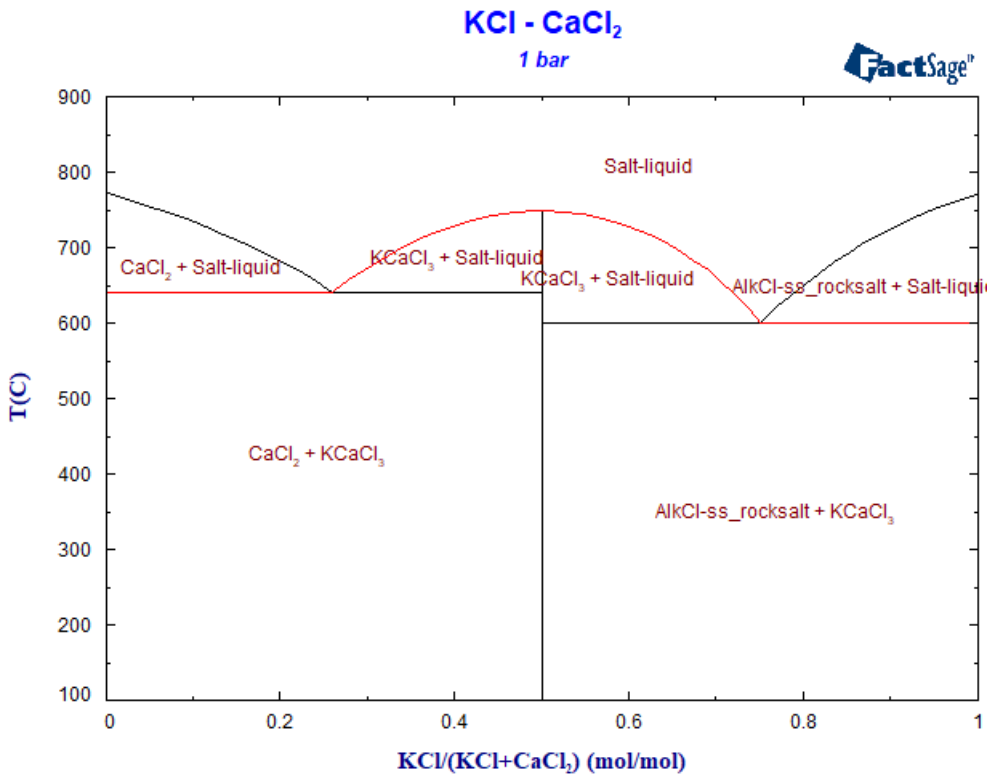

Figure 49: A melting diagram of the KCl-$CaCl_2$ system.

The detection of MgO in the XRD-sample also shows that the formation of $MgCl_2$ is a possibility. MgO behaves similarly to CaO and will form the corresponding $Mg(OH)_2$ at low flue gas temperatures, which can form $MgCl_2$ by reacting with HCl in the flue gas. The hygroscopic properties of $MgCl_2$ are much the same as with $CaCl_2$, with a DRH of 33 at 25 °C (DRH for $CaCl_2$ at 25 °C is 32) (Greenspan, 1977). However, based on its properties, $MgCl_2$ would also be expected to cause corrosion at 100 °C.

The formation of the double salts $NaMgCl_3$ and Na_2MgCl_3 from melting mixtures containing $MgCl_2$ and NaCl is also a possibility (Figure 50). Not much can be said about their hygroscopic properties due to the scarcity of material available. Nevertheless, as both $MgCl_2$ and NaCl are hygroscopic, the double salts should display similar behavior. This scenario can be considered less likely as the XRD-analysis detected magnesium mainly as MgO and $Ca_3MgSi_2O_8$.

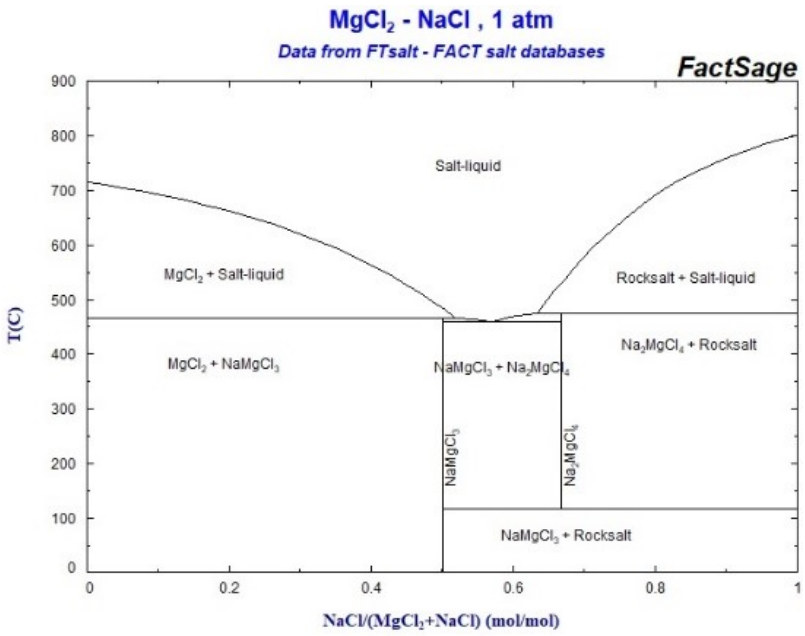

Figure 50: A melting diagram of the $MgCl_2$-NaCl system.

7. Conclusions

The impact of calcium on deposit chemistry and corrosion was studied in a full-scale bubbling fluidized bed boiler firing a fuel mixture of calcium-rich sludge and bark. Short-term deposit measurements were conducted in the superheater region and in the cold-end of the boiler. Short-term corrosion measurements were also conducted in the cold-end. As expected by the used fuel mixture, the content of the deposit was primarily dominated by calcium throughout the boiler.

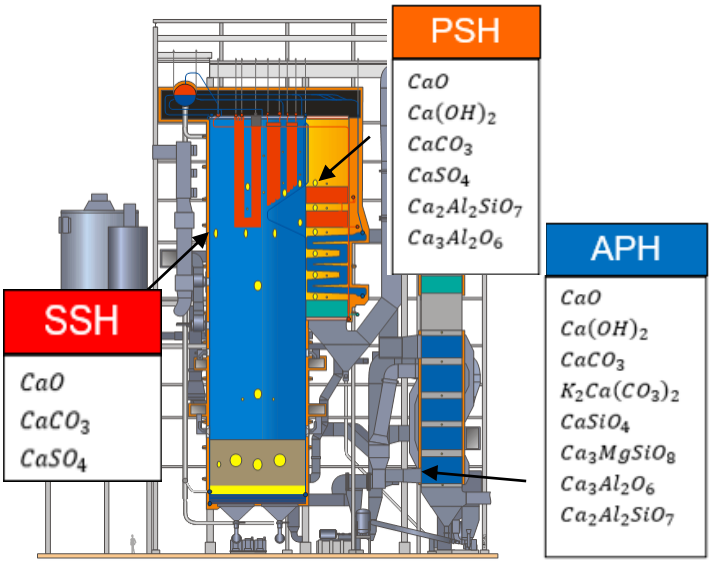

Figure 51: The detected phases of calcium at the measurement points. The phases at the SSH measurements are based only on the SEM analysis, as no XRD-analysis was conducted on these samples.

Although the rate of deposit build-up was low in the superheater region, the deposits were characterized to be quite aggressive. Relatively high chlorine contents were detected in the deposits as compared to the chlorine content in the fuel. Increased corrosion rates for X10CrMoVNb9-1 were observed with material temperatures between 500-550 °C in the secondary superheater region. Iron chlorides were also detected on nearly every sample in the superheater region. Deposit spot analyses showed that the corrosion was most likely alkali-induced. The high accumulation of alkali chlorides in combination with the decreased sulfation of alkali chlorides showed that when the Ca/S molar ratio is high, corrosion can occur even when firing fuels with low chlorine contents. There were also indications of $CaCl_2$ at the primary superheater. However, its role on high-temperature corrosion remains not fully understood.

In the cold-end deposit, the detections of chlorine were low but still significant compared to the chlorine content in the fuel. There were indications of $CaCl_2$ in the deposit, although the XRD-analysis could not confirm its presence. Based on the identification of iron chloride, a known corrosion product, it can be concluded that the observed corrosion at 80 °C was chlorine induced. The corrosion was likely caused by chlorine-based hygroscopic deposits, as HCl-induced dew point corrosion only occurs just above the water dew point. At higher temperatures, up to 120 °C, which was the highest temperature tested, corrosion was not observed. The lack of corrosion at 90°C and 100 °C was surprising as $CaCl_2$ has been shown to cause corrosion at this temperature. The contribution of $CaCl_2$ to the observed corrosion remains unclear as corrosion can be initiated by several other compounds at 80 °C. Therefore, such a low material temperature should be strictly avoided for heat-exchanger components in the cold-end. On the other hand, the lack of corrosion at 90°C, 100 °C and 120 °C shows that there is potential to lower the material temperature in the cold-end. This may be difficult to put into practice, as the content of the incoming fuel is challenging to monitor, and elevated levels of e.g. chlorine or zinc impurities may lead to corrosion at 100 °C and above. Nevertheless, there may be a possibility of lowering the present flue gas temperature. This could be further confirmed, for example, by gathering references from longer-term corrosion measurements, and by further studies of the hygroscopicity of the deposits.

8. References

Aho, M., Vainikka, P., Taipale, R., & Yrjas, P. Effective new chemicals to prevent corrosion due to chlorine in power plant superheaters. *Fuel,* Volume 87(6) (**2008**), Pages 647-654.

Aho, M., Yrjas, P., Taipale, R., Hupa, M., & Silvennoinen, J. Reduction of superheater corrosion by co-firing risky biomass with sewage sludge. *Fuel, 89*(9) (**2010**), Pages 2376-2386.

Amand, L., & Leckner, B. Reduction of emissions of sulphur and chlorine from combustion of high volatile waste fuels (sludge) in fluidised bed. Paper presented at the Proceedings of the 3rd International Conference on Combustion, Incineration/Pyrolysis and Emission Control (3rd i-CIPEC), **2004**, Hangzhou, China, Pages 476-481.

Anthony, E. J., & Granatstein, D. L. Sulfation phenomena in fluidized bed combustion systems. *Progress in Energy and Combustion Science***,** Volume 27(2) (**2001**), Pages 215-236.

Barroso, J., Ballester, J., & Pina, A. Study of coal ash deposition in an entrained flow reactor: Assessment of traditional and alternative slagging indices. *Fuel Processing Technology*, Volume 88(9) (**2007**), Pages 865-876.

Baxter, L. L. A Task 2. Pollutant emission and deposit formation during combustion of biomass fuels. Lawrence Livermore Laboratory, Berkeley (CA, USA). **1994**.

Baxter, L. L. Ash deposition during biomass and coal combustion: A mechanistic approach. *Biomass and Bioenergy*, Volume 4(2) (**1993**), Pages 85-102.

Beck, J., & Unterberger, S. The behaviour of phosphorus in the flue gas during the combustion of high-phosphate fuels. *Fuel,* Volume 85(10-11) (**2006**), Pages 1541-1549.

Bergman, A. G., & Sementsova, A. K. The ternary systems K_2Cl_2-Na_2SO_4-Na_2CO_3 and Na_2Cl_2-K_2SO_4-K_2CO_3. *Zhur.Neorg.Khim*, Volume 3(2) (**1958**), Pages 393-402.

Bhaskaran, R., Palaniswamy, N., Rengaswamy, N. S., & Jayachandran, M. Global cost of corrosion—A historical review. *Corrosion: Materials*, Volume 13(**2005**), Pages 621-628.

Brinch-Pedersen, H., Sørensen, L. D., & Holm, P. B. Engineering crop plants: Getting a handle on phosphate. *Trends in Plant Science*, Volume 7(3) (**2002**), Pages 118-125.

Broström, M., Enestam, S., Backman, R., & Mäkelä, K. Condensation in the KCl–NaCl system. *Fuel Processing Technology,* Volume 105 (**2013**), Pages 142-148.

Bryers, R. W. Fireside slagging, fouling, and high-temperature corrosion of heat-transfer surface due to impurities in steam-raising fuels. *Progress in Energy and Combustion Science*, Volume 22(1) (**1996**), Pages 29-120.

Choi, S. H., & Stringer, J. (1985). Calcium sulfate-induced corrosion of iron-chromium alloys. *Corrosion Scienc*e, Volume, 28(**1998**), Pages 839-850.

Elled, A., Davidsson, K. O., & Amand, L. Sewage sludge as a deposit inhibitor when co-fired with high potassium fuels. *Biomass and Bioenergy,* Volume 34(11) (**2010**), Pages 1546-1554.

Flagan, R. C., & Sarofim, A. F. Comments on the paper by WT Reid. *Progress in Energy and Combustion Science*, Volume 10(**1984**), Pages 171-175.

Folkeson, N. Chlorine induced corrosion in biomass and waste fired boilers: Laboratory and field investigations, PhD thesis, Chalmers University of Technology, Gothenburg. **2010**. ISBN 978-91-7385-406-1

Franceschi, V. R., & Nakata, P. A. Calcium oxalate in plants: Formation and function. *Annu.Rev.Plant Biol.*, Volume 56(**2005**), Pages 41-71.

Frandsen, F. J. Ash Formation, Deposition and Corrosion when Utilizing Straw for Heat and Power Production. Technical University of Denmark, Lyngby, Denmark. **2011**. ISBN: 978-87-92481-40-5.

Grabke, H. J., Reese, E., & Spiegel, M. The effects of chlorides, hydrogen chloride, and sulfur dioxide in the oxidation of steels below deposits. *Corrosion Scienc*e, Volume, 37(7) (**1995**), Pages 1023-1043.

Greenspan, L. Humidity fixed points of binary saturated aqueous solutions. *Journal of Research of the National Bureau of Standards*, Volume 81(1) (**1977**), Pages 89-96.

Hamm, U. Environmental aspects. *Handbook of Paper and Board,* **2006**, Pages 422-445.

Hansen, L. A., Nielsen, H. P., Frandsen, F. J., Dam-Johansen, K., Hørlyck, S., & Karlsson, A. Influence of deposit formation on corrosion at a straw-fired boiler. *Fuel Processing Technology*, Volume 64(1-3) (**2000**), Pages 189-209.

Haynes, B. S., Neville, M., Quann, R. J., & Sarofim, A. F. Factors governing the surface enrichment of fly ash in volatile trace species. *Journal of Colloid and Interface Science*, Volume 87(1) (**1982**), Pages 266-278.

Heinzel, T., Maier, J., Baum, J., Spliethoff, H., & Hein, K. Slagging and fouling in dry and molten ash PFC. *Joule III Programme Clean Coal Technology R&D*, Volume 5(**1998**), Pages 1-63.

Higo, T., Sukenaga, S., Kanehashi, K., Shibata, H., Osugi, T., Saito, N., & Nakashima, K. Effect of potassium oxide addition on viscosity of calcium aluminosilicate melts at 1673–1873 K. *ISIJ International*, Volume 54(9) (**2014**), Pages 2039-2044.

Jenkins, B., Baxter, L. L., Miles Jr, T. R., & Miles, T. R. Combustion properties of biomass. *Fuel Processing Technology,* Volume 54(1-3) (**1998**), Pages 17-46.

Karlsson, S., Pettersson, J., Johansson, L., & Svensson, J. Alkali-induced high temperature corrosion of stainless steel: The influence of NaCl, KCl and $CaCl_2$. *Oxidation of Metals*, Volume 78(1-2) (**2012**), Pages 83-102.

Kosnyrev, G. T., Desyatnik, V. N., & Nosonova, E. N. Study of transformations in the $Ca(OH)_2$–$CaCl_2{\cdot}2H_2O$ system during thermal dehydration (in russian). *Zh Prikl Khim*, Volume 63(1) (**1990**), Pages 187-190.

Kosnyrev, G. T., Desyatnik, V. N., & Nosonova, E. N. Hydrolysis of calcium chloride during thermal dehydration of its tetrahydrate (in russian). Deposited doc., SPSTL 1005 Khp-D81.**1981**.

Lee, Y. Y., & McNallan, M. J. Ignition of nickel in environments containing oxygen and chlorine. *Metallurgical Transactions A*, Volume 18(6) (**1991**), Pages 1099-1107.

Lehmusto, J., Yrjas, P., Skrifvars, B., & Hupa, M. High temperature corrosion of superheater steels by KCl and K_2CO_3 under dry and wet conditions. *Fuel Processing Technology*, Volume 104(**2012**), Pages 253-264.

Li, X., Gupta, D., Eom, H., Kim, H., & Ro, C. Deliquescence and efflorescence behavior of individual NaCl and KCl mixture aerosol particles. *Atmospheric Environment*, Volume 82(**2014**), Pages 36-43.

Lin, W. Interactions between SO_2 and NO_x emissions in fluidised bed combustion of coal, PhD Thesis, Delft University, The Netherlands, **1994**.

Lindau, L., & Goldschmidt, B. Low temperature corrosion in bark fueled small boilers. Värmeforsk Services AB, Rapport M9-835, **2008**.

Lindstrom, E., Sandström, M., Bostrom, D., & Ohman, M. Slagging characteristics during combustion of cereal grains rich in phosphorus. *Energy & Fuels*, Volume 21(2) (**2007**), Pages 710-717.

Liu, H. Biomass fuels for small and micro combined heat and power (CHP) systems: Resources, conversion and applications. *Small and Micro Combined Heat and Power (CHP) Systems*, **2011**, Pages 88-122. Woodhead Publishing.

https://doi.org/10.1533/9780857092755.1.88

Lloyd, G. E. Atomic number and crystallographic contrast images with the SEM: A review of backscattered electron techniques. *Mineralogical Magazine*, Volume 51(359) (**1987**), Pages 3-19.

Manzel, J. Sevar-trocknungsverfahren mit dünnbett. *Beiheft Zu Müll Und Abfall*, Volume 28 (**1989**), Pages 74-81.

Marschner, H. Mineral Nutrition of Higher Plants, 2nd Edition; Academic Press: London, **1995**, Pages 265−277. (ISBN 0-12-473543-6).

Matsuoka, K., Yamashita, T., Kuramoto, K., Suzuki, Y., Takaya, A., & Tomita, A. Transformation of alkali and alkaline earth metals in low rank coal during gasification. *Fuel*, Volume 87(6) (**2008**), Pages 885-893.

McGhee, T. J., & Steel, E. W. Water supply and sewerage, McGraw-Hill, New York, **1991**, Volume 6.

Ministry of Agriculture and Forestry. The forest resources of Finland. **2019**. Retrieved from

https://mmm.fi/sv/skogar/skogsbruk/finlands-skogstillgangar

Moss, G. The fluidized desulphation gasifier. Paper presented at the Proceedings of the Second International Conference on Fluidized Bed, **1970**, Pages II6-1-7.

Moss, G. (1975). The mechanisms of sulphur absorption in fluidized beds of lime. Paper presented at the Institute of Fuel Symposium Series (London), Volume 1 (**1975**), Pages D2-7.

Murray, H. Industrial clays case study. *Mining, Minerals and Sustainable Development,* IIED and WBCSD, Volume 64 (**2002**), Pages 1-9.

Oka, S. Fluidized bed combustion. Boca Raton, CRC press, **2003**.

https://doi.org/10.1201/9780367801267

Onasch, T. B., McGraw, R., & Imre, D. Temperature-dependent heterogeneous efflorescence of mixed ammonium sulfate/calcium carbonate particles. *The Journal of Physical Chemistry A*, Volume 104(46) (**2000**), Pages 10797-10806.

Partanen, J. Chemistry of HCI and limestone in fluidised bed combustion. PhD thesis, Åbo Akademi Turku, Finland. **2004**. Report number AAA-KTF/PCC-04-1, ISBN 952-12-1287-X.

Partington JR. A text-book of inorganic chemistry. 5th ed. London: Macmillan, 1939.

Pettersson, A., Zevenhoven, M., Steenari, B., & Amand, L. Application of chemical fractionation methods for characterisation of biofuels, waste derived fuels and CFB co-combustion fly ashes. *Fuel*, Volume 87(15-16) (**2008**), Pages 3183-3193.

https://doi.org/10.1016/j.fuel.2008.05.030

Pettersson, J., Asteman, H., Svensson, J., & Johansson, L. KCl induced corrosion of a 304-type austenitic stainless steel at 600 C; the role of potassium. *Oxidation of Metals,* Volume 64(1-2) (**2005**), Pages 23-41.

Pontoppidan, K., Pettersson, D., & Sandberg, A. The type of thermal feed treatment influences the inositol phosphate composition. *Animal Feed Science and Technology*, Volume 132(1-2) (**2007**), Pages 137-147.

Priyanto, D. E., Ueno, S., Sato, N., Kasai, H., Tanoue, T., & Fukushima, H. Ash transformation by co-firing of coal with high ratios of woody biomass and effect on slagging propensity. *Fuel*, Volume 174 (**2016**), Pages 172-179.

Reid, W. T. The relation of mineral composition to slagging, fouling and erosion during and after combustion. *Progress in Energy and Combustion Science*, Volume 10(2) (**1984**), Pages 159-169.

Retschitzegger, S., Brunner, T., & Obernberger, I. Low-temperature corrosion in biomass boilers fired with chemically untreated wood chips and bark. *Energy & Fuels*, Volume 29(6) (**2015**), Pages 3913-3921.

Scala, F., & Chirone, R.Characterization and early detection of bed agglomeration during the fluidized bed combustion of olive husk. *Energy & Fuels*, Volume 20(1) (**2006**), Pages 120-132.

Scala, F., & Chirone, R. A SEM/EDX study of bed agglomerates formed during fluidized bed combustion of three biomass fuels. *Biomass and Bioenergy*, Volume 32(3) (**2008**), Pages 252-266.

Schouten, J. C., & Van den Bleek, C M. Sulfur retention and NOx reduction: The sure model. *Coal science and technology, Volume 22 (**1995**), Pages 227-257, Elsevier.*

Schouten, J. C. Sulfur retention and particle motion during fluidized bed combustion of coal. PhD Thesis, Technical University of Delft, Delft University Press, The Netherlands, **1988**.

Schwuger, M. J. Detergents and the environment, Jülich GmbH, Jülich, Germany: Institute of Applied Physical Chemistry Research Center. **1996**. ISBN 0-8247-9396-X.

Scott, G. M., & Smith, A. Sludge characteristics and disposal alternatives for the pulp and paper industry. Paper presented at the Tappi International Environmental Conference. **1995**. Page 269.

Senelwa, K., & Sims, R. E. Fuel characteristics of short rotation forest biomass. *Biomass and Bioenergy*, Volume 17(2) (**1999**), Pages 127-140.

Skrifvars, B. J., Blomquist, J. P., Hupa, M., & Backman, R. Predicting the ash behavior during biomass combustion in FBC conditions by combining advanced fuel analyses with thermodynamic multicomponent equilibrium calculations. Paper presented at the Pittsburgh Coal Conference, Pittsburgh, PA (United States). **1998**.

Skrifvars, B., Yrjas, P., Laurén, T., Hupa, M., & Dittrich, M. The Åbo Akademi database: Ash behavior measurements in full-scale boilers. Paper presented at the 18th International Conference on Fluidized Bed Combustion, **2005**, Pages 573-579.

Statistics FInland. Waste statistics. **2014**. Retrieved from: http://www.stat.fi/til/jate/2012/jate_2012_2014-05-15_tie_001_en.html

Stromberg, B., & Herstad Svärd, S. Bränslehandboken 2012 (The Fuel Handbook 2012). Värmeforsk (Thermal Engineering Research Institute), Stockholm, Sweden.

Tang, I. N., & Munkelwitz, H. R. Composition and temperature dependence of the deliquescence properties of hygroscopic aerosols. *Atmospheric Environment. Part A. General Topics*, Volume 27(4) (**1993**), Pages 467-473.

Tchobanoglous, G.; Burton, F. L & Stensel, H. D. Wastewater Engineering: Treatment, Disposal and Reuse, 4th ed.; Metcalf & Eddy, McGraw-Hill: New York, **1991**. ISBN: 9780070495395.

Usherson, J. Recycled paper and sludge. *Resource Recycling*, Volume 11(3) (**1992**), Pages 95-100.

Vainio, E., DeMartini, N., Hupa, L., Amand, L., Richards, T., & Hupa, M. Hygroscopic properties of calcium chloride and its role on cold-end corrosion in biomass combustion. *Energy & Fuels*, Volume 33(11) (**2019**), Pages 11913-11922

Vainio, E., Kinnunen, H., Laurén, T., Brink, A., Yrjas, P., DeMartini, N. Low-temperature corrosion in co-combustion of biomass and solid recovered fuels. *Fuel*, Volume 184 (**2016**), Pages 957-965.

Van der Loo, S., & Koppejan, H. Handbook of biomass: Combustion and cofiring. Twente University Press. **2002**. ISBN 9036517737.

Vassilev, S. V., Baxter, D., Andersen, L. K., & Vassileva, C. G. An overview of the composition and application of biomass ash. Part 1. Phase–mineral and chemical composition and classification. *Fuel*, Volume 105 (**2013**), Pages 40-76.

Weast, R. C., Ed. Handbook of Chemistry and Physics, CRC: Boca Raton, FL, **1975**.

Weinell, C. E., Jensen, P. I., Dam-Johansen, K., & Livbjerg, H. Hydrogen chloride reaction with lime and limestone: Kinetics and sorption capacity. *Industrial & Engineering Chemistry Research*, Volume 31(1) (**1992**), Pages 164-171.

Werkelin, J., Skrifvars, B., Zevenhoven, M., Holmbom, B., & Hupa, M. Chemical forms of ash-forming elements in woody biomass fuels. *Fuel*, Volume 89(2) (**2010**), Pages 481-493.

Wexler, A. S., & Seinfeld, J. H. Second-generation inorganic aerosol model. *Atmospheric Environment. Part A.General Topics*, Volume 25(12) (**1991**), Pages 2731-2748.

Wzorek, M). Characterisation of the properties of alternative fuels containing sewage sludge. *Fuel Processing Technology*, Volume 104 (**2012**), Pages 80-89.

Yrjas, P., Aho, M., Zevenhoven, M., Taipale, R., Silvennoinen, J., & Hupa, M. Co-firing of sewage sludge with bark in a bench-scale bubbling fluidized bed—a study of deposits and emissions. Paper presented at the Proceedings of the 20th International Conference on Fluidized Bed Combustion*,* **2009**, Pages 922-929.

Zevenhoven, M., Yrjas, P., Skrifvars, B., & Hupa, M). Characterization of ash-forming matter in various solid fuels by selective leaching and its implications for fluidized-bed combustion. *Energy & Fuels*, Volume 26(10) (**2012**), Pages 6366-6386.

Zevenhoven-Onderwater, M. Ash-forming matter in biomass fuels. PhD thesis, Åbo Akademi, Åbo/Turku, Finland. **2001**.

Zhang, B., Zhong, Z., Xue, Z., Xue, J., & Xu, Y. Release and transformation of potassium in co-combustion of coal and wheat straw in a BFB reactor. *Applied Thermal Engineering*, Volume 144 (**2018**), Pages 1010-1016.